Doctor of Philosophy

Hydrogen Control of Dielectric Oxides for Multi-functional Sensors

Department of Physics and Energy Harvest-Storage Research Center (EHSRC),

University of Ulsan, Ulsan 44610, Republic of Korea

Nguyen Xuan Duong

Hydrogen Control of Dielectric Oxides for Multi-functional Sensors

Supervisor: Tae Heon Kim

A Dissertation submitted to the Graduate School of the University of Ulsan in partial Fulfillment of the requirements for the Degree of

Doctor of Philosophy

June 2023

by

Nguyen Xuan Duong

Department of Physics and Energy Harvest-Storage Research Center (EHSRC),

University of Ulsan, Ulsan 44610, Republic of Korea

Hydrogen Control of Dielectric Oxides for Multi-functional Sensors

This is to declare that the dissertation

submitted by Nguyen Xuan Duong is approved officially.

신 영 한

Committee Chair: Prof. Young-Han Shin

Department of Physics, University of Ulsan

조 성 래

Committee Member: Prof. Sunglae Cho

Department of Physics, University of Ulsan

Teun-Teun Kim

Committee Member: Prof. Teun-Teun Kim

Department of Physics, University of Ulsan

손 창 희

Committee Member: Prof. Changhee Sohn

Department of Physics, Ulsan National Institute of Science and Technology

Tae Heon Kim

Committee Member and Supervisor: Prof. Tae Heon Kim

Department of Physics, University of Ulsan

Department of Physics and Energy Harvest-Storage Research Center (EHSRC),

University of Ulsan, Ulsan 44610, Republic of Korea

June 2023

Abstract

Dielectrics are insulating materials characterized by the ability to become polarized (i.e., dielectric permittivity) in the presence of an electric field. Nowadays, improving dielectric permittivity in complex oxides is of great interest in the aspects of fundamental science as well as technological applications. Note that such a huge dielectric permittivity, which is controllable by external stimuli, enables us to accomplish multi-functional nano-devices such as switchable passive sensors potentially. In this thesis, we demonstrate the hydrogenation control of dielectric responses in complex oxide ceramics for practical applications in dielectric-based gas sensors. First, an unusual polymorphic phase, which is an excellent platform to examine the protonation effect, is realized in oxide ceramics by cation substitution. Second, we systematically investigate the hydrogenation effect on the dielectric properties of dielectric oxide ceramics. Finally, by reversibly manipulating dielectric permittivity through protonation, we also provide a conceptual demonstration of the realization of dielectric-based humidity sensors with high performance.

First, we present a room-temperature polymorphic phase transition in $BaTiO_3$ ceramics induced by Ni substitution. As the Ni concentration increases, the initial tetragonal structure changes to a hexagonal structure. A possible mechanism of polymorphic transition in Ni-substituted $BaTiO_3$ ceramics is discussed in conjunction with the microscopic analyses of the crystal structure and the electronic configuration. The oxygen vacancy defects are generated in oxide ceramics due to the substitution of Ni^{2+} to the Ti^{4+} cations. With the formation of oxygen vacancies, the Ti oxidation state is locally reduced from 4+ to 3+. Due to the reduction of the local Ti charge valency, the polar Ti-O hybridization in tetragonal $BaTiO_3$ becomes weakened, leading to the structural phase transition in Ni-substituted $BaTiO_3$ ceramics. As a result, a high-temperature 6H-hexagonal phase is realized in $BaTiO_3$ ceramics by Ni substitution.

Second, we demonstrate an ultrahigh dielectric permittivity in the 6H-hexagonal $BaTiO_3$ ceramics by hydrogenation via the specific treatment under ambient environments. We observed a significant enhancement of low-frequency dielectric permittivity at room temperature when the as-sintered oxygen-deficient $BaTiO_3$ ceramics were exposed to water-vapor-containing ambient environments. Intriguingly, the huge dielectric permittivity (i.e., on-state) in the treated ceramics is recovered to the initial value (i.e., off-state) of as-sintered ceramics by external stress, indicating the reversible manipulation of dielectric responses. When the as-sintered $BaTiO_3$ ceramics are exposed to the ambient air containing water vapor, the dissociated protons (H^+) from water molecules are introduced into the ceramics due to the high mobility. The introduction of hydrogen ions produces the heterogeneous distributions of the crystal structures and the electric polarizability microscopically leading to the enhancement of overall dielectric permittivity in the Ni-substituted $BaTiO_3$ ceramics.

For device applications, we examine the sensing capability of our Ni-substituted $BaTiO_3$ ceramics for the realization of dielectric humidity sensors. The dielectric and associated electrical properties of Ni-substituted $BaTiO_3$ are highly sensitive to ambient environments. The modification of dielectric responses under various ambient conditions (i.e., ambient air, vacuum, N_2, CO_2, water vapor, liquid water, and acetic acid) is systematically examined. Dielectric relaxation characteristics of Ni-substituted $BaTiO_3$ ceramics are reversibly controllable by hydrogenation through the treatment under ambient environments and thermal annealing. We also evaluate the humidity sensing properties of Ni-substituted $BaTiO_3$ in an actual sensor. The susceptibility of dielectric permittivity and related electrical conductivity to a humid atmosphere enables the realization of oxide-ceramic-based humidity sensors with high efficiency and sensitivity.

Table of contents

List of Figures

Chapter 1

Introduction

1.1. Dielectrics

1.1.1. Polarization in dielectrics

In electromagnetism, a dielectric is an electrical insulator that can be polarized by an applied electric field [1]. There are many materials called dielectric materials in nature such as wood, glass, chalk, plastics, papers, or even distilled water. The unique property of an ideal dielectric is that it does not contain free charges which can move from molecule to molecule. The bound charges are tightly bound to the atomic or molecular structure, however, the bound charges can shift a small distance from their binding centers.

An important concept in dielectric theory is that of an electrical dipole moment, which is simply a separation between a negative and positive charge of equal magnitude Q, as shown in Figure 1.1. If a is the vector from the negative to the positive charge, the electric dipole moment is defined as a vector by [2].

$$\boldsymbol{p} = Qa \tag{1.1}$$

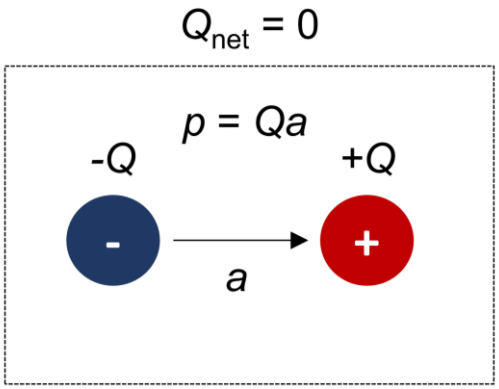

Figure 1.1 The definition of electrical dipole moment.

When a dielectric is placed in an electric field, positive and negative charges tend to move in the opposite direction in response to the applied field, creating a separation between two opposite charged centers [2, 3]. This separation between positive and negative charges generates the dipole moments ***p*** within the dielectric media under the applied electric field (Figure 1.2). The electrical polarization ***P*** is defined as the accumulation of all dipole moments in a unit volume Δv in dielectrics.

$$\boldsymbol{P} = \lim_{\Delta v \to 0} \frac{1}{\Delta v} \sum_i \boldsymbol{p_i} \tag{1.2}$$

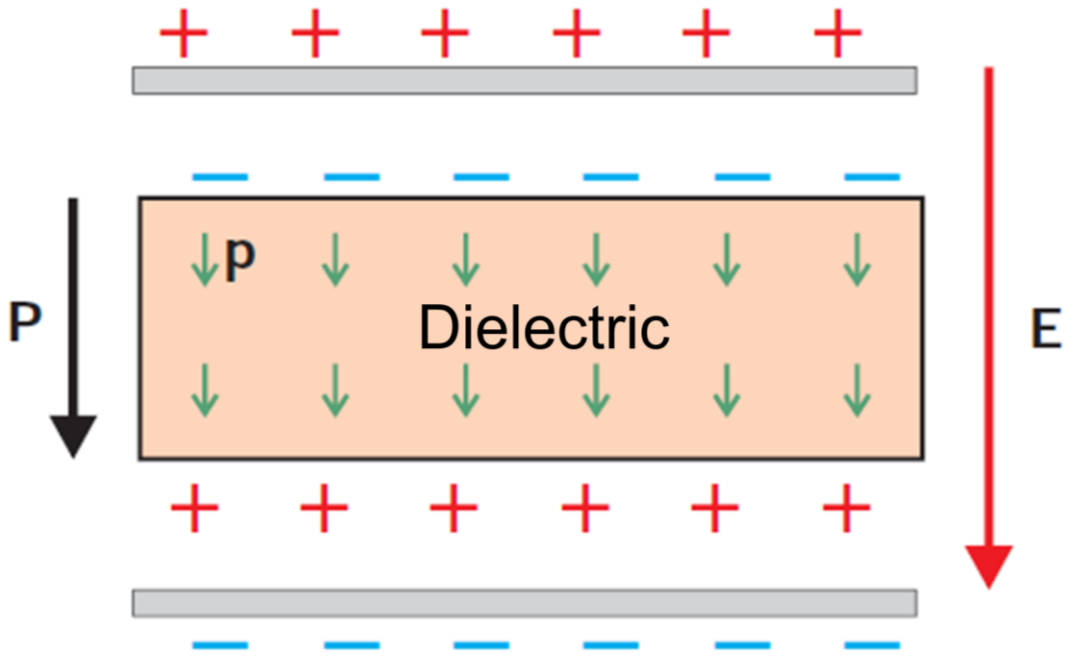

Figure 1.2 Schematic of dielectric materials under the applied electric field. The dielectrics are polarized resulting in the formation of electrical polarization (***P***) [1].

1.1.2. Electrical polarizability and relative permittivity in electromagnetism

The magnitude of the induced dipole moment is determined by the electric field that triggers it. To establish a connection between the induced dipole moment $\boldsymbol{p}$ and the electric field $\boldsymbol{E}$ that leads to it, we utilize a parameter called polarizability α [2, 3].

$$\boldsymbol{p} = \alpha \boldsymbol{E} \tag{1.3}$$

Here, in the simple case, we assume the polarizability (α) from the electronic polarization only. So, polarization ($\boldsymbol{P}$) can be expressed in terms of polarizability:

$$\boldsymbol{P} = N\alpha \boldsymbol{E} \tag{1.4}$$

where N is the number of dipole moments per unit volume. On the other hand, in a dielectric material, the induced polarization is proportional to the external electric field $\boldsymbol{E}$ and can be expressed as:

$$\boldsymbol{P} = \varepsilon_0 \chi \boldsymbol{E} \tag{1.5}$$

with ε_0 as the permittivity of vacuum and χ is the dielectric susceptibility. The dielectric susceptibility (χ) and the polarizability (α) are related by.

$$\chi = \frac{1}{\varepsilon_0} N\alpha \tag{1.6}$$

Dielectric displacement $\boldsymbol{D}$ can be described by:

$$\boldsymbol{D} = \varepsilon_0 \boldsymbol{E} + \boldsymbol{P} = \varepsilon_0 (1 + \chi) \boldsymbol{E} = \varepsilon_0 \varepsilon_r \boldsymbol{E} \tag{1.7}$$

where $\varepsilon_r = (1 + \chi)$ is the relative dielectric permittivity (dielectric constant), corresponding to the degree of polarization in the dielectric materials.

The relative permittivity is in terms of polarizability.

$$\varepsilon_r = 1 + \frac{1}{\varepsilon_0} N\alpha \tag{1.8}$$

Equation 1.8 indicates the relationship between the relative permittivity and polarizability. The dielectric permittivity defines how strongly a dielectric material becomes electrically polarized under the influence of an electric field.

There are different polarization mechanisms of an insulating solid including electronic, ionic, orientational, and space charge polarizations. In the absence of an electric field, the electronic charge cloud surrounding an atom (at a little distance from the atom) is symmetrically disposed around the nucleus. In an electric field this charge cloud becomes deformed and the center of the electronic negative charge is no longer coincident with the positive nuclear charge (Figure 1.3), and a dipole will arise. This effect is termed electronic polarizability. Charged ions in a solid will suffer a displacement in an electric field resulting in ionic polarizability, ai (Figure 1.3). A number of common molecules, including water, carry a permanent dipole. If such molecules are exposed to an electric field, they will try to orient the dipole along the field (Figure 1.3) leading to orientational polarizability. As the movement of molecules in solids is restricted, orientational polarizability is more often noticed in gases and liquids. If a material has mobile charges present, electrons, holes or ions, they will move under the influence of the electric field, with positive charges moving towards one electrode and negative charges towards the other. These will tend to build up at grain boundaries and the electrode regions until the resulting charge inhibits further movement and equilibrium is reached, producing space charge polarizability. Good ionic conductors often show pronounced space charge effects.

At low enough frequencies the value of the relative permittivity measured will be identical to the static value, and all polarizability terms will contribute to dielectric permittivity. However, space charge polarization is usually unable to follow changes in electric field that occur much faster than that of radio frequencies, about 10 Hz, and this contribution will no longer be registered at frequencies much higher than this value. Similarly, any dipoles present are usually unable to rotate to the alternations of the electric field when frequencies reach the microwave region, about 10^6 Hz, and at higher frequencies this contribution will be lost. Ionic polarizability, involving the movement of atomic nuclei, is no longer registered when the frequency of the field approaches that of the infrared range, 10^{12} Hz. Electrons, being the lightest components of matter, still respond to an alternating electric field at frequencies corresponding to the visible region, 10^{14} Hz, but even the contribution of electronic polarizability drops out at ultraviolet frequencies (Figure 1.3).

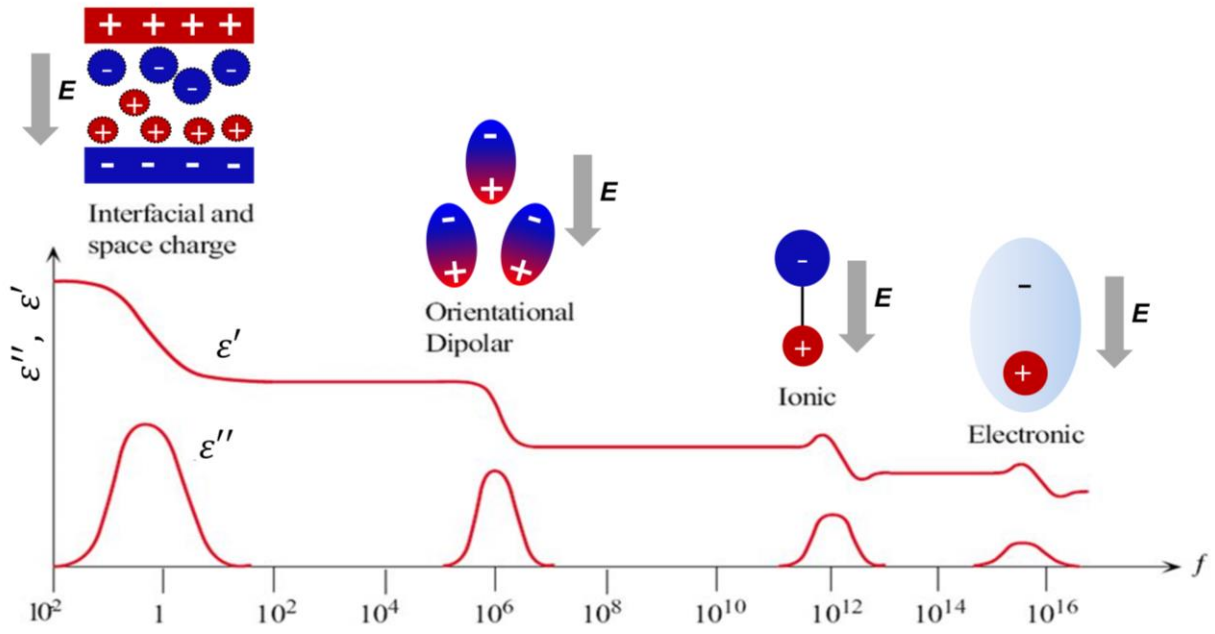

Figure 1.3 Real and imaginary parts of complex dielectric permittivity as a function of frequency.

1.1.3. Colossal dielectric constant

The dielectric constant, also known as the relative permittivity, is a physical property of a dielectric material that describes its ability to store electric charge in an electric field. In previous reports, the colossal dielectric constant (CDC) usually refers to a phenomenon observed in certain dielectric materials where the dielectric constant can be greatly enhanced by several orders of magnitude, up to values of 1000 or more, under certain conditions such as temperature, pressure, or doping with impurities (Figure 1.4) [4]. Up to now, studies on colossal dielectric permittivity in dielectrics have garnered significant attention, particularly in relation to their fundamental scientific implications and potential technological applications.

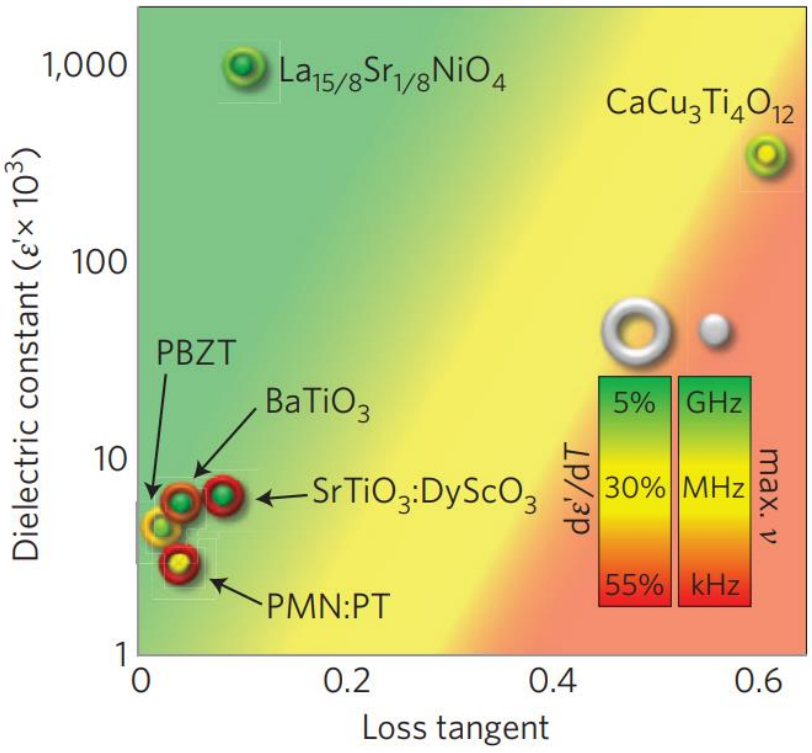

Figure 1.4 Comparison of several dielectric compounds exhibiting the colossal dielectric permittivity in the previous studies [4].

Nowadays, dielectric materials with ultrahigh dielectric permittivity are in demand for various technological applications, as shown in Figure 1.5 [4-7]. For example, in the field of electronics, dielectrics are commonly used in capacitors, which are fundamental components in electronic circuits. Furthermore, dielectric materials are essential in energy storage devices, such as batteries capacitor banks, and supercapacitors. Dielectric materials used in these devices can improve their performance by enhancing energy storage capacity, increasing charge and discharge rates, and improving overall efficiency. For sensing applications, dielectrics can be utilized in a wide range of sensing devices (e.g., capacitive sensors, humidity sensors, strain sensors, and so on) [7, 8]. The change in electrical properties (e.g., capacitance, resistance, impedance) are measured to detect various environmental conditions.

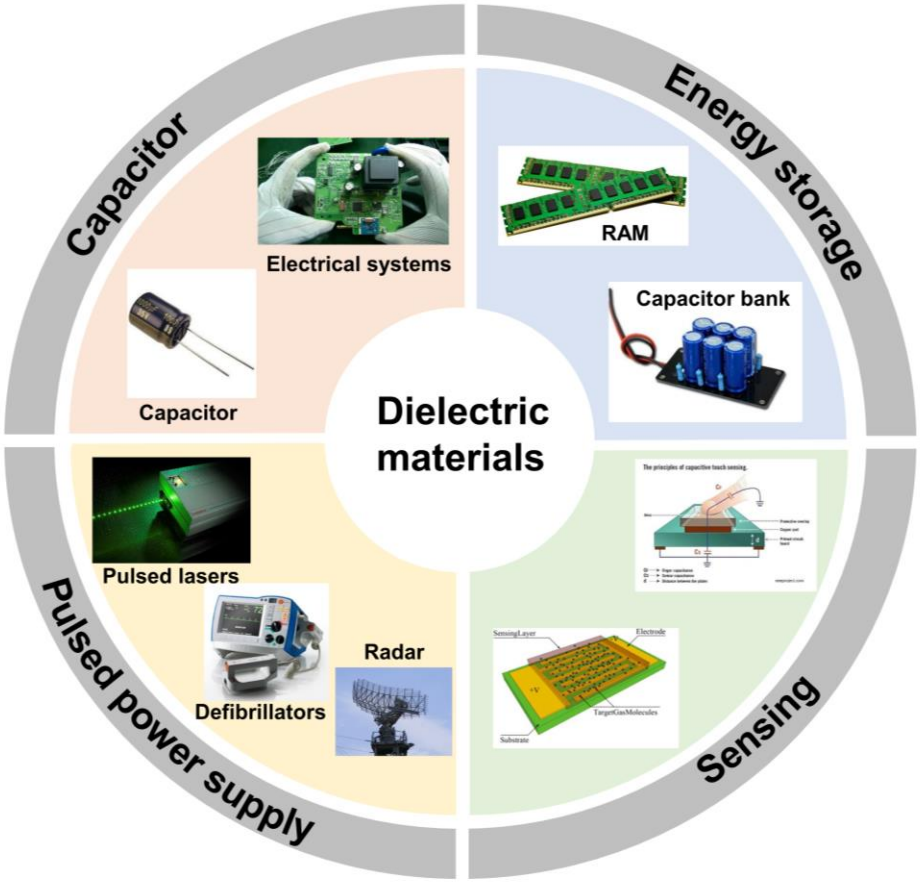

Figure 1.5 Schematic illustration of the applications of dielectric materials in various fields.

1.1.4. Control of dielectric permittivity in dielectric materials by external stimuli

In dielectric materials, the control of dielectric properties by external stimuli is of significant importance for realizing the unusual functional phenomena due to the fundamental scientific development and promising device applications [9-12]. The attractive functionalities of controllable dielectric properties to external stimuli include photo-dielectric [13, 14], magneto-dielectric [15-17], and mechanical stress-induced dielectric constant effects [18, 19], as shown in Figure 1.6. For example, tuning of a dielectric constant by photo-irradiation is called the photo-dielectric effect. Intriguingly, the magneto-dielectric effect has attracted significant attention

because of the ability to manipulate dielectric permittivity under external magnetic fields. The fascinating physical phenomena of manipulation of dielectric permittivity to external stimuli can enable the realization of multifunctional devices.

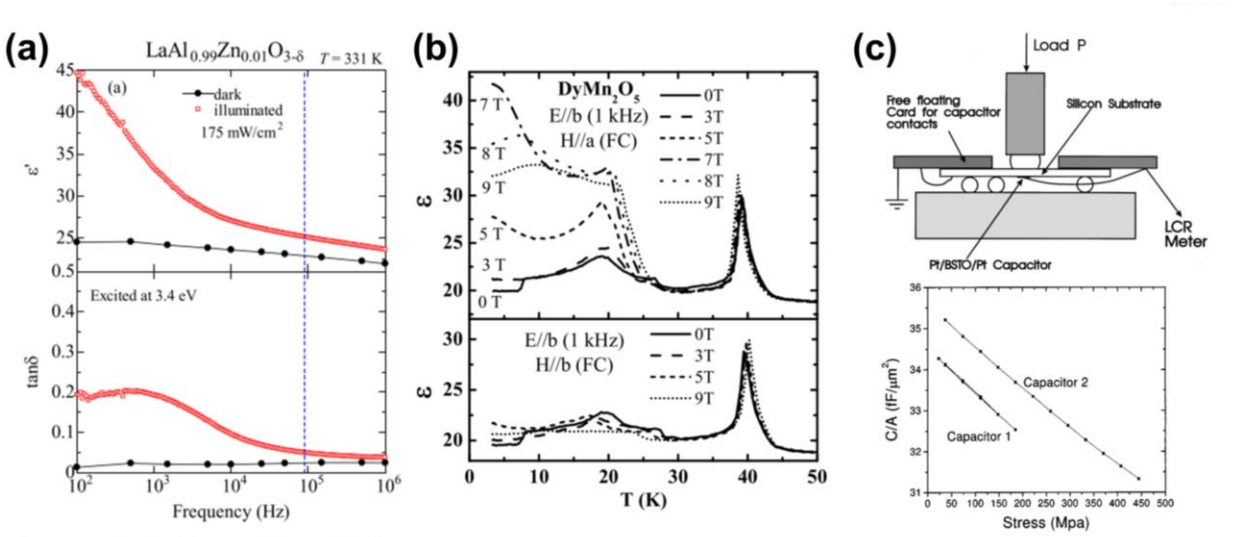

Figure 1.6 Control of dielectric responses in complex oxides by external stimuli. (a) The photo-dielectric effect. (b) The magneto-dielectric coupling. (c) The mechanical stress-induced dielectric constant effect [14, 17, 18].

1.2. Reversible manipulation of dielectric responses for sensing applications

In an aspect of technological applications, the control of dielectric permittivity by external stimuli in dielectric materials can be utilized for the implementation of sensing devices. For instance, photo-dielectric materials have been used in photodetector applications to enable the detection of light by monitoring their photo-induced changes in dielectric permittivity [20]. Magneto-dielectric materials, which exhibit changes in their dielectric permittivity in response to an applied magnetic field, can be harnessed in magnetic field sensors to detect the presence, strength, and direction of a magnetic field [17, 21]. In the capacitive gas sensors, the variation of dielectric constant under a gas environment with respect to a reference condition is an output signal

to detect the presence of a gas [8, 22]. By boosting dielectric permittivity of dielectric materials under the gas environment, the ratio of dielectric constants between the initial state (under a reference condition) and the treated state (under the gas environment) is further enhanced, allowing us to realize capacitive gas sensors with high sensitivity.

1.3. Motivation: Protonation control of physical properties in complex oxides

Protonation, the introduction of protons (H^+) to materials, has been demonstrated as a versatile approach to control and manipulate the physical properties of complex oxide materials. Note that the hydrogen ion is the lightest ionic mass and the smallest ionic radius [23]. The incorporated protons into oxide materials can induce changes in the local lattice structure and bonding characteristics, leading to modifications in their physical properties. In previous studies, a variety of physical properties of functional oxides (e.g., crystal and electronic structures, the electrical, magnetic, and transport characteristics) are reversibly controllable by hydrogenation/dehydrogenation processes (Figure 1.7) [24-27]. Protonation can influence the structural stability and phase transition behavior of oxide materials [24]. The incorporation of protons can alter the lattice structure locally, leading to structural transition in complex oxides. Moreover, protonation also impacts the magnetic properties of oxide materials. For instance, in some oxide compounds [e.g., (La, Sr)MnO_3], the addition of protons can change the arrangement of magnetic moments, resulting in modifications in the magnetic behavior of oxides [25]. The control of physical properties in oxides by protonation offers a powerful tool for materials design and engineering, allowing for the tailoring of oxide materials to specific application requirements. The ability to manipulate oxide materials through protonation provides exciting opportunities for advancing materials research and developing novel functional materials with enhanced performance in a wide range of applications.

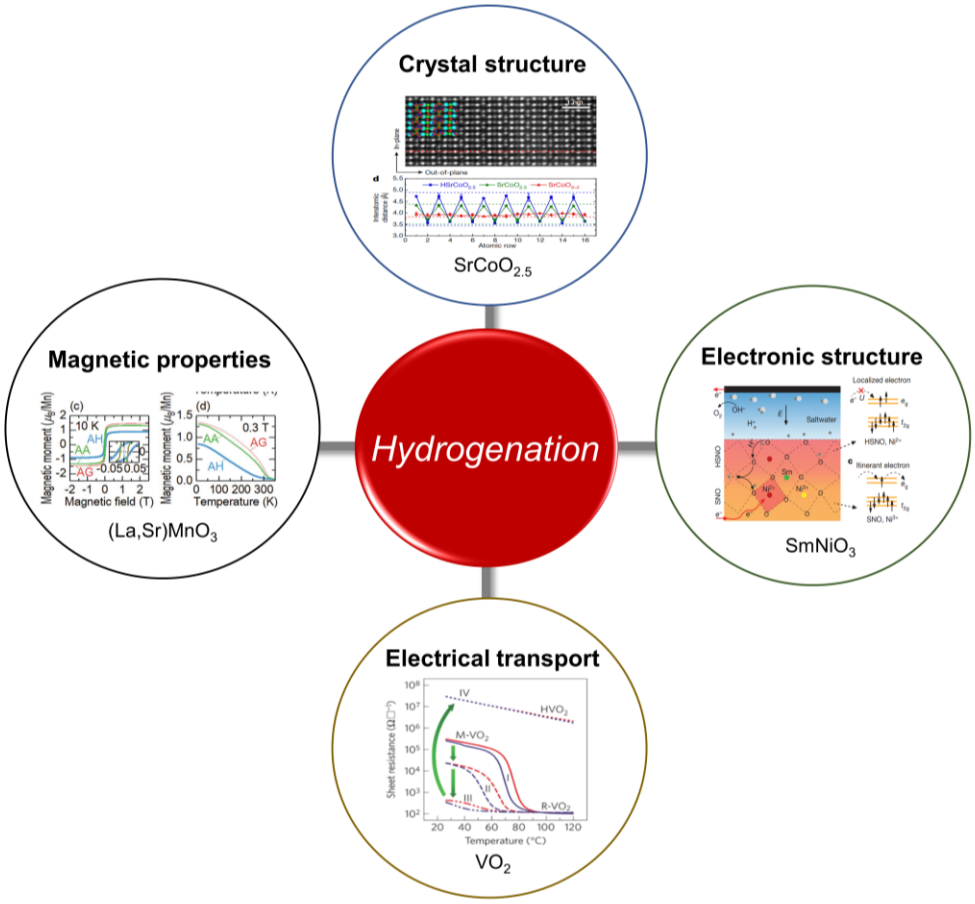

Figure 1.7 Reversible control of physical properties in complex oxides by hydrogenation [24-27].

1.4. Dielectric-based sensing applications

1.4.1. Multi-functional sensors with high efficiency and sensitivity

Dielectric materials with a high dielectric permittivity, which is manipulated by external stimuli, can be utilized for the realization of dielectric-based sensors with high performance. The dielectric-based sensors with multi-functionality have been designed to detect a variety of environmental parameters such as temperature, humidity, pressure, gas concentration, and so on. The change of electrical properties (e.g., dielectric permittivity) to the external stress is used as an

output signal of dielectric-based sensors. For example, in a capacitor type of gas sensors, the sensitivity to ambient gas environments is directly linked with a change of relative capacitance (proportional to a dielectric constant) under the ambient condition with respect to a reference condition [22]. It is therefore significant to design dielectric materials with the enhanced dielectric responses, which can be reversibly controlled by external stress, for the actual realization of oxide-based gas sensors with high sensitivity and efficiency.

1.4.2 Multi-Layer Ceramic Capacitor (MLCC)

Dielectric materials play a crucial role in the design of multi-layer ceramic capacitors (MLCCs). MLCCs are widely used in electronic devices, such as computers, smartphones, and automotive electronics [4, 28]. The geometry of a MLCC consists of alternating layers of metal electrodes and dielectric materials, as shown in Figure 1.8. The physical properties of a dielectric material strongly affect the device performance (i.e., capacitance, temperature stability, and reliability) of MLCCs [28, 29]. Therefore, dielectric materials with high dielectric constants, low losses, and stable electrical properties are ideal for MLCCs, resulting in higher capacitance values and better performance.

One of the commonly used dielectric materials in MLCCs is ferroelectric ceramic, which is known for its excellent electrical properties, including high dielectric constant and ferroelectricity. Nowadays, the barium titanate ($BaTiO_3$) ceramic is one of the common types of dielectric material used in multi-layer ceramic capacitors (MLCCs) [4, 28]. Ferroelectric $BaTiO_3$ ceramics, which exhibit a huge ferroelectric polarization, allow for higher capacitance values and better performance at high frequencies than non-ferroelectric dielectrics. Furthermore, it is also interesting that the intriguing physical phenomenon (e.g., magnetoelectric effect) is observed in

the $BaTiO_3$ based-multilayer capacitors, enabling the electrical devices with multi-functionality [30].

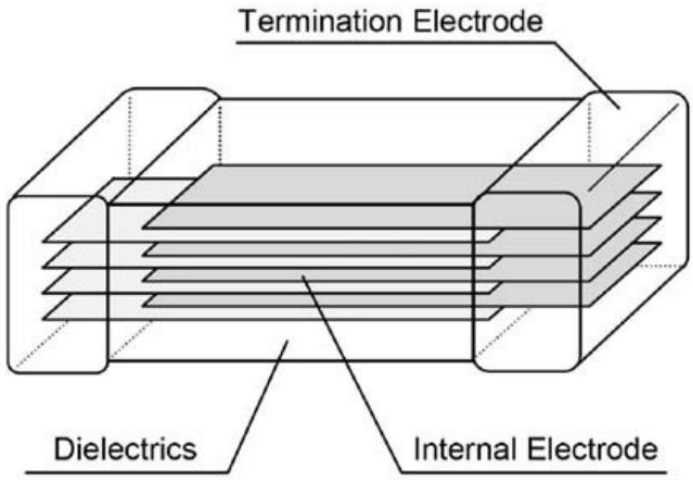

Figure 1.8 A illustration of the construction of a multi-layer ceramic capacitor.

1.5. Our strategy: Hydrogen control of relative permittivity in dielectric oxides

1.5.1. Hydrogenation to oxygen-deficient oxides through water dissociation

Up to now, there are various approaches to implement hydrogenation in complex oxide materials. Among them, the introduction of hydrogen ions (i.e., protonation) into the oxides via the dissociation of water molecules is a possible route, as shown in Figure 1.9. It should be noted that the dissociation of water molecules is energetically feasible at the defect sites (i.e., oxygen vacancy sites) on the surface of complex oxides [31, 32]. When the oxygen-deficient oxides incorporating large amounts of oxygen vacancy defects are exposed to the ambient environment containing water vapor, oxygen vacancies on the surface of oxides act as the active sites for the separation of water molecules into hydrogen ions (H^+) and hydroxyl ions (OH^-). The hydroxyl ions dissociated from water tend to be adsorbed at the oxygen vacancy sites. On the other hand, the

dissociated hydrogen ions from water molecules can come into the oxide materials, leading to changes in their chemical and physical properties [32, 33].

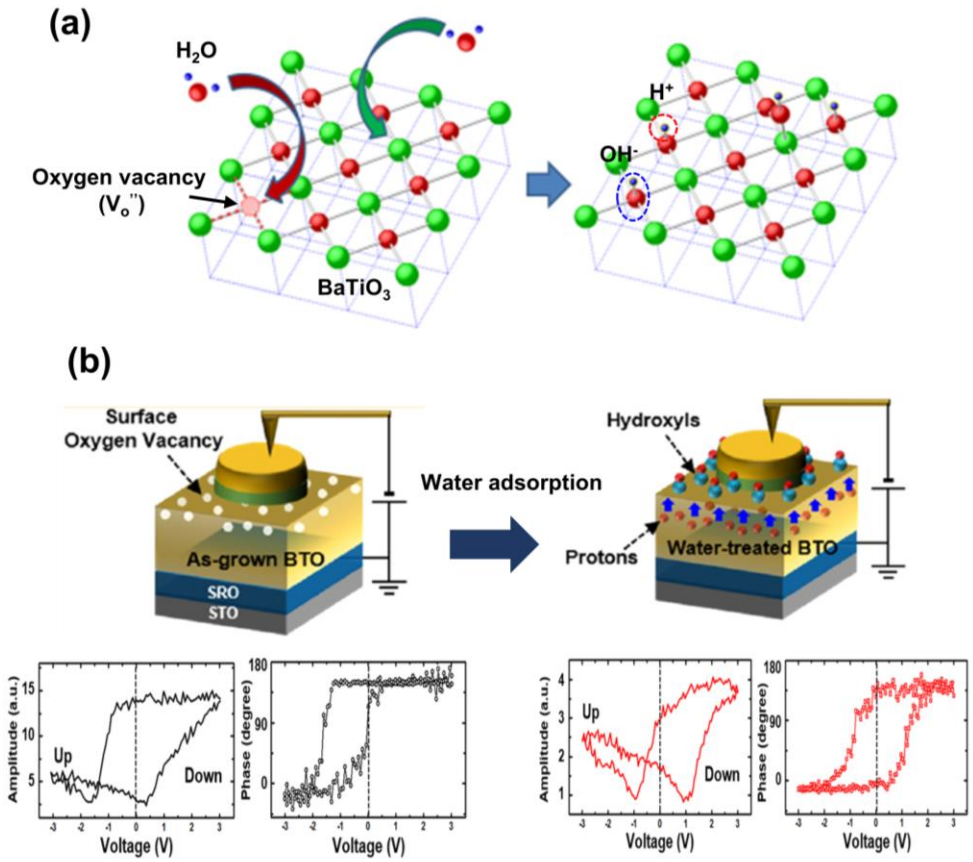

Figure 1.9 Introduction of hydrogen ions to oxygen-deficient oxides via water dissociation. (a) Oxygen vacancy defects as active sites for the water dissociation on the surface of complex oxides. (b) The introduction of hydrogen ions induces the modification in ferroelectric properties of $BaTiO_3$ thin films [32, 33].

1.6. Hypothesis

1.6.1. Protonation-driven ultrahigh dielectric constant in oxide ceramics

Here, we hypothesize that the high dielectric responses in oxygen-deficient oxide ceramics are induced by hydrogenation through water dissociation, as shown in Figure 1.10. The protonation to oxide ceramics can be achieved through a specific treatment under ambient environments. The oxide ceramics, which incorporate a large amount of oxygen vacancies, are treated under an ambient environment containing water vapor. We note that the dissociation of water molecules is energetically feasible at oxygen vacancy defects in complex oxides [31, 32]. When the water molecules come to the surface of ceramics, water molecules are dissociated into hydrogen ions (H^+) and hydroxyl ions (OH^-). The dissociated hydroxyls are adsorbed on the ceramic surfaces at the oxygen vacancy sites [33]. Considering that a proton (H^+) is the smallest ion with high mobility [34], the separated protons would be introduced into the oxygen-deficient ceramics. The hydrogen ion with an electrically positive charge can induce an internal electric field at a given lattice site. The internal field by incorporated protons can induce the local structural deformation with enhanced electric polarizability at an atomic level [33, 35]. The inhomogeneity in the local dielectric responses induced by hydrogenation can result in a substantial improvement in the overall dielectric permittivity of oxide ceramics.

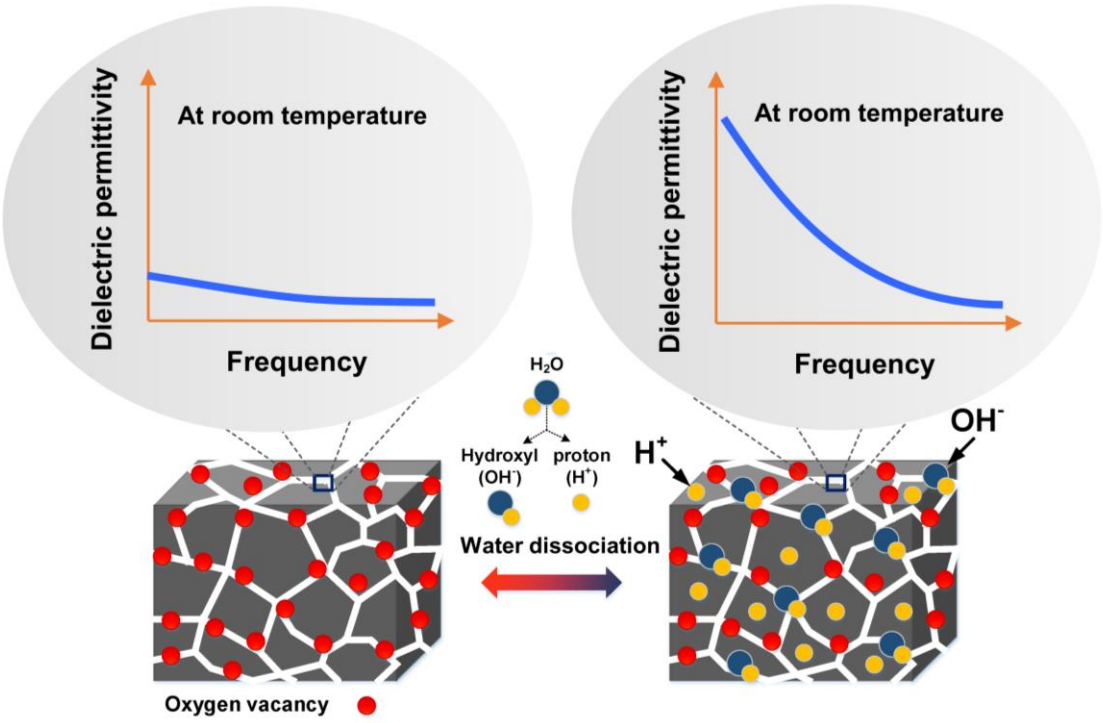

Figure 1.10 The schematic illustrates a hypothesis of a change in dielectric responses of oxide ceramics induced by hydrogenation via water dissociation.

1.6.2. 6H-hexagonal $BaTiO_3$: A material system for examining the protonation effect

To test our hypothesis, we chose the 6H-hexagonal $BaTiO_3$ as a platform to examine the protonation effect on the dielectric properties of complex dielectric oxides. It should be noted that a hexagonal polymorph is only achieved in the stoichiometric $BaTiO_3$ composition at an extremely high temperature (> 1460 °C) (the detailed crystal structure of the 6H-hexagonal $BaTiO_3$ polymorph is shown in Figure 1.11). Very recently, it has been experimentally demonstrated the stabilization of the hexagonal $BaTiO_3$ phase at room temperature by transition-metal substitution [36, 37]. Furthermore, the formation of oxygen vacancies by transition-metal substitution is closely related to the realization of 6H-hexagonal $BaTiO_3$ [36]. The oxygen-deficient $BaTiO_3$ ceramic with a 6H-hexagonal phase would be a suitable system to study the dielectric responses to the

hydrogenation in complex oxides. The protonation to the oxygen-deficient $BaTiO_3$ ceramics can be obtained through a treatment under ambient environments. When the water molecules in the ambient environment contact with the ceramics, oxygen vacancy defects on the surface facilitate the dissociation of water molecules into protons (H^+) and hydroxyls (OH^-). The dissociated hydrogen ions can be introduced in the 6H-hexagonal $BaTiO_3$ ceramics, leading to the modification in dielectric properties. Therefore, it is possible to tailor dielectric responses in oxygen-deficient $BaTiO_3$ ceramics by protonation.

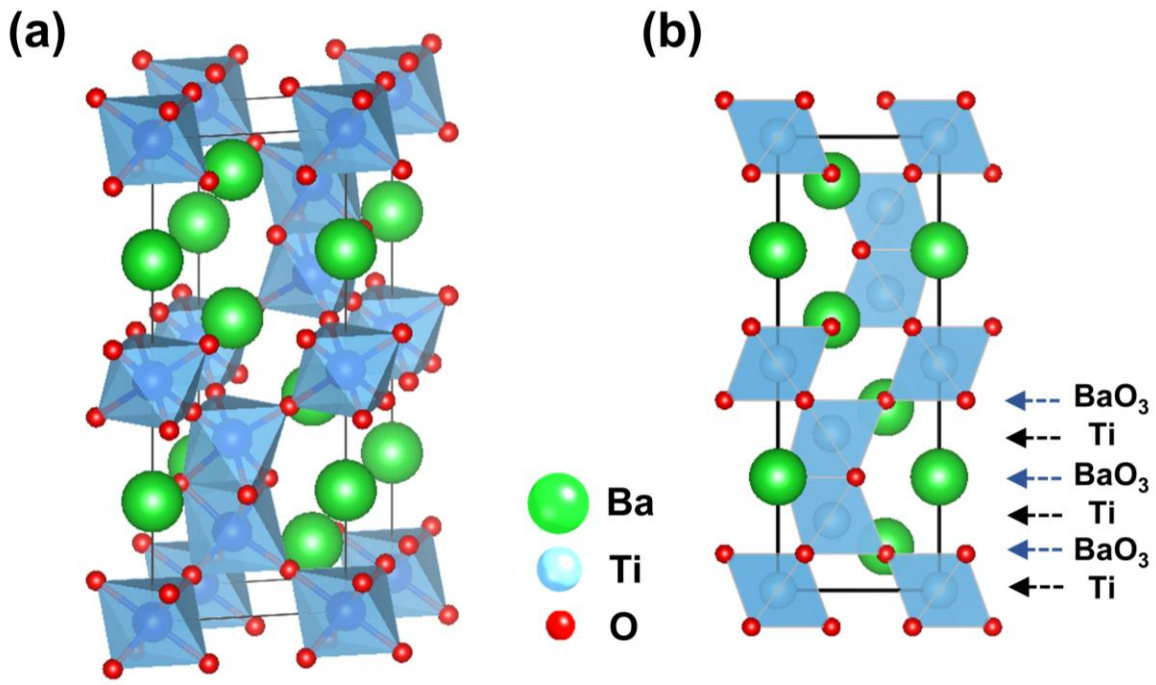

Figure 1.11 (a) A schematic 3D view of the 6H-hexagonal $BaTiO_3$ polymorph. (b) the hexagonal $BaTiO_3$ structure viewed along the $[11\bar{2}0]$ direction.

References

1. R. J. Tilley, *Understanding solids: the science of materials* (John Wiley & Sons, 2004).
2. S. O. Kasap, *Principles of Electronic materials and Devices* (McGraw-Hill New York, 2006).
3. K. C. Kao, *Dielectric phenomena in solids* (Elsevier, 2004).
4. A. I. Kingon, J.-P. Maria, S. Streiffer, *Nature* **406**, 1032-1038 (2000).
5. S. Krohns, P. Lunkenheimer, S. Meissner, A. Reller, B. Gleich, A. Rathgeber, T. Gaugler, H. U. Buhl, D. C. Sinclair, A. Loidl, *Nat. Mater.* **10**, 899-901 (2011).
6. S. C. B. Mannsfeld, B. C. K. Tee, R. M. Stoltenberg, C. V. Chen, S. Barman, B. V. O. Muir, A. N. Sokolov, C. Reese, Z. Bao, *Nat. Mater.* **9**, 859-864 (2010).
7. W. H. Ko, Q. Wang, *Sens. Actuator A Phys.* **75**, 242-251 (1999).
8. T. Ishihara, S. Matsubara, *J. Electroceramics* **2**, 215-228 (1998).
9. Y. Wang, W. Jie, C. Yang, X. Wei, J. Hao, *Adv. Funct. Mater.* **29**, 1808118 (2019).
10. C. C. Homes, T. Vogt, S. M. Shapiro, S. Wakimoto, A. P. Ramirez, *Science* **293**, 673-676 (2001).
11. R. Lo Nigro, R. G. Toro, G. Malandrino, M. Bettinelli, A. Speghini, I. L. Fragalà, *Adv. Mater.* **16**, 891-895 (2004).
12. H. Palneedi, M. Peddigari, G. T. Hwang, D. Y. Jeong, J. Ryu, *Adv. Funct. Mater.* **28**, 1803665 (2018).
13. M. Takesada, T. Yagi, M. Itoh, S.-y. Koshihara, *J. Phys. Soc. Jpn.* **72**, 37-40 (2003).
14. T. Nagai, K. Tanabe, I. Terasaki, H. Taniguchi, *Appl. Phys. Lett.* **113**, 212902 (2018).
15. T. Kimura, S. Kawamoto, I. Yamada, M. Azuma, M. Takano, Y. Tokura, *Phys. Rev. B* **67**, 180401 (2003).

16. R. S. Freitas, J. F. Mitchell, P. Schiffer, *Phys. Rev. B* **72**, 144429 (2005).

17. N. Hur, S. Park, P. A. Sharma, S. Guha, S.-W. Cheong, *Phys. Rev. Lett.* **93**, 107207 (2004).

18. S. Song, J. Zhai, L. Gao, X. Yao, *Appl. Phys. Lett.* **94**, 052902 (2009).

19. T. M. Shaw, Z. Suo, M. Huang, E. Liniger, R. B. Laibowitz, J. D. Baniecki, *Appl. Phys. Lett.* **75**, 2129-2131 (1999).

20. T. Hasegawa, S.-i. Mouri, Y. Yamada, K. Tanaka, *J. Phys. Soc. Jpn.* **72**, 41-44 (2003).

21. T. Goto, T. Kimura, G. Lawes, A. P. Ramirez, Y. Tokura, *Phys. Rev. Lett.* **92**, 257201 (2004).

22. P. M. Harrey, B. J. Ramsey, P. S. A. Evans, D. J. Harrison, *Sens. Actuators B Chem.* **87**, 226-232 (2002).

23. R. D. Shannon, *Acta Crystallogr. A* **32**, 751-767 (1976).

24. H. Yoon, M. Choi, T.-W. Lim, H. Kwon, K. Ihm, J. K. Kim, S.-Y. Choi, J. Son, *Nat. Mater.* **15**, 1113-1119 (2016).

25. J. Lee, Y. Ha, S. Lee, *Adv. Mater.* **33**, 2007606 (2021).

26. A. Janotti, C. G. Van de Walle, *Nat. Mater.* **6**, 44-47 (2007).

27. Z. Zhang, D. Schwanz, B. Narayanan, M. Kotiuga, J. A. Dura, M. Cherukara, H. Zhou, J. W. Freeland, J. Li, R. J. N. Sutarto, **553**, 68-72 (2018).

28. J. F. Scott, *Science* **315**, 954 (2007).

29. A. D. Milliken, A. J. Bell, J. F. Scott *, Appl. Phys. Lett.* **90**, 112910 (2007).

30. C. Israel, N. D. Mathur, J. F. Scott, *Nat. Mater.* **7**, 93-94 (2008).

31. R. Schaub, P. Thostrup, N. Lopez, E. Lægsgaard, I. Stensgaard, J. K. Nørskov, F. Besenbacher, *Phys. Rev. Lett.* **87**, 266104 (2001).

32. J. Shin, V. B. Nascimento, G. Geneste, J. Rundgren, E. W. Plummer, B. Dkhil, S. V. Kalinin, A. P. Baddorf, *Nano Lett.* **9**, 3720-3725 (2009).

33. H. Lee, T. H. Kim, J. J. Patzner, H. Lu, J.-W. Lee, H. Zhou, W. Chang, M. K. Mahanthappa, E. Y. Tsymbal, A. Gruverman, C.-B. Eom, *Nano Lett.* **16**, 2400-2406 (2016).

34. K. D. Kreuer, *Solid State Ion.* **125**, 285-302 (1999).

35. C. H. Park, D. J. Chadi, *Phys. Rev. Lett.* **84**, 4717 (2000).

36. G. M. Keith, K. Sarma, N. M. Alford, D. C. Sinclair, *J. Electroceramics* **13**, 305-309 (2004).

37. G. M. Keith, M. J. Rampling, K. Sarma, N. M. Alford, D. C. Sinclair, *J. Eur. Ceram. Soc.* **24**, 1721-1724 (2004).

Chapter 2

Experimental detail (method)

2.1. Material selection/synthesis: 6H-hexagonal $BaTiO_3$ by cation substitution

2.1.1. Phase stabilization of the 6H-hexagonal polymorph via a solid-state reaction method

We fabricated polycrystalline Ni-substituted $BaTiO_3$ ($BaTi_{1-x}Ni_xO_{3-\delta}$) samples with different nickel concentrations (x) ranging from 0 to 0.125 using the conventional solid-state-reaction method (as shown in Figure 2.1). To make the mixed powders, the raw materials of $BaCO_3$, TiO_2, and NiO (99.9% purity, High Purity Chemicals, Saitama, Japan) were combined in molar concentrations of 1: 1-x: x, respectively. The powders were then ball-milled with ethanol for 24 hours, dried, and calcined in an alumina crucible in a box furnace at 1100 ℃ for 8 hours in air. The calcined powders were ground, ball-milled again for 24 hours, and then dried to make fine powders with smaller grain sizes suitable for pelletizing. After that, we added polyvinyl-alcohol ($[CH_2CH(OH)]_n$) binder solution to the powders. Then, we molded a 1-inch-diameter pellet and pelletized it under a pressure of ~133 Pa. The Ni-substituted $BaTiO_3$ ceramic pellet was then sintered at 1330 ℃ for 6 hours in air to achieve crystallization.

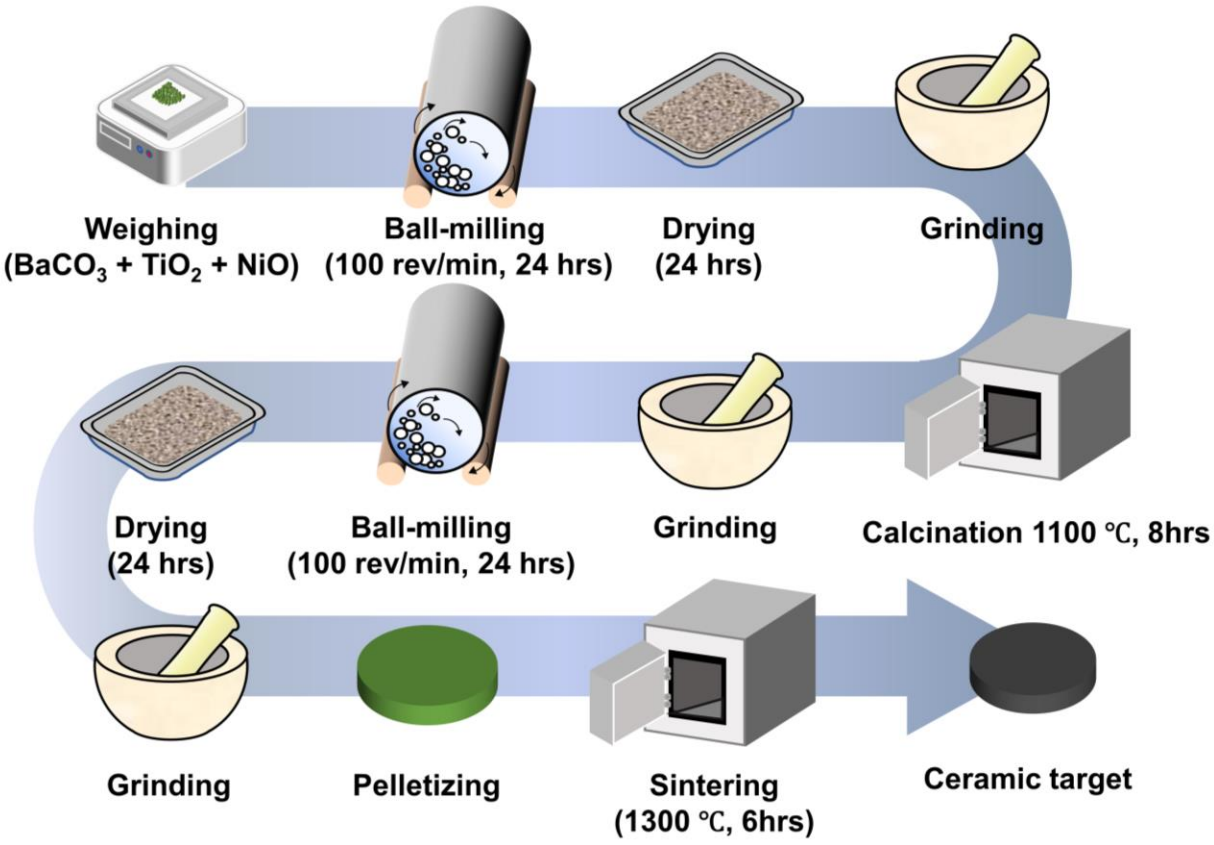

Figure 2.1 Synthesis of Ni-substituted $BaTiO_3$ ceramics by the conventional solid-state reaction method.

2.2. Material characterization

2.2.1. X-ray diffraction (XRD)

The structural properties of the Ni-substituted $BaTiO_3$ ($BaTi_{1-x}Ni_xO_{3-\delta}$) ceramics with different Ni contents ($0 \leq x \leq 0.175$) were analyzed using an x-ray diffractometer [wavelength $\lambda = 1.5406$ Å (Cu Kα), D8 Advance, Bruker, Germany] at room temperature.

2.2.2. Transmission electron microscopy (TEM)

Transmission electron microscopy samples of the Ni-substituted $BaTiO_3$ were prepared by the Ga ion beam milling method using a dual-beam focused ion beam system (Helios NanoLab 450, Thermo Fisher Scientific) and additionally milled by a low-energy Ar-ion milling system (Fishione Model 1040 Nanomill) to reduce damage at the surface layers of the samples. An aberration-corrected STEM (FEI Titan^3 G2 60-300) system was used to obtain ABF STEM images of the samples with the detector angle range of 12 to 24 mrad. The probe convergence semi-angle and the source size of the electron probe were 26 mrad and 0.9 Å, respectively.

2.2.3. X-ray photoelectron spectroscopy analyses

The K-Alpha+ XPS system (Thermo Fisher Scientific Inc., U.K) accompanied by a monochromated Al Kα x-ray source (hν = 1486.6 eV) with a spot size of 400 μm, was used to conduct x-ray photoelectron spectroscopy (XPS) measurements. Charge compensation of the x-ray photoelectron spectroscopy (XPS) samples was performed during analysis. The carbon C 1*s* peak of hydrocarbon at the binding energy of 284.6 eV was utilized as a reference to correct all the measured spectra. XPS analyses were conducted on both pure and Ni-substituted $BaTiO_3$ ceramics.

2.2.4. X-ray absorption spectroscopy measurements

X-ray absorption spectroscopy (XAS) analyses were measured in total electron yield (TEY) mode at 4D PES beamline in Pohang accelerator laboratory. The signal was obtained by measuring the sample current generated by photon irradiation, and normalized using an I_0 current measured by Au mesh in front of the samples to eliminate photon beam fluctuation.

2.2.5. Field emission scanning electron microscope (FE-SEM) and energy dispersive spectroscopy (EDS) analyses

We investigated the surface morphology and the chemical stoichiometry of our Ni-substituted $BaTiO_3$ ceramics by a field emission scanning electron microscope (FE-SEM, JSM-7600, JEOL, Japan) with an energy dispersive spectroscopy (EDS) detector.

2.2.6. Raman spectroscopy

To confirm a structural phase transition in our Ni-substituted $BaTiO_3$ ceramics, room-temperature Raman measurements were also carried out at a wavelength of 532 nm by using a conventional Raman spectrometer (LabRam HR800, Horiba, Co.). It is a high-throughput single-stage spectrometer with a grating of 1800 lines per mm. An optical microscope (BX41, Olympus) was used for acquiring Raman spectra at the backscattering geometry. The spectral resolution was about 2 cm^{-1}.

2.2.7. Polarization-electric field hysteresis and piezoresponse force microscopy (PFM) measurements

To assess the ferroelectric properties of our Ni-substituted $BaTiO_3$ ceramics, we conducted ferroelectric hysteresis loops (*P-E*) measurements using the aixACCT Ceramic Multilayer Actuator (aixCMA) test bench at 10 Hz under 5 kV/cm applied electric field. Additionally, we employed piezoresponse force microscopy (PFM) measurements to verify the ferroelectricity. The PFM measurements were carried out using a commercial atomic force microscope (AFM) machine (NX-10, Park system) and a conductive PtCr-coated AFM tip (TAP 190E-G, BudgetSensors). For PFM imaging, we applied an AC bias of 3 Vrms and 17.1 kHz frequency, and a lock-in amplifier (SR830, Stanford Research Systems) was used.

2.2.8. Dielectric constant measurements

The dielectric constant and loss of the samples were measured for their temperature dependence using an impedance analyzer (HP4192A) across a temperature range of 30 to 350 ℃ at three different frequencies of 1 kHz, 10 kHz, and 100 kHz. The frequency-dependent dielectric constant was also measured using a HIOKI 3522-50 analyzer within the frequency range of 1Hz to 100 kHz. It is worth noting that the impedance analyzer (HIOKI 3522-50) can measure tanδ values ranging from 0.00001 to 9.99999.

2.2.9. Impedance analyses

To investigate the temperature-dependent electrical characteristics of our Ni-substituted $BaTiO_3$ ceramics, we conducted impedance analyses for two different dielectric states, namely the off- and on-states. Before the electrical impedance measurements, we coated the top and bottom surfaces of the ceramic samples with silver pastes and cured them at 700 ℃ for 30 minutes. We also measured the frequency-dependent dielectric permittivity of each sample to ensure that the ceramic remained in the off- and on-states. The impedance measurements were carried out using a HIOKI 3522-50 analyzer over a temperature range of 20 to 180 ℃.

2.2.10. Time-of-flight secondary ion mass spectrometry measurements

TOF-SIMS experiments were performed with a Hybrid SIMS (ION-TOF GmbH, Münster, Germany) in KBSI Busan Center by using a pulsed 30 keV Bi_1 primary beam with a current 1.5 pA. The analyzed area used in this work is a square of 100 μm × 100 μm. Positive ion spectra were internally calibrated using H^+, H_2^+, CH_3^+, $C_2H_5^+$, $C_3H_7^+$ peaks and normalized to the respective secondary total ion yields. The chemical images of the analyzed area are recorded with 128 × 128

pixel resolution during the data acquisition. The depth profile is a square of 300 μm × 300 μm using Cesium beam 1 keV.

2.3. Chemical environment treatments for protonation

2.3.1. Hydrogenation to oxide ceramics through specific treatments under ambient environments

We systematically examined the hydrogenation effect on dielectric properties of Ni-substituted $BaTiO_3$ ceramics through a specific treatment under various ambient environments. To investigate the change in the dielectric permittivity of Ni-substituted $BaTiO_3$ ceramics under different environments, we first measured the dielectric constant of the ceramic capacitors in their as-sintered state before any treatment. After this, we performed a specific treatment on the ceramic samples and re-measured their dielectric properties for comparison purposes. We monitored the evolution of the dielectric responses of the ceramics under different ambient conditions: ambient air, vacuum, high humidity, N_2, CO_2, liquid water, and acetic acid (Figure 2.2 and Table 2.1).

Our first experiment aimed to examine the effect of ambient air on the dielectric responses of the Ni-substituted $BaTiO_3$ ceramics. We exposed the ceramic samples to the air environment at room temperature for a period of 6 weeks and then measured the dielectric permittivity of the samples after the air exposure. For the second experiment, we treated the as-sintered ceramics under vacuum and high humidity conditions. To investigate the dielectric characteristics of the ceramic samples in the vacuum state, we placed them in a desiccator with a low vacuum pressure of 380 Torr for one week. To investigate the effect of humidity, we filled a plastic tray with deionized water and placed it on the bottom of the desiccator. The ceramic specimens were then

placed above the water-filled tray to avoid direct contact with the liquid water. Finally, we closed the desiccator and purged the air inside to adjust the internal pressure to 380 Torr.

In our third experiment, we investigated the effects of ambient treatments under nitrogen (N_2) and carbon dioxide (CO_2) conditions. We placed the as-sintered ceramics in a vacuum desiccator and evacuated it to a pressure of 380 Torr. We then inserted N_2 and CO_2 gas into the desiccator until the internal pressure reached approximately 700 Torr. We repeated this procedure twice to ensure a sufficient amount of N_2 and CO_2 gas was present in the desiccator. (Figure 2.2 and Table 2.1).

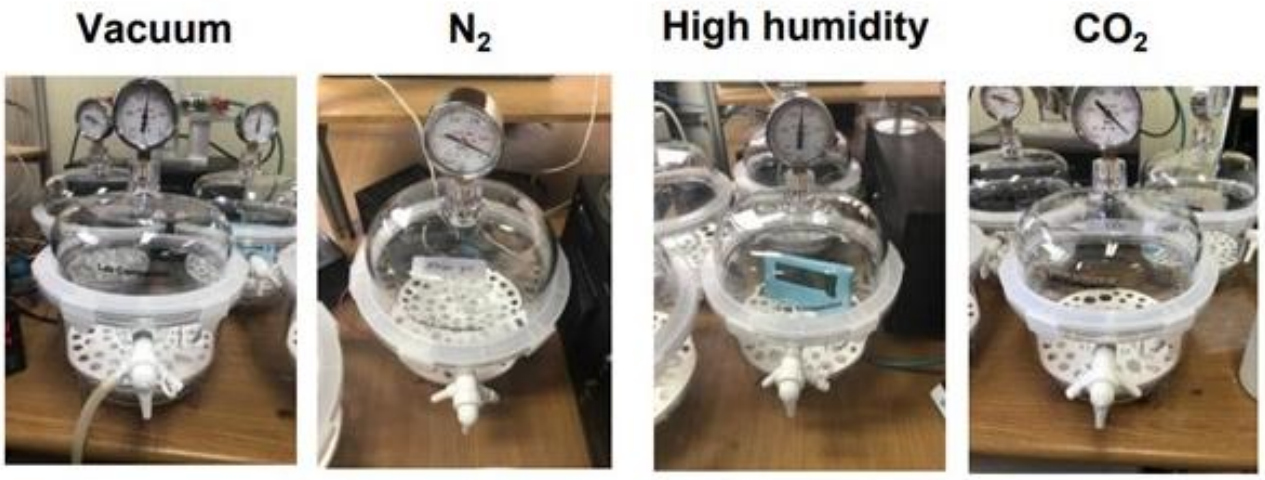

Figure 2.2 Experimental set-up of Ni-substituted $BaTiO_3$ ceramics under vacuum, nitrogen (N_2), carbon dioxide (CO_2), and high humidity environments.

Table 2.1 Base pressure, time duration, and description of various ambient treatments.

Treatment	Base pressure	Time duration	Description
Vacuum	~380 Torr	1 week	The sample under a low vacuum of ~ 380 Torr
Nitrogen (N_2)	~380 Torr	1 week	The sample under ~ 700 Torr of N_2
Carbon dioxide (CO_2)	~380 Torr	1 week	The sample under ~ 700 Torr of CO_2
High humidity	~380 Torr	2 days	The sample under a low vacuum of ~ 380 Torr with distilled water at the bottom of the desiccator

For the treatment of Ni-substituted $BaTiO_3$ ceramics by water, we treated the samples by immersing the as-sintered Ni-substituted $BaTiO_3$ ceramics in deionized water for 10 minutes at room temperature, followed by drying them under a flow of N_2 gas. To perform the treatment under acetic acid condition, an experimental setup was created to expose the ceramics to an acetic-acid-rich environment. The ceramic samples were placed in a beaker, which was then put at the bottom of a glass jar containing acetic acid. The jar was then closed, and the ceramics were left in the acetic acid environment for 2 days (Figure 2.3). After treatment, the treated Ni-substituted $BaTiO_3$ ceramics were removed from the jar and dried under a flow of N_2 gas before the dielectric measurements were taken.

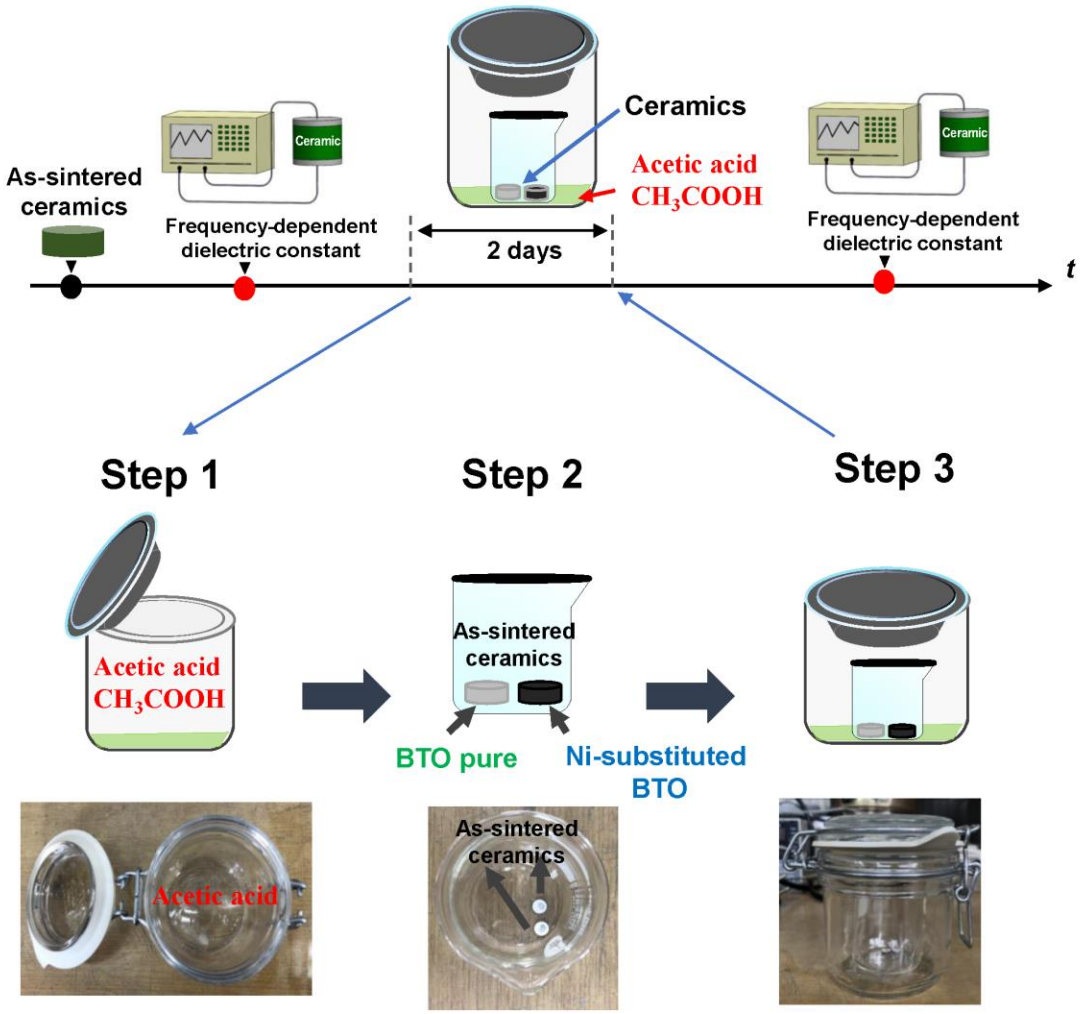

Figure 2.3 A schematic represented the experimental set-up of the acid acetic treatment.

2.4. Device tests for potential applications to multi-functional sensors

2.4.1. Sensing experiments in the 6H-hexagonal $BaTiO_3$ ceramics

To evaluate the humidity sensing capabilities of our Ni-substituted $BaTiO_3$ ceramics, we conducted a sensing experiment depicted in Figure 2.4. The experiment involved measuring the humidity-sensing properties of the ceramic samples in a quartz tube (a diameter of 3 cm and length of 30 cm) at room temperature. To achieve relative humidity levels ranging from 20-80 RH%, we

calibrated the humidity environment by mixing dry air with water vapor. The flow rate of humidity gas was maintained at 1000 sccm, which was controlled by a mass-flow controller (MFC). We used a Keithley 2401 source meter to measure the electrical conductivity of ceramic samples, with a *dc* bias voltage of 0.5 V, and all conductivity data were recorded by a home-made LabVIEW software.

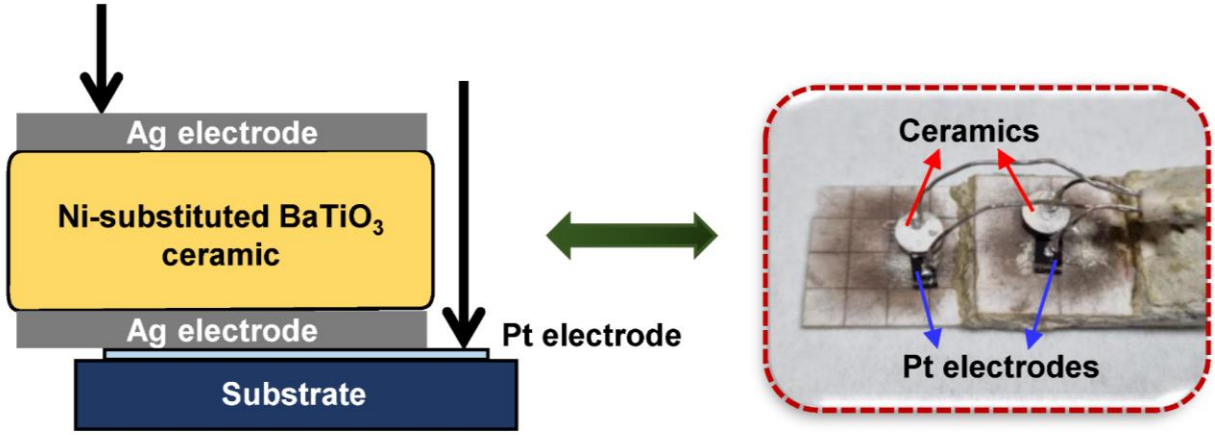

Figure 2.4 Experimental set-up of humidity sensing experiments

Chapter 3

Polymorphic phase transition in $BaTiO_3$ by Ni substitution

3.1. Structural phase transition in complex oxides

A structural phase transition is a phenomenon in which a material undergoes a change in its crystal structure due to changes in external conditions such as temperature, pressure, or magnetic field. Understanding a structural phase transition in complex oxides is of great significance for exploring exotic physical phenomena and for realizing potential applications to new multi-functional devices. Note that the complex oxides mostly undergo the phase transition, where new physical phenomena appear [1]. Therefore, it is important to understand the mechanism of the associated phase transition to clarify the emergence of unusual physical properties.

3.2. Crystallographic structure and structural phase transition in $BaTiO_3$

Barium titanate ($BaTiO_3$) is a well-known oxide material that has captured the significant attention of researchers due to its unique properties and potential applications in various fields [2]. The $BaTiO_3$ material has five different crystallographic structures. In the perovskite polymorphs of $BaTiO_3$, it undergoes a structural phase transition as temperature increases with four different polymorphic phases: rhombohedral (R3*m*), orthorhombic (A*mm*2), tetragonal (P4*mm*), and cubic (P$m\bar{3}m$), as shown in Figure 3.1 [3]. On the other hand, there is another polymorph of $BaTiO_3$ (hexagonal phase h-$BaTiO_3$, P6_3/*mmc*), which is only stable at very high temperatures above 1460 °C for the stoichiometric composition [4, 5]. As a result, limited research has been conducted on the hexagonal $BaTiO_3$ polymorph due to the difficulty in synthesizing. Hence, the associated physical properties of h-$BaTiO_3$ have been rarely reported in previous literature, too [6].

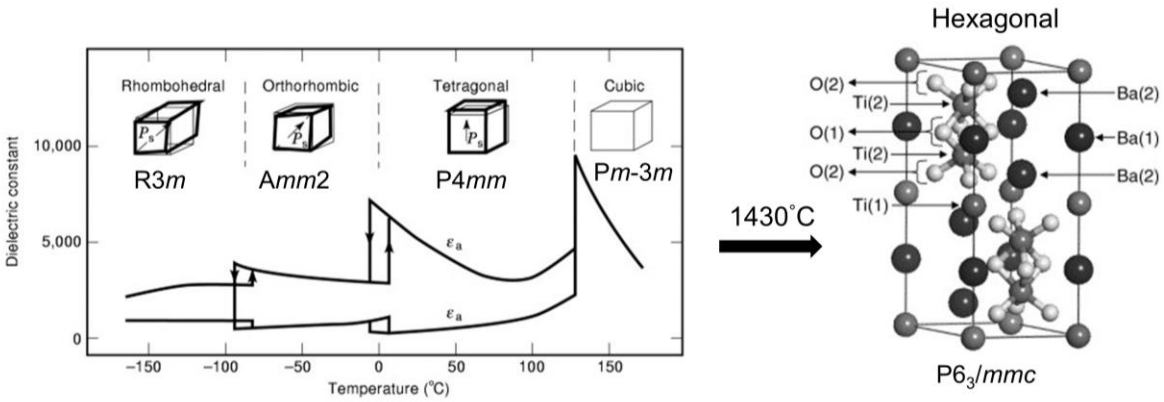

Figure 3.1 The schematic illustration of the polymorphic phase transition in perovskite $BaTiO_3$ with increasing temperature [3].

3.3. Hypothetical realization of 6H-hexagonal $BaTiO_3$ polymorph by cation substitution

The structural phase transition in $BaTiO_3$ could be induced by chemical substitution. Recently, some researchers have demonstrated through experiments that it is possible to achieve the hexagonal phase of $BaTiO_3$ at room temperature by doping certain transition-metal ions (such as Fe^{3+}, Co^{3+}, Mn^{4+}, Ni^{2+}, etc.) into pure $BaTiO_3$ [7-11]. If an acceptor, which has a smaller oxidation state than Ti^{4+}, replaces a B-site Ti^{4+} site, it leads to the creation of oxygen vacancies ($V_O^{\bullet\bullet}$) to compensate for the overall charge neutrality, resulting in the local change from Ti^{4+} to Ti^{3+} [12]. For instance, the replacement of Ti^{4+} with Ni^{2+} is expected to produce an oxygen vacancy following the chemical reaction [11].

$$NiO \xrightarrow{TiO_2} Ni''_{Ti} + O_o + \frac{1}{2}O_2\uparrow + V_o^{\bullet\bullet}$$

An interesting observation is that a polymorphic transition from tetragonal perovskite to hexagonal $BaTiO_3$ is obtained with the formation of oxygen vacancies, leading to stabilizing the h-$BaTiO_3$ at room temperature (see Figure 3.2) [10, 13-16]. It should be noted that the ferroelectric

distortion in the tetragonal $BaTiO_3$ is a result of weakened short-range Coulomb repulsion by Ti-O bonding [17-19]. By cation substitution, a tetravalent Ti^{4+} ion is substituted with a transition metal ion with a lower oxidation state (e.g., Ni^{2+} [11], Fe^{3+} [7], and Co^{3+} [9]), which degenerates the Ti-O hybridization. Thus, long-range ferroelectric ordering becomes unstable due to the restored short-range repulsion, and then the cubic phase becomes energetically favorable with paraelectricity [17]. The addition of such a transition-metal cation (such as Ni^{2+}) into the cubic $BaTiO_3$ can lead to a subsequent structural transition to the hexagonal phase [9-11]. Although the stabilization of the hexagonal phase in oxygen-deficient $BaTiO_3$ is previously reported [8, 9, 16, 20, 21], the exact underlying mechanism of the oxygen-vacancy-driven hexagonal phase transition is still uncertain and remains under debate. Therefore, it is highly essential to conduct systematic experimental studies to further understand the polymorphic phase transition and the related physical properties in the hexagonal $BaTiO_3$.

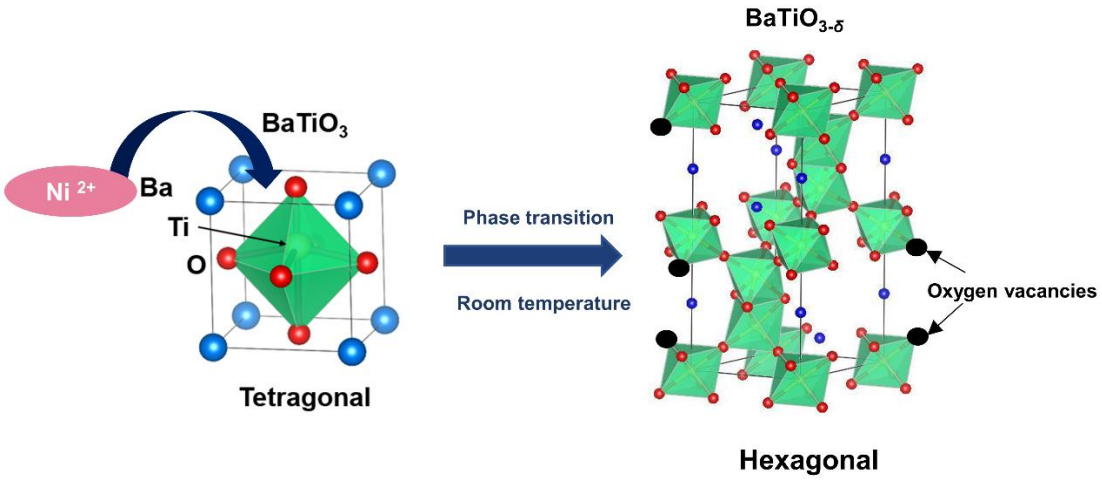

Figure 3.2 Schematic diagram of tetragonal-hexagonal phase transition in $BaTiO_3$ at room temperature induced by Ni substitution.

This research describes a polymorphic transition in $BaTiO_3$ ceramics induced by the substitution of Ni ions. As the concentration of Ni (x) increases, the original tetragonal structure transforms into a hexagonal structure. We also discuss a plausible mechanism of the oxygen-vacancy-mediated polymorphic phase transition in Ni-substituted $BaTiO_3$ ceramics according to the microscopic analyses of the crystal structure and electronic configuration.

3.4. Polymorphic phase transition in $BaTiO_3$ ceramics by Ni substitution

3.4.1. Structural evolution depending on Ni concentration

Figure 3.3 displays the results of the x-ray diffraction (XRD) theta-2theta (θ-2θ) in both pure and Ni-substituted $BaTiO_3$ ceramics. In the case of pure $BaTiO_3$, the Bragg peaks observed in the XRD pattern align with the peak positions of a reference tetragonal $BaTiO_3$ pattern. However, for Ni-substituted $BaTiO_3$, the appearance and eventual dominance of the diffraction peak corresponding to the hexagonal $BaTiO_3$ polymorph (as $x > 0.03$) indicates a transition from the tetragonal to the hexagonal phase.

In order to provide a clearer demonstration of the structural transition in Ni-substituted $BaTiO_3$, we examined the evolution of Bragg peaks around the 2θ angle of 45˚ as a function of Ni concentration (x), as depicted in Figure 3.3(b). It should be noted that tetragonal $BaTiO_3$ can exist in two different crystallographic structures (c- and a-domains). In the c-domain configuration, the crystallographic c-axis is oriented along the out-of-plane direction with a lattice parameter of 4.036 Å, while the c-axis is in the in-plane direction with a lattice constant of 3.992 Å for the a-domain [22]. Due to the multi-domain structure of tetragonal $BaTiO_3$, the diffraction peaks of the (002) and (200) lattice planes are observed with different 2θ angles of 44.78 and 45.24˚, respectively. As x increases, the Bragg peaks of (002) and (200) in tetragonal merge to a single peak around the

angle of 45.05˚ [23]. This may be attributed to a tetragonal-to-cubic structural transition in bulk $BaTiO_3$, particularly at x = 0.03 [24].

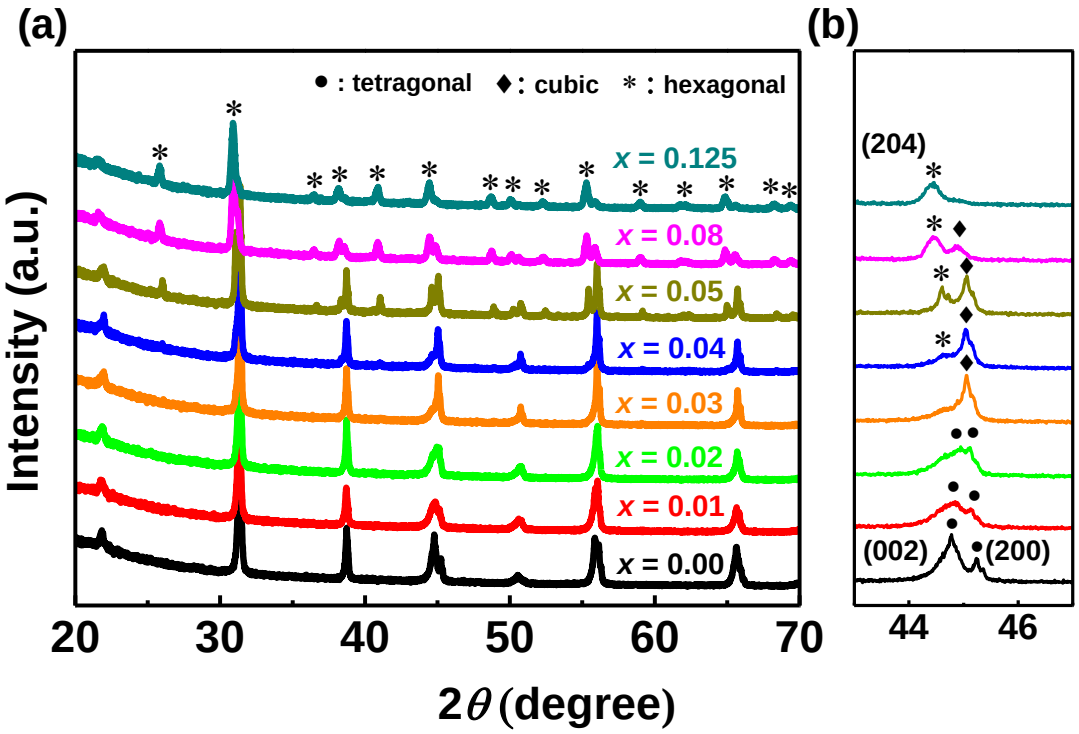

Figure 3.3 (a) X-ray diffraction (XRD) patterns of as-sintered Ni-substituted $BaTiO_3$ ceramics with various Ni concentrations (x). (b) The evolution of the XRD pattern around the 2θ angle of 45˚ as a function of x. In tetragonal $BaTiO_3$ (x = 0.00), two separated diffraction peaks [i.e., (002) and (200)] are obtained due to the multi-domain configuration of the tetragonal c and a domains. With the increase of x, the (204) diffraction peak of a hexagonal $BaTiO_3$ phase is observed, indicating the occurrence of a tetragonal-to-hexagonal phase transition in Ni-substituted $BaTiO_3$ ceramics.

$BaTiO_3$ with high levels of substitution, particularly x values greater than 0.03, will form a hexagonal phase. The presence of the (204) Bragg peak at an angle of 44.39˚ is attributed to the hexagonal $BaTiO_3$ phase. The (204) hexagonal peak becomes more prominent with increasing

concentrations of Ni, indicating that hexagonal polymorphs are energetically preferred during the tetragonal-cubic-hexagonal structural transition in Ni-substituted $BaTiO_3$ [7, 11, 20]. Our XRD analysis revealed that a tetragonal phase is still present at Ni concentrations below the critical value of $x = 0.03$, while the hexagonal phase is favored when the concentration is above $x = 0.03$.

Raman spectroscopy measurements of our Ni-substituted $BaTiO_3$ ceramic samples also confirmed the polymorphic transition (Figure 3.4). In Raman pattern of pure $BaTiO_3$ (black solid curve in Figure 3.4), we obtained the peaks at 260, 303, 517, 720 cm^{-1}, which are in agreement with the characteristic vibration modes of a tetragonal $BaTiO_3$ phase [25]. These peaks are assigned to the A_1(TO), E(TO+LO) and B_1, A_1(TO) and E(TO), A_1(LO) and E(LO) vibration modes (marked by the dash lines), respectively. In comparison with the XRD data, we noted that the initial structure of pure $BaTiO_3$ exhibits a tetragonal symmetry. The typical modes of the tetragonal $BaTiO_3$ structure remain in the spectra of Ni-substituted $BaTiO_3$ at $x = 0.03$ (blue solid line) without additional peaks compared to spectrum of pure sample. It indicates that the tetragonal structure remains in Ni-substituted $BaTiO_3$ with a Ni concentration lower $x = 0.03$. It is interesting to note that the intensity reduction of vibration mode around 303 cm^{-1} associated with the Ti displacement in TiO_6 octahedra, could explain the structural transformation from tetragonal to cubic by a low Ni concentration. In Raman spectroscopy pattern of $x = 0.125$ (red solid line), the peaks at 148, 220, 630 cm^{-1} emerge (marked by the arrows). According to the previous report [11, 25], these peaks are well matched with the modes of a $BaTiO_3$ hexagonal phase.

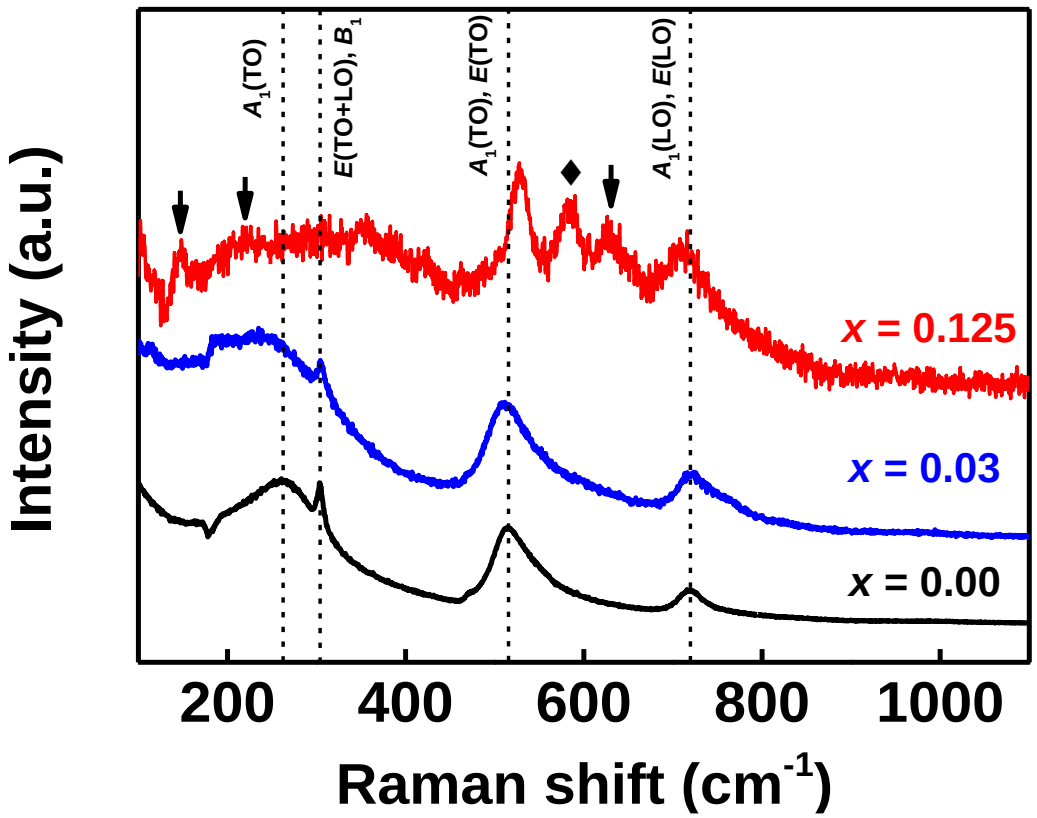

Figure 3.4 Raman spectra of Ni-substitution $BaTiO_3$ at different Ni concentrations (x = 0.00, 0.03, and 0.125).

The vibration mode around 630 cm^{-1} is attributed to the vibration of Ti ion in a hexagonal structure. The existence of mode around 585 cm^{-1} obtained in spectrum [marked by the diamond (♦)] could be explained by the substitution of Ni ions with a higher atomic mass into Ti ion sites in structure [26]. To understand clearly, we consider the frequency of a simple harmonic oscillator:

$$f = \frac{1}{2\pi}\sqrt{\frac{k}{m}}$$

where m is atomic weight, k is the force constant.

The ratio between the frequency of vibration of Ti ion and that of Ni ion replacing Ti sites can be calculated according to the following equation:

$$\frac{f_{Ti}}{f_{Ni}} = \sqrt{\frac{m_{Ni}}{m_{Ti}}}$$

The relationship between wavenumber and frequency of an oscillator is:

$$k = \frac{2\pi}{\lambda} = \frac{2\pi f}{v}$$

where λ, v are wavelength and wave velocity, respectively.

The wavenumber ratio of two vibrations, one is the vibration of Ti ion, and the other one is that of Ni ion replacing into Ti site could be estimated by the equation below:

$$\frac{k_{Ti}}{k_{Ni}} = \frac{f_{Ti}}{f_{Ni}} = \sqrt{\frac{m_{Ni}}{m_{Ti}}} = 1.107$$

where the atomic weights of Ni and Ti are 58.7 and 47.87 (u), respectively.

This wavenumber ratio value of these two vibration modes calculated from Raman data is:

$$\frac{k_{Ti}}{k_{Ni}} = \frac{630}{585} = 1.077$$

The two values, one estimated from difference of atomic weight and the other one calculated from the wavenumber of modes in experimental data, are quite close, which strengthens the supposition that the vibration mode around 585 cm^{-1} is generated by the vibration of Ni ions incorporated into the Ti ion positions. It is also strong evidence of the substitution of Ni into B sites in the perovskite structure.

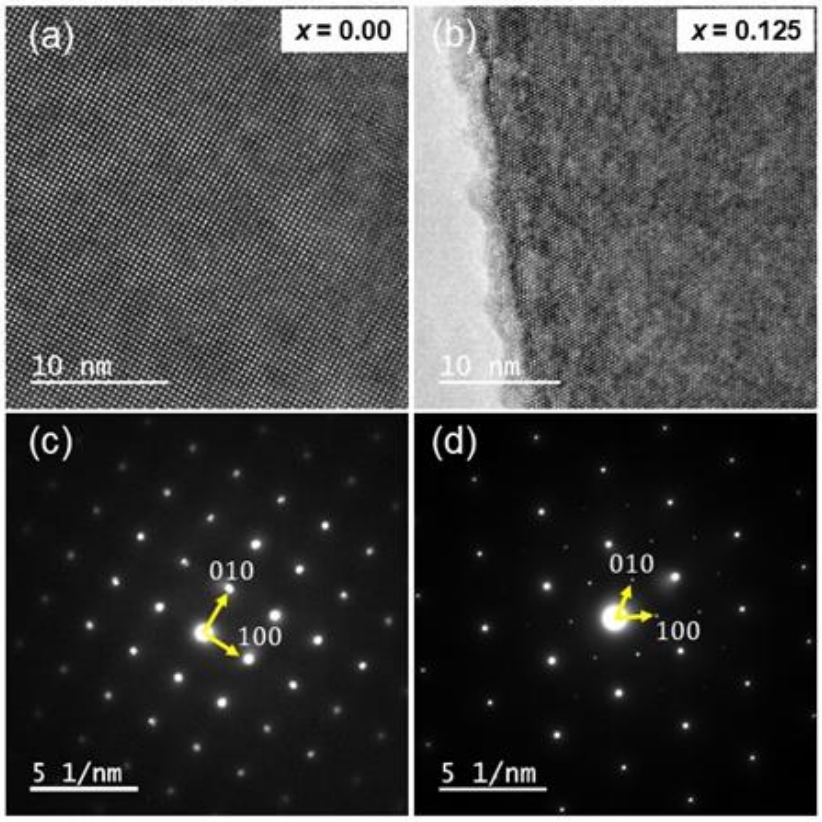

Figure 3.5 High-revolution transmission electron microscopy (HRTEM) images of (a) pure $BaTiO_3$, and (b) Ni-substituted $BaTiO_3$ at x = 0.125. The corresponding selected area electron diffraction (SAED) patterns taken along [001] zone axis of Ni-substituted $BaTiO_3$ at (c) x = 0.00, (d) and x = 0.125.

TEM measurements are performed to confirm the structural transition from tetragonal to hexagonal polymorph induced by Ni substitution. The phase contrast images are captured from pure $BaTiO_3$ and Ni-substituted $BaTiO_3$ ceramics (with a Ni concentration of x = 0.125) along the [001] zone axis [Figure 3.5(a) and (b)] and corresponding electron spot patterns [Figure 3.5(c) and (d)] are obtained. The spot patterns are indexed based on the reference crystallographic information of $BaTiO_3$, as shown in Figure 3.6. The correspondence between the simulated [Figure 3.6(a)] and the experimental [Figure 3.6(c)] ED patterns of a pure $BaTiO_3$ at the zone axis of [001]

indicate that the pure sample agrees with the tetragonal phase [P4*mm* ($a = b$ = 3.991 Å, c = 4.041 Å, $\alpha = \beta = \gamma = 90°$)]. Whereas the recorded electron spot pattern of Ni-substituted $BaTiO_3$ (x = 0.125) [Figure 3.6(d)] at the zone axis of [001] is indexed according to the simulated pattern [Figure 3.6(b)] of a hexagonal $BaTiO_3$ [$P6_3/mmc$ ($a = b$ = 5.724 Å, c = 13.965 Å, $\alpha = \beta = 60°$, $\gamma = 120°$)].

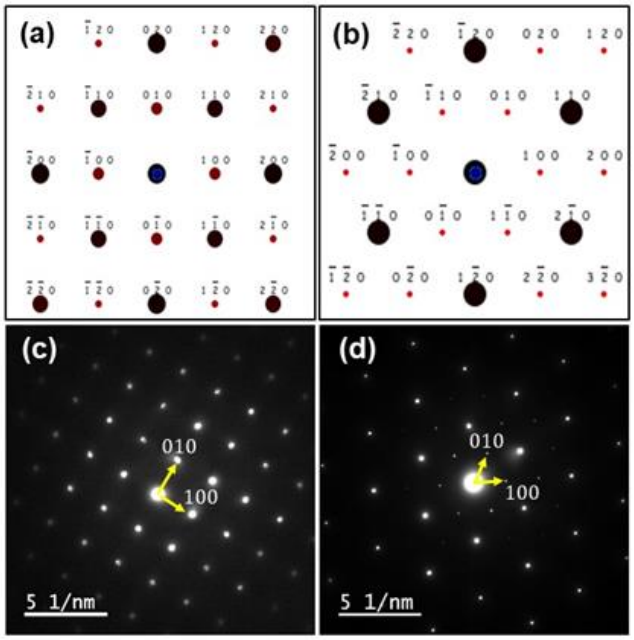

Table 1

crystallographic data of spot pattern simulation $BaTiO_3$			
Space group	P4*mm*	Space group No.	99
a	3.9905 Å	α	90°
b	3.9905 Å	β	90°
c	4.0412 Å	γ	90°

Table 2

crystallographic data of spot pattern simulation $BaTiO_3$			
Space group	P63/*mmc*	Space group No.	194
a	5.7238 Å	α	90°
b	5.7238 Å	β	90°
c	13.9649 Å	γ	120°

Figure 3.6 The electron diffraction (ED) pattern simulations and [experiments] of (a) [(c)] pure $BaTiO_3$, and (b) [(d)] Ni-substituted $BaTiO_3$ at x = 0.125. Tables 1 and 2 show the space groups and lattice parameters of pure and x = 0.125, respectively.

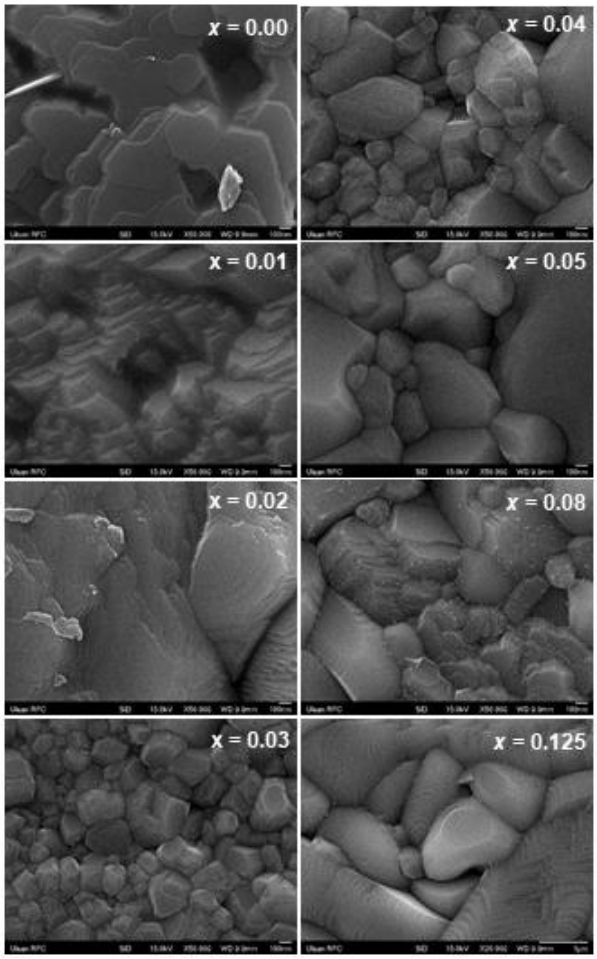

Figure 3.7. The SEM images of Ni-substituted $BaTiO_3$ at different Ni concentrations.

To investigate the surface morphology, the scanning electron microscope (SEM) measurement was carried out for Ni-substituted $BaTiO_3$ ceramics at various Ni levels. For SEM measurement, the as-sintered samples were polished the surfaces, and then, thermally etched at 1300 °C for 1 hour. As shown in Figure 3.7, the stripe patterns are observed in the SEM images of the compositions at x = 0.00, 0.01, and 0.02. It may be attributed to the mixed structures of two

domains ($c + a$) in tetragonal $BaTiO_3$. The shape of grains transforms into the circular shape at $x = 0.03$, at which the Ni-substituted $BaTiO_3$ is a cubic phase. The formation of the hexagonal phase at higher doping concentrations ($x > 0.03$) could explain the increasing average grain size at the surface with the increasing Ni content.

3.4.2. Ferroelectric-paraelectric-dielectric phase transition in $BaTiO_3$ by Ni substitution

We also examine the relation between ferroelectricity and structural phase transition in Ni-substituted $BaTiO_3$ ceramics. We performed measurements of the polarization-electric field (*P-E*) hysteresis loops of the ceramics at different Ni concentrations (x). The results depicted in Figure 3.8(a) reveal that the pure $BaTiO_3$ ($x = 0.00$) exhibits a *P-E* loop of a ferroelectric material with a distinct hysteretic characteristic. As the Ni concentration increases, the original ferroelectric hysteresis loop of pure $BaTiO_3$ becomes slanted, and the ferroelectric hysteresis is weakened. At Ni concentrations of $x = 0.03$ or 0.04, the corresponding *P-E* loop displays negligible hysteresis, closely resembling that of paraelectric $BaTiO_3$ with cubic symmetry. In Ni-substituted $BaTiO_3$ ceramics with higher Ni contents ($x > 0.05$), we found that the measured *P-E* loops are characteristic of dielectric materials, which are linear with a slight hysteresis [23, 27]. We also note that electrical leakage current causes hysteretic behaviors in lossy dielectrics, resulting in the *P-E* loop adopting an open elliptical curve with a linear shape [28].

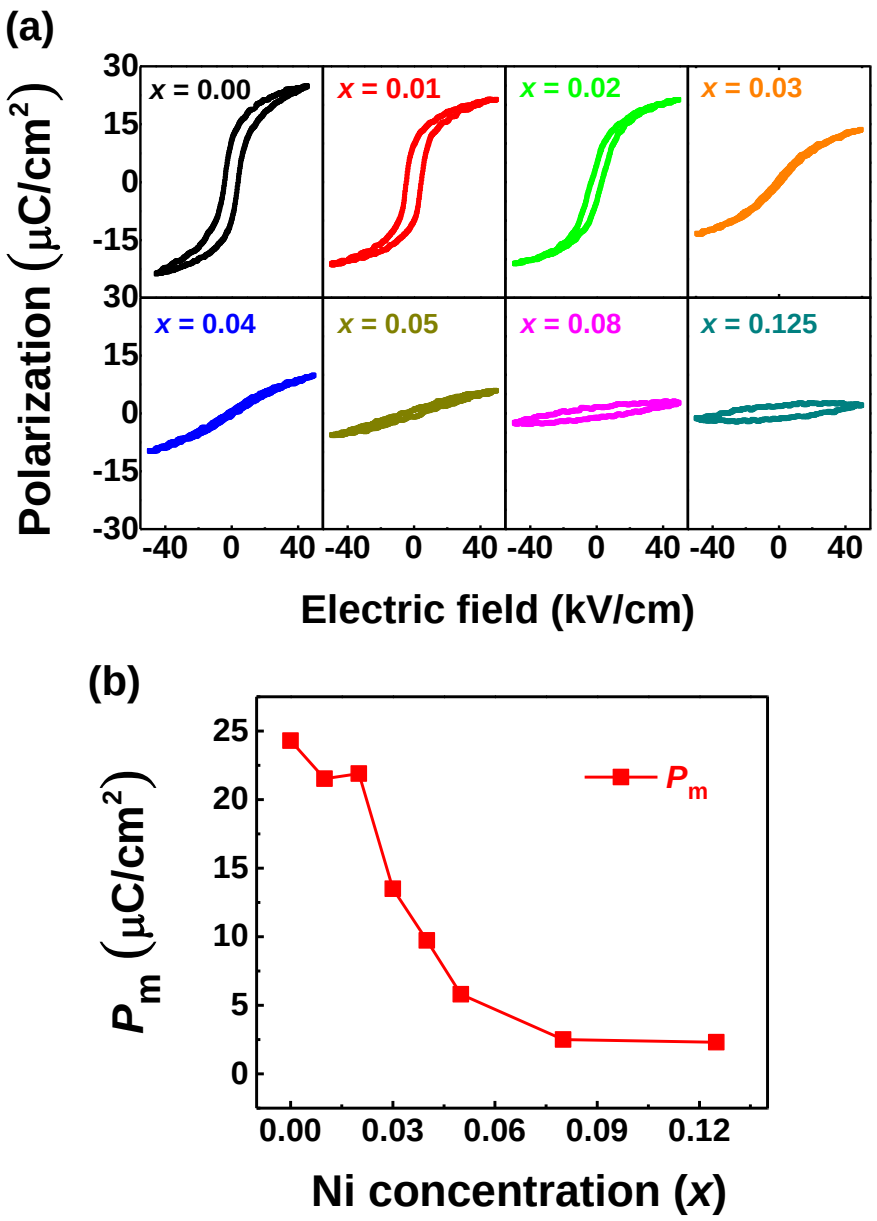

Figure 3.8 (a) *P*-*E* hysteresis loops of the Ni-substituted $BaTiO_3$ ceramics under external electric fields (i.e., triangular pulse fields with the amplitude of 50 kV/cm and the frequency of 10 Hz). (b) The Ni concentration (x) dependence of the maximum polarization (P_m) in the measured *P*-*E* loops. It is highly likely that the Ni-substituted $BaTiO_3$ ceramics undergo a ferroelectric-paraelectric-dielectric phase transition with the increase of Ni content.

To clearly illustrate the phase transition from ferroelectric to paraelectric to dielectric, we plot a graph [Figure 3.8(b)] showing the maximum polarization values (P_m) in the *P-E* loops as a function of Ni concentrations. For values of *x* less than 0.03, the P_m remains around 22 $\mu C/cm^2$, indicating the presence of long-range ferroelectric ordering in tetragonal $BaTiO_3$. However, as *x* increases above 0.03, the maximum polarization declines rapidly due to paraelectric ordering in cubic $BaTiO_3$. At Ni concentrations exceeding 0.05, the P_m approaches zero, indicating a transition to a dielectric phase. Our piezoresponse force microscopy (PFM) measurements revealed that pure $BaTiO_3$ has a higher amplitude in piezoresponse compared to Ni-substituted $BaTiO_3$, which is consistent with the observed dependence of P_m on Ni concentration (refer to Figure 3.9 for more information). As our Ni-substituted $BaTiO_3$ ceramics undergo a structural transition from tetragonal to cubic to hexagonal as *x* increases (as depicted in Figure 3.3), the hexagonal $BaTiO_3$ attained through heavy Ni substitution is expected to be dielectric.

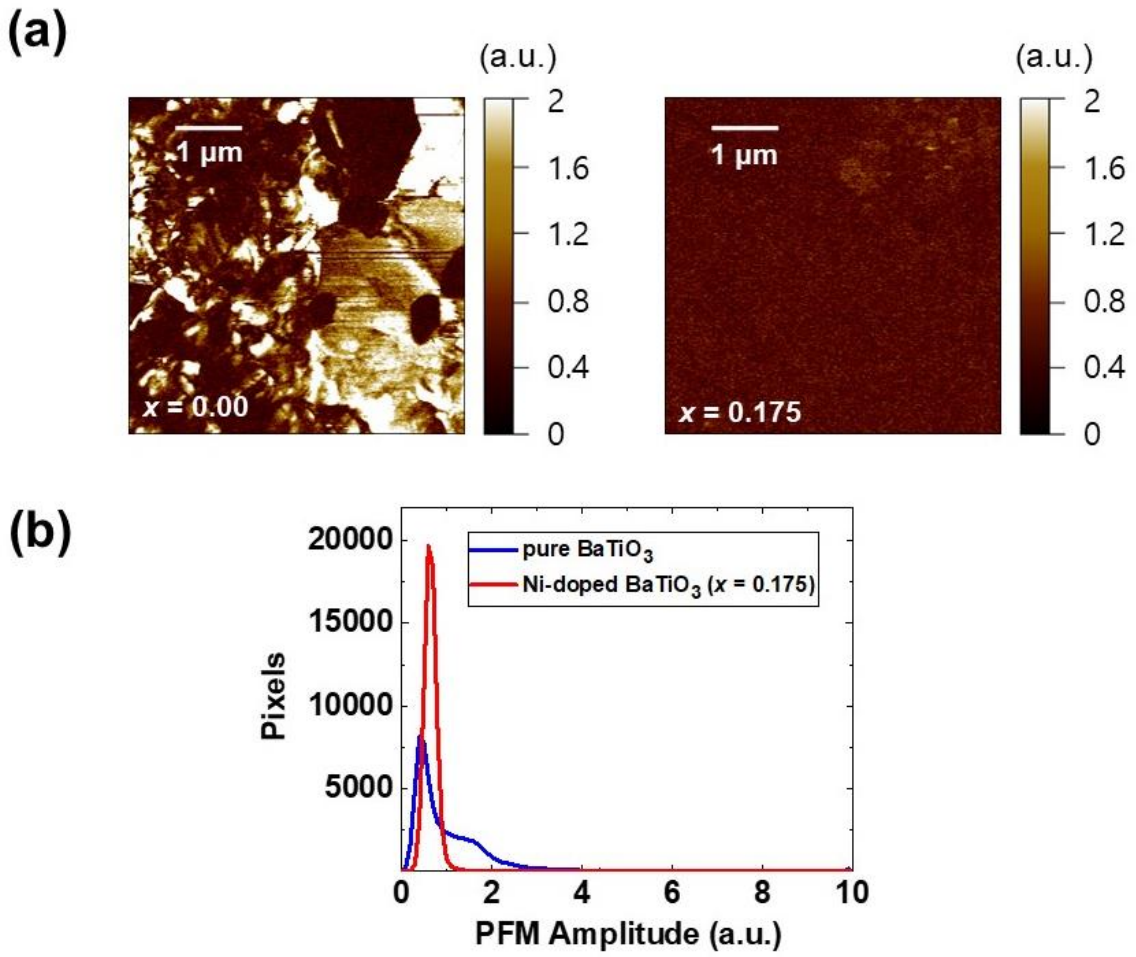

Figure 3.9 (a) Out of plane PFM amplitude images of pure $BaTiO_3$ and Ni-substituted $BaTiO_3$ (x = 0.175). In the PFM amplitude images, bright regions have larger amplitude values than dark regions. (b) The amplitude value distribution from PFM images for pure and Ni-substituted $BaTiO_3$ at x = 0.175.

In order to gain a deeper understanding of the dielectric phase transition, we conducted experiments of dielectric permittivity as a function of temperature in our Ni-substituted $BaTiO_3$ ceramics (shown in Figure 3.10). The results showed that there is a ferroelectric-to-paraelectric phase transition occurring at approximately 120 °C in pure $BaTiO_3$ (x = 0.00) (marked by the solid arrow) corresponding to a structural transition from tetragonal to cubic symmetry. As the Ni concentration increases (x = 0.01 and 0.02), the transition temperature moves towards room

temperature and ultimately disappears within the measured temperature range (i.e. from 22 to 350 °C) of our dielectric measurements at higher Ni concentrations (x = 0.03, 0.04, 0.05, and 0.08). Interestingly, in heavily Ni-substituted $BaTiO_3$ ceramic (x = 0.125), a dielectric transition appears at around 100 °C with remarkably huge dielectric constant (the maximum dielectric constant ~ 10,000 at 1 kHz). This enormous dielectric response in substituted $BaTiO_3$ ceramics has been observed previously in other studies [29-31].

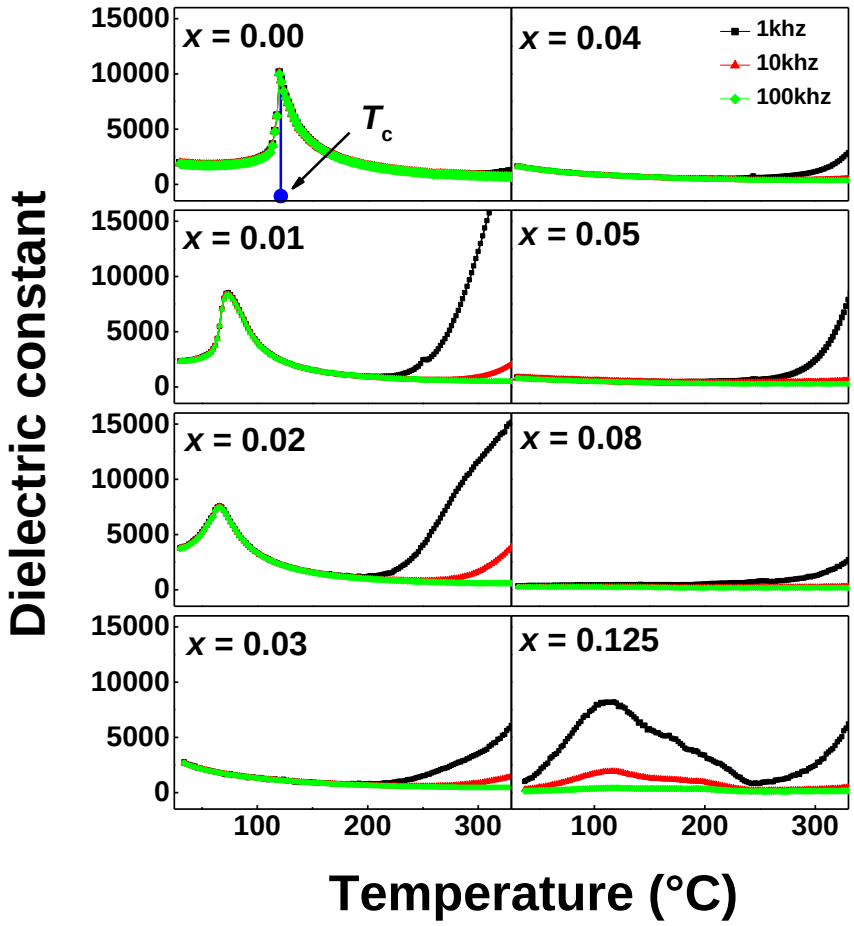

Figure 3.10 The dielectric permittivity as a function of temperature in the Ni-substituted $BaTiO_3$ ceramics at different frequencies (i.e., 1, 10, and 100 kHz). The solid arrow indicates the Curie temperature (T_c). As the Ni content increases, T_c moved toward the room temperature in the x

ranges between 0.01 and 0.02, and then disappeared in the measured temperature range for x values between 0.03 and 0.08. At x = 0.125, a huge dielectric anomaly occurred in a wide range of temperatures (from room temperature to 150 °C).

3.5. Possible origin of room-temperature phase transition by cation substitution

We conducted x-ray photoelectron spectroscopy (XPS) measurements to investigate the underlying mechanism behind the room-temperature polymorphic phase transition in $BaTiO_3$ induced by Ni substitution. Initially, we measured the XPS spectra at the Ni $2p_{3/2}$ edges to confirm the presence of Ni dopants in the substituted $BaTiO_3$ ceramics (Figure 3.11). We note that the intensity of a peak in XPS is directly proportional to the amount of a specific element [32]. We plotted the maximum intensity of the Ni $2p_{3/2}$ spectra as a function of the Ni contents (x). It is evident that the intensity of the XPS peak increases gradually with increasing x, indicative of a corresponding increase in the number of Ni atoms.

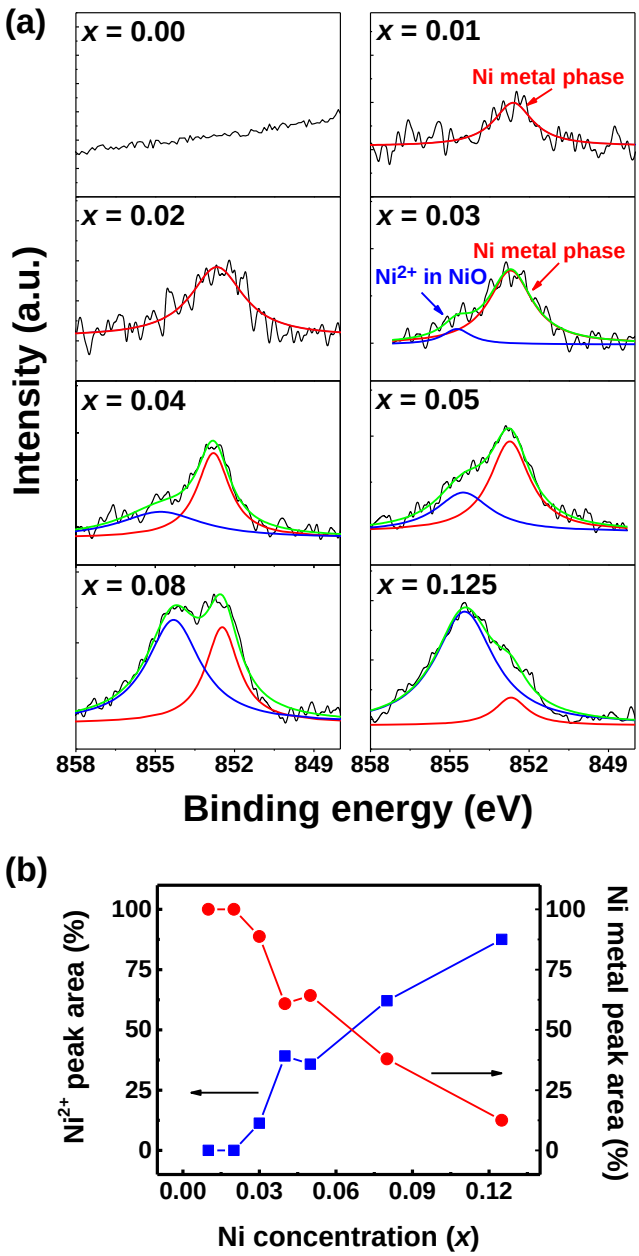

Figure 3.11 (a) The Ni $2p_{3/2}$-edge XPS spectra in the Ni-substituted $BaTiO_3$ ceramics at different Ni concentration (x). At $x < 0.03$, the raw XPS data (the black solid line) was fitted by the spectrum of Ni metal state (the solid red line). (b) The Ni^{2+} oxidation peak (the solid blue line) emerges at higher Ni level ($x > 0.03$) and the solid green line illustrates the fitted data. The volume fraction of Ni metal peak (red curve) and Ni^{2+} oxidation peak (blue curve) as a function of Ni level (x).

To investigate the changes in the charge valence state of Ni dopants as a function of *x*, we performed a deconvolution of the raw XPS data [the black solid line in Figure 3.11(a)] at the Ni $2p_{3/2}$ edge into two spectra representing the Ni metal [binding energy ~852.5 eV, the red solid curve in Figure 3.11(a)] and Ni^{2+} oxidation [binding energy ~854.5 eV, the blue solid curve in Figure 3.11(a)]. We then extracted the volume fraction from the best Lorentzian fits [the green solid curve in Figure 3.11(a)] of the individual XPS peaks and plotted it as a function of *x* [Figure 3.11(b)]. We found that at lower *x* values (< 0.03), the XPS curve is fitted by only a single spectrum of the Ni metal state. In contrast, at *x* values of 0.03, 0.04, and 0.05, the oxidized Ni^{2+} peak starts to appear in addition to the Ni metal state. As *x* increases, the peak area of the Ni^{2+} oxidation state progressively increases, so that in the substituted $BaTiO_3$ sample with a high Ni concentration ($x = 0.125$), the Ni^{2+} state occupies most of the XPS spectrum.

With the change in the Ni oxidation state, oxygen vacancies would be generated to balance the overall charge neutrality in Ni-substituted $BaTiO_3$ ceramics. We analyzed the correlation between the oxygen vacancy amount and the increasing Ni content (*x*) by fitting raw XPS spectra at the O 1*s* edge [Figure 3.12(a)]. We observed that as the Ni concentration increases and a divalent Ni^{2+} peak starts to appear in the Ni $2p_{3/2}$-edge XPS spectra at $x = 0.03$, the portion of the oxygen-vacancy peak in the best-fitted O 1*s*-edge XPS spectra steeply increases. This suggests that oxygen vacancies are formed to maintain the balance of the overall charge valence state in the Ni-substituted $BaTiO_3$ when Ni metal state is oxidized to the divalent Ni^{2+} state. However, when the Ni concentration increases ($x > 0.05$), the fitted area of the oxygen-vacancy XPS spectra does not continue to increase. The area of oxygen vacancy peak becomes saturated at a heavy Ni concentration ($x > 0.05$).

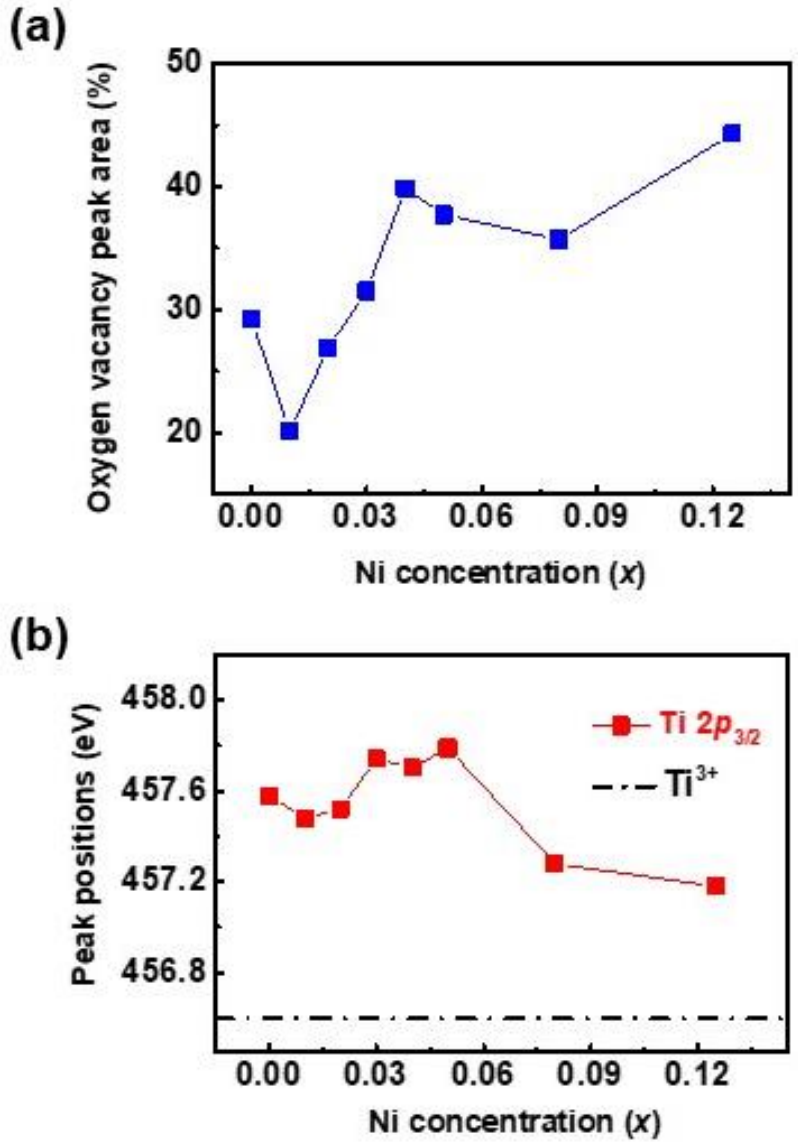

Figure 3.12 (a) The Ni concentration (x) dependence of oxygen-vacancy XPS peak area in Ni-substituted $BaTiO_3$ ceramics. (b) The variation of Ti $2p_{3/2}$ peak position depending on the Ni level (x) in the Ti $2p_{3/2}$-edge XPS spectra. The shift of the Ti $2p_{3/2}$ peaks towards a lower binding energy indicates the local modification of the Ti oxidation state from 4+ to 3+ (the black dash-dotted line shows the binding energy of Ti^{3+} state) at a defect site, which enables to compensate an unbalance in the charge valency by the oxygen vacancy generation.

The x-ray photoelectron spectroscopy (XPS) spectra at the Ti $2p_{3/2}$ edges indicate a reduction of the Ti^{4+} oxidation state with the generation of oxygen vacancies. Figure 3.12(b) shows the change in the binding energy of the tetravalent Ti^{4+} peak in the fitted XPS spectra at the Ti $2p_{3/2}$ edges as a function of the Ni concentration (x). It is clear that the binding energy of the Ti^{4+} state at a lower Ni content ($x > 0.05$) is higher (~ 457.6 eV) than that at higher x (< 0.03) (~ 457.2 eV). Note that the binding energy of the Ti^{3+} ions at the Ti $2p_{3/2}$ edge is reported around 456.6 eV [the black dash-dotted line in Figure 3.12(b)] [33, 34]. Therefore, the initial Ti^{4+} oxidation state in pure $BaTiO_3$ would change towards a lower state of $Ti^{(4-\delta)+}$ in Ni-substituted $BaTiO_3$ leading to a decrease in the binding energy. We also observe that the reduction in the binding energy of Ti^{4+} with increasing x is contrary to the increase of the oxygen vacancy peak area in the O 1*s* XPS spectra. Considering that the oxidation state of the transition-metal (e.g., Ni) atoms with a multi-valency is sensitive to the formation of oxygen vacancies in complex oxide ceramics [16, 21, 35], is highly likely that the decrease in the Ti^{4+} oxidation state is due to the oxygen vacancies in Ni-substituted $BaTiO_3$.

We now discuss the association between the modification of Ti charge valency induced by oxygen vacancies and the polymorphic phase transition from tetragonal to hexagonal structures in Ni-substituted $BaTiO_3$ ceramics. Our XRD results show that the hexagonal phase appears above the critical Ni level ($x = 0.03$), and it is important to note that the concentration of oxygen vacancies also increases at higher Ni concentration ($x > 0.03$). It is highly probable that an oxygen vacancy is generated when the Ni^{2+} ion substitutes for Ti^{4+} site in $BaTiO_3$ ceramics, resulting in a local change of the Ti charge valency from 4+ ($3d^0$) to 3+ ($3d^1$) [12]. Due to the local reduction of the Ti oxidation state by the formation of oxygen vacancy, the overall Ti oxidation state is reduced from 4+ to 4-δ, leading to the decrease of Ti^{4+} binding energy in the XPS spectra. When an oxygen

vacancy defect is present, a short-range Coulomb repulsion between neighboring B-site Ti ions is restored, leading to a degradation of the polar Ti-O ionic displacement in tetragonal $BaTiO_3$ [17, 19]. The hardening of the ferroelectric soft mode causes a transition from the ferroelectric tetragonal $BaTiO_3$ to paraelectric cubic $BaTiO_3$. In the generation of additional oxygen vacancies through Ni substitution for Ti cations, the hexagonal polymorph phase is realized at room temperature with a dielectric phase transition.

3.7. Future studies in a 6H-hexagonal $BaTiO_3$ system

The understanding of a structural phase transition in complex oxides is of interest in the aspect of fundamental science as well as technological application. The polymorphic phase transition in oxide materials is usually accompanied by the appearance of facilitating physical properties. Furthermore, by stabilizing an exotic polymorphic phase of oxides, attractive physical phenomena are expected to be realized.

In this work, the polymorphic phase transition in $BaTiO_3$ ceramics by Ni substitution is systematically investigated. The microscopic origin of structural phase transition is discussed in conjunction with the experimental analyses. A 6H-hexagonal phase in $BaTiO_3$, which is only stable above 1460 °C for the stoichiometric composition, is stabilized at room temperature by Ni substitution. Considering that the multiferroics have been realized in the hexagonal oxides, 6H-hexagonal $BaTiO_3$ can be an excellent platform for achieving new room-temperature multiferroics with high performance. Furthermore, the oxygen-deficient $BaTiO_3$ with a hexagonal symmetry would be a suitable system for examining the protonation effect on the dielectric properties of oxide materials.

References

1. M. Imada, A. Fujimori, Y. Tokura, *Rev. Mod. Phys.* **70**, 1039 (1998).
2. M. Acosta, N. Novak, V. Rojas, S. Patel, R. Vaish, J. Koruza, G. Rossetti Jr, J. Rödel, *Appl. Phys. Rev.* **4**, 041305 (2017).
3. B. Jaffe, W. Cook, H. Jaffe, *Piezoelectric Ceramics* (Academic Press, London, 1971).
4. K. W. Kirby, B. A. Wechsler, *J. Am. Chem. Soc.* **74**, 1841-1847 (1991).
5. G. M. Keith, K. Sarma, N. M. Alford, D. C. Sinclair, *J. Electroceramics* **13**, 305-309 (2004).
6. R. D. Burbank, H. T. Evans, *Acta Crystallogr.* **1**, 330-336 (1948).
7. D. P. Dutta, M. Roy, N. Maiti, A. K. Tyagi, *Phys. Chem. Chem. Phys.* **18**, 9758-9769 (2016).
8. N. Dang, T. Thanh, L. Hong, V. Lam, T.-L. Phan, *J. Appl. Phys.* **110**, 043914 (2011).
9. H. T. Langhammer, R. Bottcher, T. Muller, T. Walther, S. G. Ebbinghaus, *Phys. Condens. Matter.* **27**, 295901 (2015).
10. H. T. Langhammer, T. Müller, K. H. Felgner, H. P. Abicht, *J. Am. Ceram. Soc.* **83**, 605-611 (2000).
11. C. Fu, N. Chen, G. Du, *Ceram. Int.* **43**, 15927-15931 (2017).
12. D. I. Woodward, I. M. Reaney, G. Y. Yang, E. C. Dickey, C. A. Randall, *Appl. Phys. Lett.* **84**, 4650-4652 (2004).
13. O. Eibl, P. Pongratz, P. Skalicky, H. Schmelz, *Philos. Mag. A* **60**, 601-612 (1989).
14. R. Glaister, H. Kay, *Proc. Phys. Soc.* **76**, 763 (1960).
15. G. M. Keith, M. J. Rampling, K. Sarma, N. M. Alford, D. Sinclair, *J. Eur. Cream. Soc.* **24**, 1721-1724 (2004).

16. D. C. Sinclair, J. M. Skakle, F. D. Morrison, R. I. Smith, T. P. Beales, *J. Mater. Chem.* **9**, 1327-1331 (1999).

17. R. E. Cohen, *Nature* **358**, 136-138 (1992).

18. P. Hu, J. Chen, J. Deng, X. Xing, *J. Am. Ceram. Soc.* **132**, 1925-1928 (2010).

19. R. E. Cohen, H. Krakauer, *Ferroelectrics* **136**, 65-83 (1992).

20. S. Das, R. Mishra, B. Roul, *Solid. State. Commun.* **191**, 19-24 (2014).

21. A. Rečnik, D. Kolar, *J. Am. Ceram. Soc.* **79**, 1015-1018 (1996).

22. R. Rhodes, *Acta. Crystallogr.* **4**, 105-110 (1951).

23. F. Jona, G. Shirane, *Ferroelectric Crystals* (Pergamon Press, New York, 1962).

24. D. Yoon, *J. Ceram. Process. Res.* **7**, 343 (2006).

25. H. Han, C. Voisin, S. Guillemet-Fritsch, P. Dufour, C. Tenailleau, C. Turner, J. C. Nino, *J. Appl. Phys.* **113**, 024102 (2013).

26. H. M. Nguyen, N. V. Dang, P. Y. Chuang, T. D. Thanh, C. W. Hu, T. Y. Chen, V. D. Lam, C. H. Lee, L. V. Hong, *J. Appl. Phys.* **99**, 202501 (2011).

27. M. E. Lines, A. M. Glass, *Principles and applications of ferroelectrics and related materials* (Oxford university press, 2001).

28. J. Scott, *J. Phys. Condens. Matter* **20**, 021001 (2007).

29. W. Q. Cao, L. F. Xu, M. M. Ismail, L. L. Huang, *Mater. Sci-Poland.* **34**, 322-329 (2016).

30. Q. Sun, Q. Gu, K. Zhu, R. Jin, J. Liu, J. Wang, J. Qiu, *Sci Rep.* **7**, 42274 (2017).

31. S. Zheng, D. Shi, L. Liu, G. Li, Q. Wang, L. Fang, B. Elouadi, *J. Mater. Sci-Mater. El.* **25**, 4058-4065 (2014).

32. J. F. Watts, J. Wolstenholme, *An introduction to surface analysis by XPS and AES* (John Wiley & Sons, 2003).

33. D. Gonbeau, C. Guimon, G. P. Guillouzo, A. Levasseur, G. Meunier, R. Dormoy, *Surf. Sci.* **254**, 81-89 (1991).

34. M. Murata, K. Wakino, S. Ikeda, *J. Elec. Spec. Phenom.* **6**, 459-464 (1975).

35. X. Liu, S. Gao, H. Xu, Z. Lou, W. Wang, B. Huang, Y. Dai, *Nanoscale* **5**, 1870-1875 (2013).

Chapter 4

Hydrogenation control of dielectric permittivity in 6H-hexagonal $BaTiO_3$ ceramics

4.1 Dielectric materials with ultrahigh dielectric permittivity

Dielectric permittivity defines how strongly a dielectric material becomes electrically polarized under the influence of an electric field [1]. Nowadays, dielectric materials with high dielectric permittivity are still in demand for potential applications in a wide range of functional devices such as capacitors [2], dynamic random access memories [3], high-energy-density storage [4], and passive sensors [5, 6].

4.1.1. $CaCu_3Ti_4O_{12}$

The $CaCu_3Ti_4O_{12}$ system has attracted considerable attention in the research field because of its excellent dielectric properties (Figure 4.1). Recently, the colossal dielectric constant in related cubic perovskite $CaCu_3Ti_4O_{12}$ has been reported with a maximum permittivity of 10^4 over a wide temperature range of 100-600 K [7-9]. Note that the thermal stability of dielectric permittivity in $CaCu_3Ti_4O_{12}$ makes it suitable for use in actual device applications. Due to interests in aspects of fundamental science and practical applications, there are numerous studies on the ultrahigh dielectric permittivity in $CaCu_3Ti_4O_{12}$ compounds. Although various mechanisms have been suggested to explain the obtained giant dielectric responses [7, 10, 11], the microscopic origin of colossal dielectric permittivity in $CaCu_3Ti_4O_{12}$ remains unclear, rather under controversy.

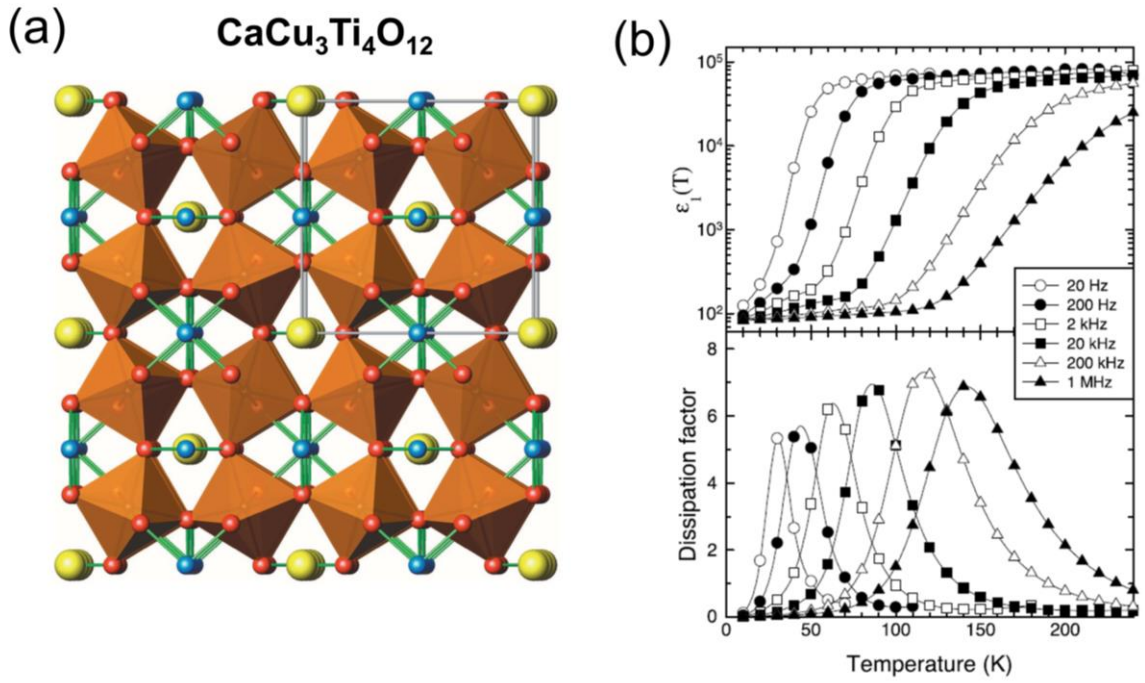

Figure 4.1 (a) The crystal structure of $CaCu_3Ti_4O_{12}$. The blue, red, and yellow balls represent the Cu, O, and Ca atoms, respectively. (b) The dielectric constant as a function of temperature in $CaCu_3Ti_4O_{12}$ [7].

4.1.2. Undoped/doped $BaTiO_3$

Ferroelectric materials, like $BaTiO_3$, are widely used due to their huge dielectric anomaly obtained at ferroelectric-paraelectric phase transition [12, 13]. The giant dielectric constant ~ 8000 has been obtained in polycrystalline $BaTiO_3$ ceramics. However, such high dielectric permittivity of a transition from ferroelectric to paraelectric is only obtained in a narrow temperature range close to the transition temperature (T_c), which restricts these materials to technological applications [14, 15]. Up to now, many efforts have been devoted to enhance the dielectric permittivity in $BaTiO_3$. For example, using a synthesis method of spark plasma sintering, the colossal dielectric constant up to 10^5 over a range of temperature from 100 to 300 K has been achieved in $BaTiO_3$

ceramics [Figure 4.2(a)] [16]. Furthermore, chemical doping is also a promising approach to improve the dielectric properties of $BaTiO_3$ [17, 18]. In La-doped $BaTiO_3$ ceramic, an ultrahigh dielectric constant of ~ 10^5 is achieved from 200 to 450 K, as shown in Figure 4.2(b).

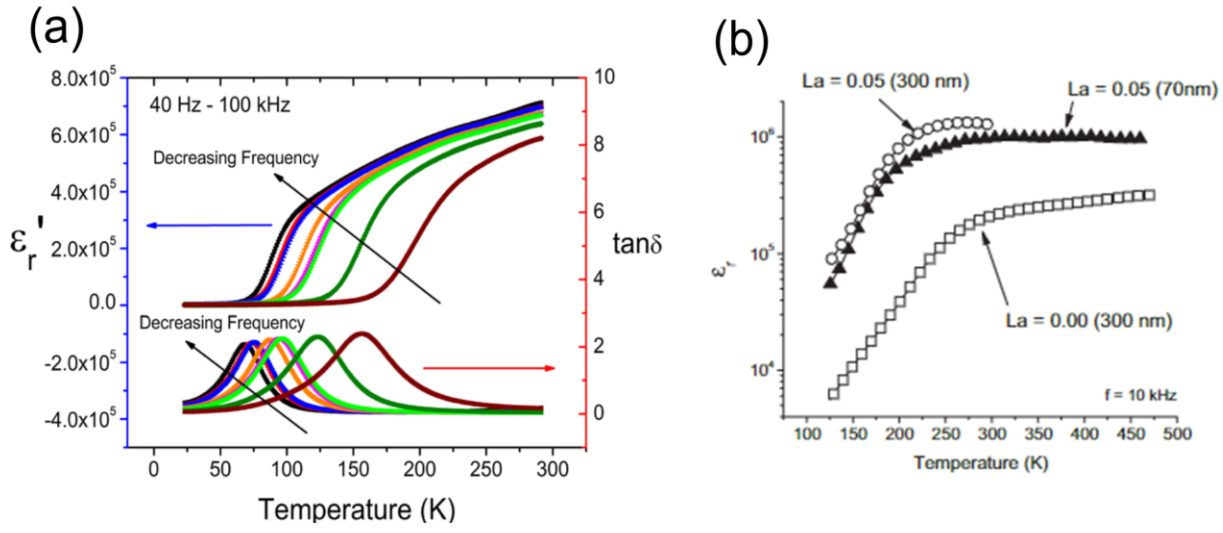

Figure 4.2 Colossal dielectric constant in (a) pure and (b) La-doped $BaTiO_3$ ceramics [16, 17].

4.1.3. TiO_2-based materials

TiO_2-based ceramics have been discovered as a new colossal dielectric permittivity material. In particular, by co-doping of the acceptor (In^{3+}) and donor (Nb^{5+}) into TiO_2, the (In, Nb) codoped-TiO_2 ceramics exhibit an ultrahigh dielectric constant ($\varepsilon \sim 10^4$) with a low dielectric loss ($\tan\delta \sim 0.05$) in a temperature range of 80-450 K [see Figure 4.3(a)] [19, 20]. The huge dielectric constant is also stable in the measured frequency region (10 to 10^5 Hz) [Figure 4.3(b)]. The reported studies also pointed out that the huge dielectric response in (In, Nb) codoped-TiO_2 is closely related to defect formation.

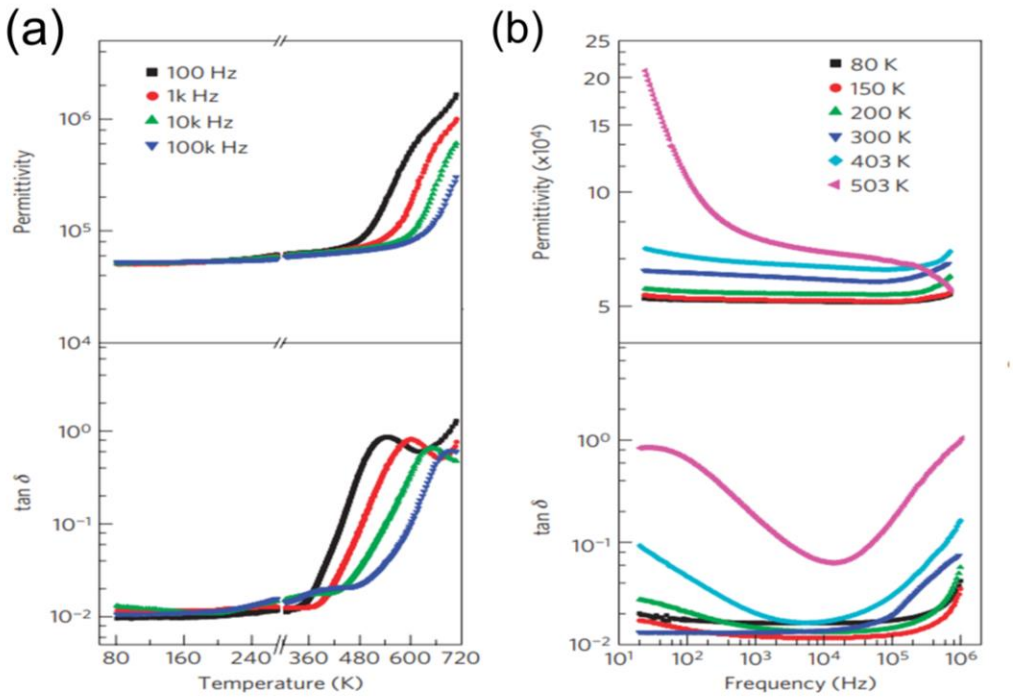

Figure 4.3 (a) The temperature-dependent dielectric constant and dielectric loss in (In, Nb) codoped-TiO_2. (b) dielectric permittivity and loss as a function of frequency in (In, Nb) codoped-TiO_2 ceramics [19].

4.1.4. Double perovskite oxides

Double perovskite oxide is a promising platform for achieving colossal dielectric permittivity. The high dielectric responses have been reported in various oxide ceramics with a double perovskite structure [21, 22]. For instance, it has been reported that the double perovskite Ba_2CoNbO_6 shows a dielectric constant of 10^3 within a temperature range of 80-300 K [Figure 4.4(a)] [21]. Furthermore, a giant dielectric permittivity up to 10^5 has been obtained in the La_2CuSnO_6 ceramics fabricated by a conventional solid-state reaction method [Figure 4.4(b)] [22]. These findings highlight the potential of the double perovskite oxide system in developing a new class of high-dielectric constant materials.

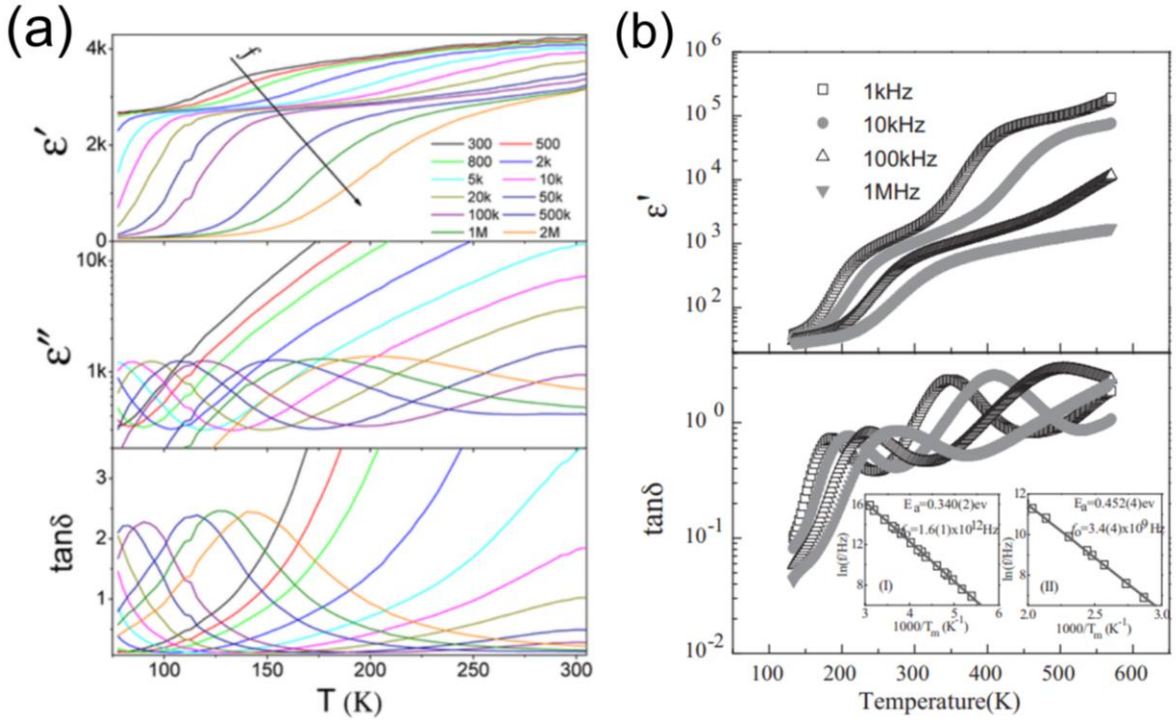

Figure 4.4 Ultrahigh dielectric permittivity in double perovskite oxides. The temperature-dependent dielectric constant and dielectric loss in double perovskite (a) Ba_2CoNbO_6 and (b) La_2CuSnO_6 ceramics [21, 22].

4.2. Engineering of physical properties in complex oxides by protonation

Protonation (i.e., the introduction of hydrogen ions to materials) is a promising route to control the physical properties of dielectric oxides. The hydrogen ions, the smallest and the lightest ions, would be incorporated into the oxide materials leading to the modification in the associated physical properties [23-25]. The previous works indicated that a variety of physical properties including crystal structures [23, 24], electronic structures [23, 24], electrical properties, magnetic properties, and transport characteristics [23, 25] have been reversibly manipulated through protonation/deprotonation processes.

4.2.1. Manipulation of crystal structure in $SrCoO_{2.5}$ by protonation

Hydrogenation can be an effective way to tailor the crystal structure of complex oxides. Considering that the hydrogen ion is the lightest ion with a small ionic radius, the protons can be incorporated into the complex oxides experimentally [23, 24]. The incorporated protons into oxide materials can induce changes in the local lattice structure, leading to the modification of crystal structure macroscopically. Moreover, the crystal structure can be restored to the initial structural phase by a dehydrogenation process (i.e., the removal of hydrogen ions from materials), enabling the reversible modulation of structural phases. For example, in strontium cobalt oxide thin films, it has been reported the reversible transformation between brownmillerite $SrCoO_{2.5}$ and protonated $HSrCoO_{2.5}$ phases via protonation (Figure 4.5) [26]. Interestingly, a structural transition from a brownmillerite $SrCoO_{2.5}$ phase to a perovskite $SrCoO_3$ phase is also controllable through the incorporation of oxygen ions, resulting in phase transformations among three different crystalline phases (Figure 4.5) [26].

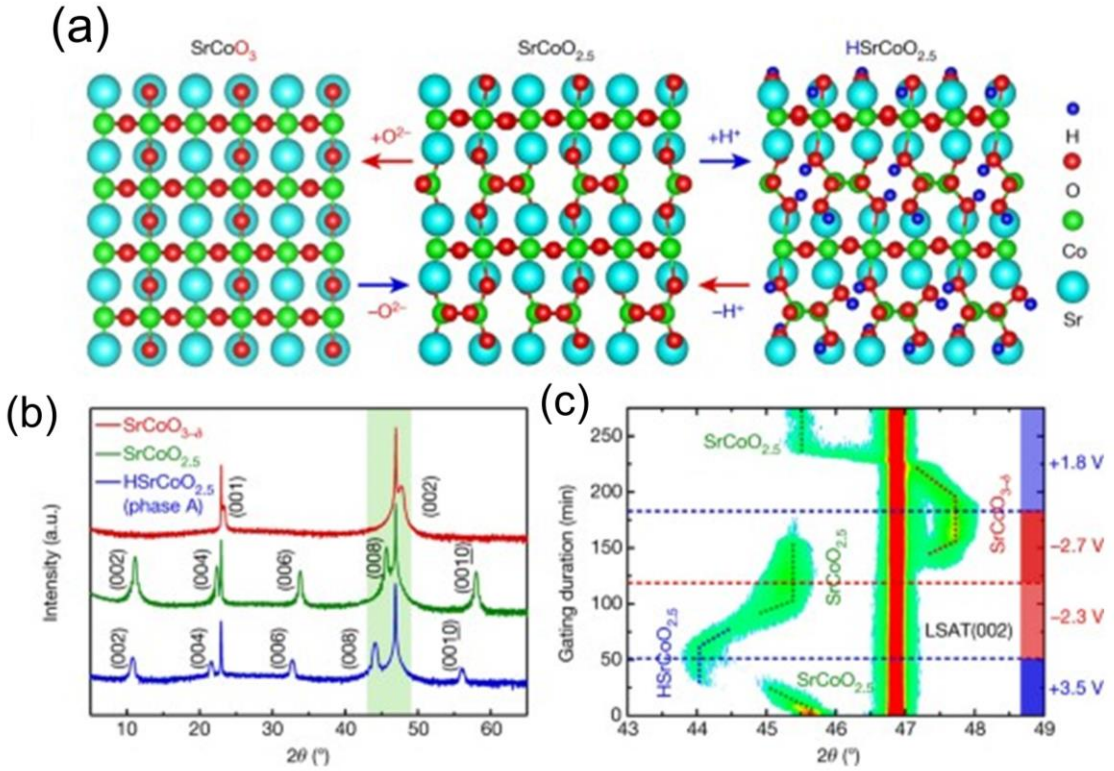

Figure 4.5 Reversible control of tri-state phase transformation among brownmillerite $SrCoO_{2.5}$, perovskite $SrCoO_3$ and protonated ($HSrCoO_{2.5}$) phases. The transition from brownmillerite $SrCoO_{2.5}$ to protonated $HSrCoO_{2.5}$ phases is reversibly controlled by protonation. While a transformation between brownmillerite to perovskite is obtained by oxygen ion insertion [26].

4.2.2. Hydrogen control of magnetic properties in (La, Sr)MnO_3

The hydrogen-driven magnetic properties have been reported in the $La_{0.67}$ $Sr_{0.33}MnO_3$ (LSMO) thin films [27]. The magnitude of magnetic moment in ferromagnetic LSMO films is controllable via hydrogenation/dehydrogenation processes (Figure 4.6). By incorporating hydrogen ions (H^+) in the LSMO film, the charge valence state of Mn ions is reduced locally. The local reduction of the Mn oxidation state by protonation suppresses the double exchange interaction, resulting in a decrease in saturation magnetization of ferromagnetic LSMO films [27].

This indicates the reversible manipulation of magnetic behaviors in LSMO films through hydrogenation.

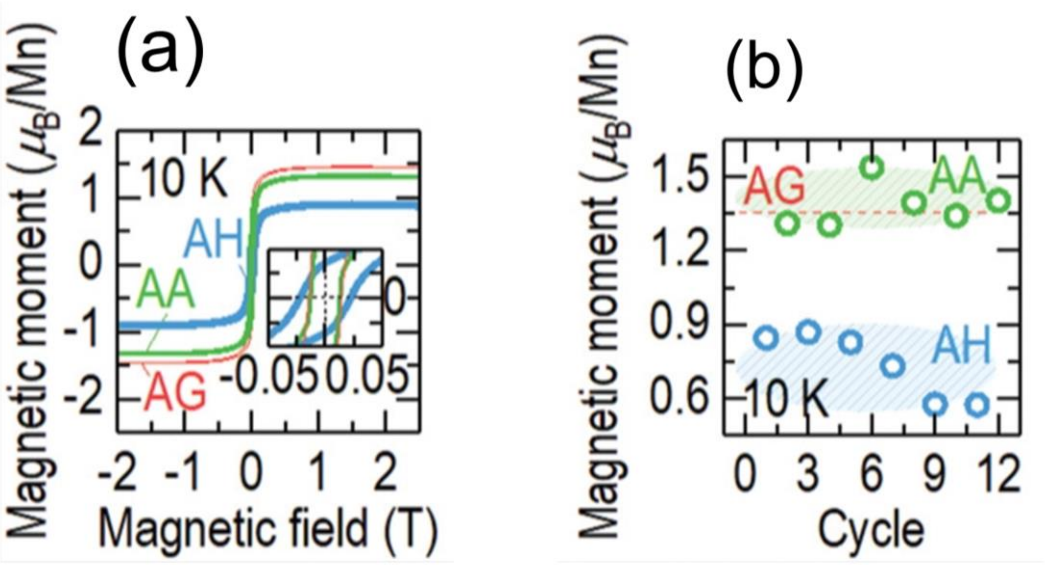

Figure 4.6 Reversible changes in magnetic properties $La_{0.67}Sr_{0.3}MnO_3$ (LSMO) films by hydrogenation (i.e. annealing in hydrogen) and dehydrogenation (i.e. annealing in argon). (a) The magnetic field dependence of the magnetic moment of as-grown (AG), hydrogen-annealed (AH), and argon-annealed (AA) films. (b) The reversible control of the saturation magnetic moment in ferromagnetic LSMO films [27].

4.2.3. Effect of hydrogenation on electrical properties in VO_2

The change of crystal structure and associated electrical properties by hydrogenation has been investigated in vanadium dioxide (VO_2) [23]. As shown in Figure 4.7, it is evident that the resistivity of VO_2 thin films is modulated through hydrogenation (i.e., annealing in a mixed gas of H_2 and Ar) and dehydrogenation (i.e., annealing in air) processes. Note that the ratio in resistance

between hydrogenated and dehydrogenated VO_2 films is up to 10^5 over the repetition of the thermal annealing in hydrogen gas and in air.

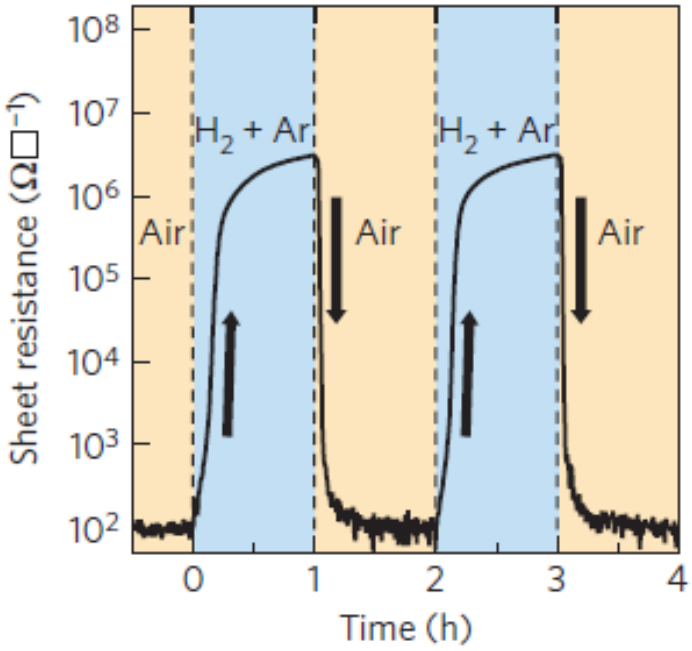

Figure 4.7 Hydrogenation-induced resistivity modulation of VO_2 thin films. The reversible resistivity changes through hydrogen/dehydrogenation [23].

4.3. Hydrogenation-induced colossal dielectric responses in oxygen-deficient oxide ceramics

Our question is how hydrogenation affects the dielectric properties of dielectric oxide ceramics. To answer this question, a systematically experimental approach is needed to figure out the hydrogenation effect on the dielectric properties of oxide ceramics. The dielectric permittivity of dielectric oxide ceramics could be modified by hydrogenation via water dissociation. Considering that the dissociation of water molecules is energetically feasible at oxygen vacancy defects in complex oxides [28, 29], hydrogen ions dissociated from water molecules would be introduced into the oxygen-deficient oxide materials. For the as-sintered state, the oxygen vacancy

defects in oxide ceramics are mostly accumulated in the proximity of grain boundaries [Figure 4.8(a)]. The as-sintered ceramics exhibit a low dielectric constant in the whole frequency range with small variations. When the oxygen-deficient oxide ceramics are exposed to air, the hydroxyl ions dissociated from the water are adsorbed on oxygen vacancies nearby the grain boundaries [Figure 4.8(b)]. On the other hand, dissociated protons (H^+) will be introduced into grains of ceramics [Figure 4.8(c)]. The introduction of protons with a positive charge inside ceramics modifies the overall dielectric responses in the Ni-substituted $BaTiO_3$ ceramics. After air exposure, the oxide ceramics show dielectric relaxation behaviors with the increasing frequency and an ultrahigh dielectric constant is achieved at a low frequency.

Here we used the 6H-hexagonal $BaTiO_3$ as a material system to check the effect of protonation on the dielectric properties of complex dielectric oxide ceramics [30]. In the pure $BaTiO_3$ composition, a hexagonal polymorph is only obtained at an extremely high temperature (> 1460 °C) [30, 31]. Very recently, it has been experimentally demonstrated the stabilization of the hexagonal $BaTiO_3$ phase at room temperature by transition-metal substitution [32-34]. Furthermore, the formation of oxygen vacancies by transition-metal substitution is closely related to the realization of 6H-hexagonal $BaTiO_3$ [33-35]. The oxygen-deficient $BaTiO_3$ ceramic with a 6H-hexagonal phase would be a suitable system to study the dielectric responses to the hydrogenation in complex oxides. The protonation to the oxygen-deficient $BaTiO_3$ ceramics can be obtained through a treatment under ambient environments. When the water molecules in the ambient environment contact with the ceramics, oxygen vacancy defects on the surface facilitate the dissociation of water molecules into protons (H^+) and hydroxyls (OH^-). The dissociated hydrogen ions can be introduced in the 6H-hexagonal $BaTiO_3$ ceramics, leading to the modification in dielectric properties [28, 29, 36]. Note that low frequency-dielectric responses are

very sensitive to the spatial distribution of mobile ionic charges (e.g., H^+ ions) [16, 37, 38], it is possible to tailor dielectric responses in oxygen-deficient $BaTiO_3$ ceramics by protonation.

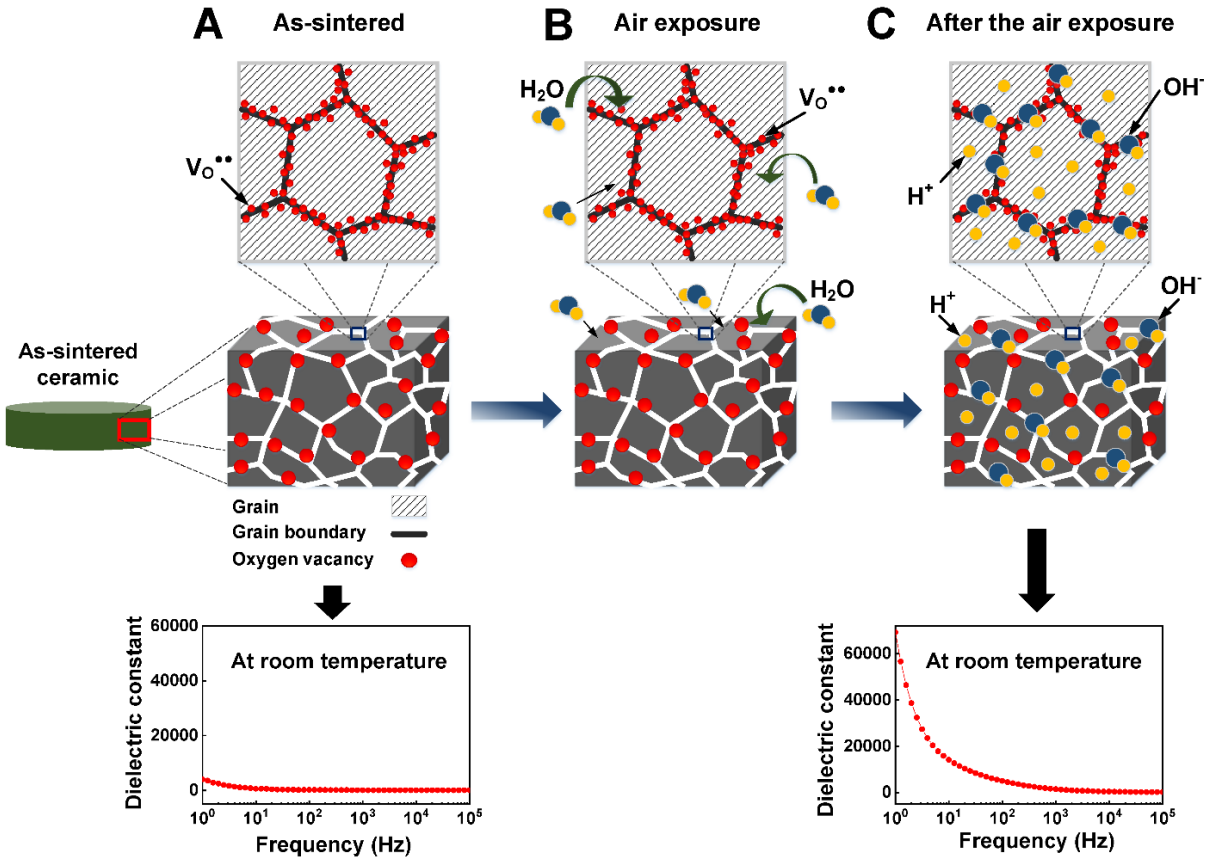

Figure 4.8 The schematic illustration of a change in dielectric responses of oxide ceramics induced by hydrogenation through water dissociation. (a) For the as-sintered state, oxygen vacancy defects are mostly accumulated at grain boundaries. (b) The oxide ceramics are exposed to the ambient air. (c) Hydroxyl ions dissociated water molecules are adsorbed at oxygen vacancy sites on the surface, while hydrogen ions are introduced to ceramics.

4.4. Experimental methods

In this research, we have developed an experimental strategy to examine the protonation effect on dielectric properties in oxide ceramic compounds via the specific treatment under

ambient environments. To do this, we synthesized the Ni-substituted $BaTiO_3$ ceramics [$Ba(Ti_{1-x}Ni_x)O_{3-\delta}$] at doping concentration ($x = 0.175$) with a 6H-hexagonal phase by a conventional solid-state reaction method (see Chapter 2). The pure $BaTiO_3$ ceramics were also fabricated for comparison. The obtained densities were ~ 5.91 and 4.74 g/cm^2 for pure and Ni-substituted ceramics, respectively. It followed that the Ni-substituted $BaTiO_3$ ceramics were less dense than the pure $BaTiO_3$ ceramics, probably due to oxygen vacancies by Ni substitution. In tetragonal $BaTiO_3$ ceramics, the density of porous ceramics (3.93 g/cm^2) was approximately 65% of the theoretical density (6.02 g/cm^2) for the tetragonal phase [40, 41]. The measured relative density of the Ni-substituted $BaTiO_3$ ceramics was ~82% of the theoretical density of the 6H-hexagonal $BaTiO_3$ phase [39], it was therefore plausible that the Ni-substituted $BaTiO_3$ ceramics were not porous.

We examined the change of dielectric responses in Ni-substituted $BaTiO_3$ ceramics to various ambient environments. We initially performed the dielectric measurements for as-sintered Ni-substituted $BaTiO_3$ ceramics. After a specific treatment under an ambient environment for a particular time duration, we re-measured dielectric responses in the treated Ni-substituted $BaTiO_3$ ceramics. The evolution of dielectric permittivity under different ambient conditions was monitored. To test the change of dielectric constant under the ambient environment, the samples were exposed to the air conditions and then, re-measured dielectric properties after a particular air-exposure time. For the treatment under vacuum, water vapor, N_2, and CO_2 conditions, the Ni-substituted $BaTiO_3$ ceramics were treated under the surrounding atmosphere in a desiccator for a particular time duration (for more details, see the method part in the Chapter 2).

4.5. Characterization of the Ni-substituted $BaTiO_3$ ceramics

4.5.1. Crystal and electronic structures

Figure 4.9(a) showed the x-ray diffraction (XRD) theta-2theta (θ-2θ) pattern of the as-sintered Ni-substituted $BaTiO_3$ [$Ba(Ti_{1-x}Ni_x)O_{3-\delta}$, x = 0.175]. The solid red lines corresponded to the measured XRD θ-2θ spectra, which were matched with the reference XRD pattern (marked by the blue bar). This suggested the formation of a hexagonal polymorphic phase in the $BaTiO_3$ ceramics by Ni substitution [33, 34]. According to our results in Chapter 3, it was evident that oxygen vacancies played a crucial role in stabilizing the phase at room temperature [30, 34]. We also performed the X-ray absorption spectroscopy (XAS) measurements of the as-sintered ceramic, as shown in Figure 4.9(b). In O *K*-edge spectra, peaks A and B were attributed to the transition from O 1*s* to t_{2g} and e_g hybridized states between O 2*p*-Ti 3*d*, respectively. It was observed that the absorption peak 'A' corresponding to a transition from O 1*s* to Ti 3*d* t_{2g} orbitals was suppressed in the Ni-substituted $BaTiO_3$ compared to pure $BaTiO_3$ ceramics. Note that the intensity of the absorption peak 'A' is sensitive to oxygen off-stoichiometry in complex oxides [42, 43]. Therefore, it is likely that the Ni-substituted $BaTiO_3$ ceramics incorporate a larger amount of oxygen vacancies than pure $BaTiO_3$ ceramics, which allows for the realization of the hexagonal phase in oxygen-deficient substituted $BaTiO_3$.

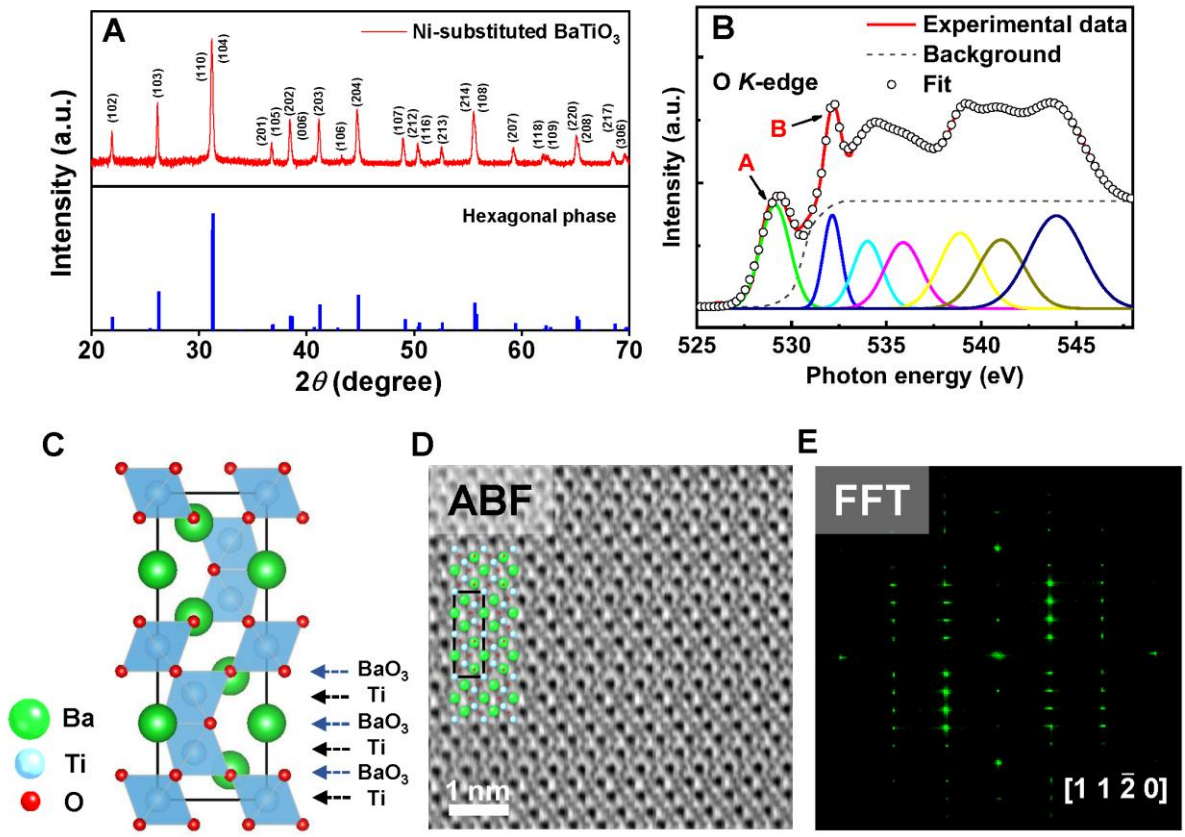

Figure 4.9 (a) XRD pattern of the as-sintered Ni-substituted $BaTiO_3$ ceramics. (b) The normalized O *K*-edge x-ray absorption spectra of the Ni-substituted $BaTiO_3$ ceramics. (c) Schematic diagram of the hexagonal $BaTiO_3$ structure viewed along the $[11\bar{2}0]$ direction. (d) ABF-STEM images of the as-sintered Ni-substituted $BaTiO_3$ ceramics along $[11\bar{2}0]$ zone axis. The project lattice structure of the hexagonal phase was superimposed in (a) and (b). The green, blue, and red balls represented the Ba, Ti, and O atoms, respectively. (e) The corresponding FFT pattern of the Ni-substituted $BaTiO_3$ ceramics along the $[11\bar{2}0]$ zone axis.

As shown in Figure 4.9(c), in the hexagonal $BaTiO_3$, the BaO_3 and Ti sub-layers are alternatively stacked in [0001] direction, and the stacking order of six BaO_3 sub-layers follows the hexagonal close-packing scheme of ABCACB in a single unit cell [30, 31, 44]. Here, two pairs of face-sharing TiO_6 oxygen octahedra are inter-connected through a corner-sharing TiO_6 octahedron

in a single unit cell [30-32]. The annular bright-field (ABF)- scanning transmission electron microscopy (STEM) analyses revealed that the observed atomic configuration is in good agreement with the projected lattice structure along the $[11\bar{2}0]$ zone axis [Figure 4.9(d)]. In a corresponding fast Fourier transform (FFT) pattern obtained from the STEM images, we also found that the diffraction spots are well matched with the simulated electron diffraction pattern of hexagonal symmetry (Figure 4.10).

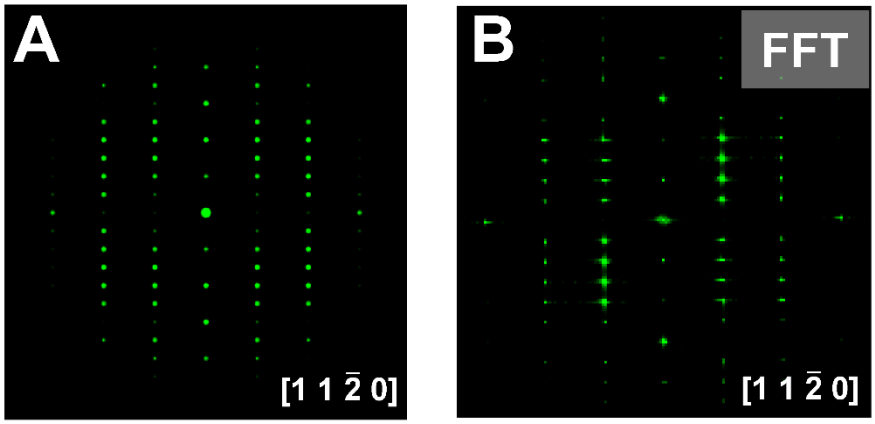

Figure 4.10 The fast Fourier transform (FFT) analyses of Ni-substituted $BaTiO_3$ ceramics. (a) The simulated electron diffraction pattern of the 6H-hexagonal $BaTiO_3$ polymorph along $[11\bar{2}0]$ direction. (b) The experimental FFT pattern of Ni-substituted $BaTiO_3$ ceramics.

4.5.2. Surface morphology and chemical composition analyses

To verify the chemical composition of the as-sintered Ni-substituted $BaTiO_3$ ceramics, we performed the field emission scanning electron microscope (FE-SEM) and energy-dispersive spectroscopy (EDS) analyses. Figure 4.11 showed the field emission-scanning electron microscope (FE-SEM) images and corresponding energy dispersive spectroscopy (EDS) results of the as-sintered Ni-substituted $BaTiO_3$ ceramics. We visualized the spatial distribution of each element

for grains [i.e., area indicated by red polygons in Figure 4.11(a) and (b)] and grain boundaries [i.e., red solid lines in Figure 4.11(a) and (b)]. The corresponding EDS mapping data at Ba *L*-, Ti *K*-, and Ni *K*-edges showed the uniform contribution of elements. In contrast, there was an inhomogeneous distribution of the oxygen element in O *K*-edge spectra. From local EDS measurements (Figure 4.12), the atomic percentages of the oxygen element were 74.8 and 50.2% at grains and grain boundaries in the as-sintered ceramics, respectively. This indicated that the grain boundary regions were significantly oxygen-deficient compared with the grain regions.

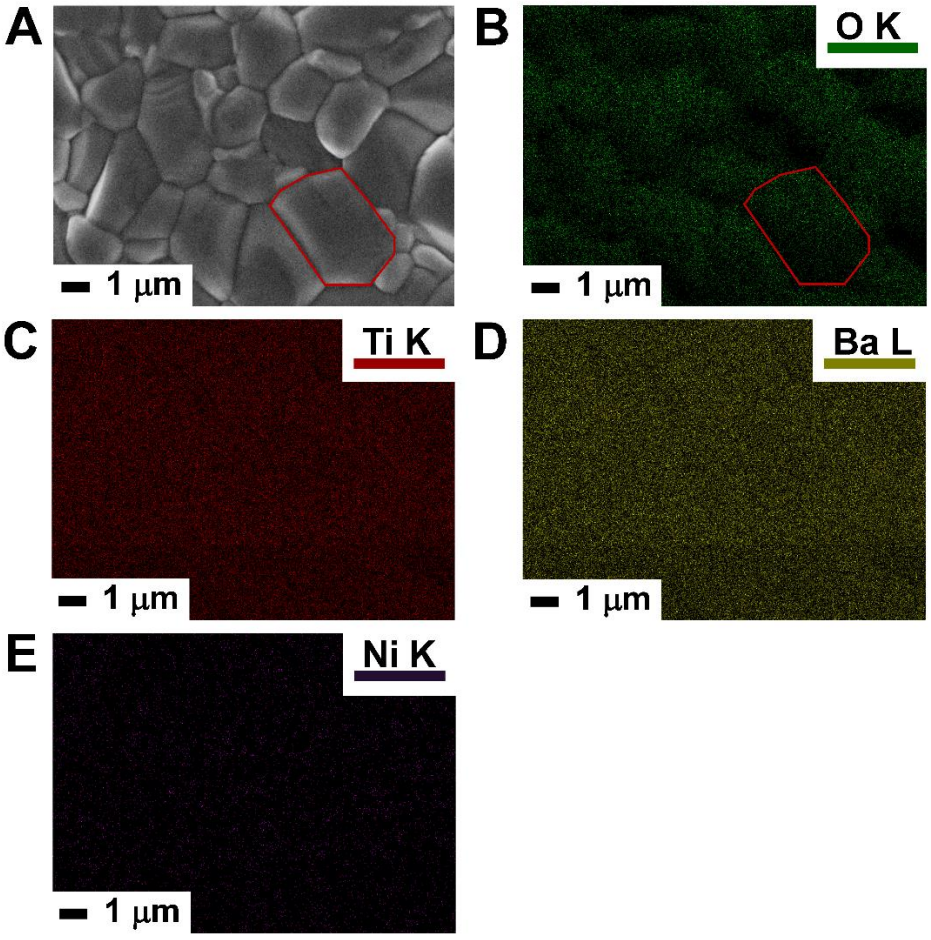

Figure 4.11 Surface morphology and elemental mapping analyses of the as-sintered Ni-substituted $BaTiO_3$ ceramics. (a) The field emission-scanning electron microscopy (FE-SEM) surface image of the as-sintered Ni-substituted $BaTiO_3$ ceramics. (b-e) The corresponding EDS mapping data of O, Ti, Ba, and Ni elements on the ceramic surface in (a), respectively. Area inside the red polygons in the FE-SEM image (a) and the O *K*-edge spectrum (b) represented grains.

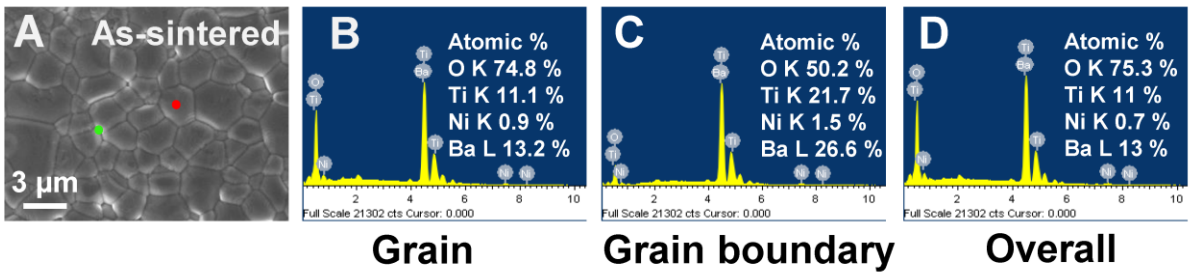

Figure 4.12 The EDS measurements of the as-sintered Ni-substituted $BaTiO_3$ ceramics in the grain and grain boundary regions. (a) The field emission-scanning electron microscopy (FE-SEM) image of the as-sintered Ni-substituted $BaTiO_3$ ceramics. (b-c) The local EDS spectra of (b) a grain [marked by the red spot in (a)] and (c) a grain boundary [marked by the green spot in (a)]. (d) The averaged EDS spectrum on the sample surface of (a).

4.6. Ultrahigh dielectric responses by a specific treatment under ambient environments

We systematically investigated the evolution of dielectric responses in Ni-substituted $BaTiO_3$ ceramics under different ambient environments. Firstly, we examined the change of dielectric permittivity under the ambient air condition (Figure 4.13). To investigate the dielectric properties of the Ni-substituted $BaTiO_3$ compounds, we performed a series of experiments. First, we measured the dielectric permittivity (ε) (marked by the red circle) and polarization-electric field (*P*-*E*) hysteretic characteristics (marked by the green circle) in the frequency range of 1 to 10^5 Hz

at room temperature. Next, we performed the temperature-dependent dielectric constant (marked by the blue circle) in the temperature range from 30 to 350 ˚C. To determine the effect of ambient air on the dielectric properties of the samples, we left the ceramic samples in air at room temperature for 6 weeks and then re-measured the dielectric responses using the same experimental method. In the as-sintered state, we observed a low dielectric constant of around 10^3 throughout the frequency range with slight variations [see Figure 4.13(b)]. The measured polarization in the Ni-substituted $BaTiO_3$ ceramics was linear with respect to the applied electric field, which is characteristic of dielectric materials with a small leakage current [Figure 4.13(c)]. We note that similar linear *P-E* curves were previously reported in substituted $BaTiO_3$ ceramics with 6H-hexagonal symmetry [33, 45]. there was no dielectric transition obtained in the plot of permittivity as a function of temperature in the range of 30 to 350 ˚C, as shown in Figure 4.13(d). Based on these results, we referred to the as-sintered state of our Ni-substituted $BaTiO_3$ ceramics as an 'off-state'.

The dielectric properties of Ni-substituted $BaTiO_3$ ceramics were significantly altered after exposure to air at room temperature for 6 weeks, as evidenced by the distinct changes observed in the treated ceramics. Figure 4.13(e) showed the dielectric relaxation behaviors of the treated ceramics with increasing frequency. The low-frequency dielectric constant at 1 Hz increased up to ~ 4.6×10^4 but decreased energetically with increasing frequency. The *P-E* hysteresis curve of the treated ceramics displayed an elliptical shape [Figure 4.13(f)], indicating that the Ni-substituted ceramics became electrically leaky after the air exposure [46]. Moreover, a huge dielectric transition was obtained in the temperature range of 30 to 190 ˚C [Figure 4.13(g)]. The dielectric anomaly was more prominent at lower frequencies, and the maximum dielectric constants at 1, 10, and 100 kHz were ~ 1.1×10^4, 5.1×10^3, and 1.0×10^3, respectively in the vicinity of the transition

temperature. This ultrahigh dielectric constant was similar to the results observed in various oxide ceramics exhibiting colossal dielectric permittivity in temperature-dependent dielectric dispersions [47, 48]. Interestingly, the frequency-dependent dielectric permittivity data of pure $BaTiO_3$ ceramics with tetragonal symmetry did not change after the 6-week air exposure. Therefore, we named the as-sintered state of the Ni-substituted $BaTiO_3$ ceramics as an 'off-state', and the treated state with high dielectric constant as an 'on-state'.

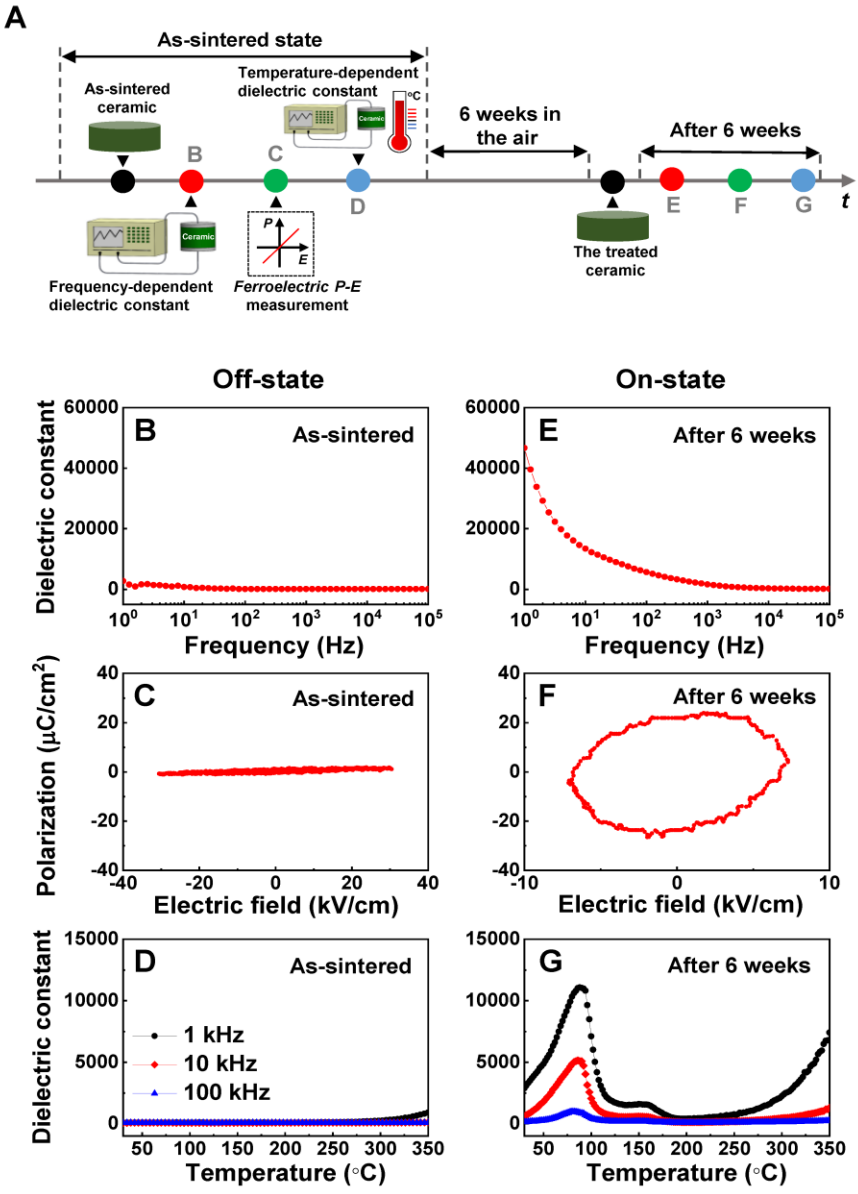

Figure 4.13 The change of dielectric responses in Ni-substituted $BaTiO_3$ ceramics under the ambient air environment. (a) A schematic diagram of the experimental sequence. Red, green, and blue circles represented frequency-dependent dielectric constant at room temperature, polarization-electric field hysteresis loop, and temperature-dependent dielectric constant measurements, respectively. (b) The frequency dependence of permittivity, (c) the *P-E* loop, and (d) the temperature-dependent dielectric constant in the as-sintered Ni-substituted $BaTiO_3$ ceramics. We exposed the as-sintered ceramics to the ambient air and then, re-measured the dielectric properties after a time duration of 6 weeks. (e) The frequency-dependent dielectric constant, (f) the hysteresis loop, and (g) the temperature dependence of dielectric permittivity in the treated ceramic samples.

To investigate the tunability of the two dielectric states observed in the as-sintered and treated Ni-substituted $BaTiO_3$ ceramics, we conducted thermal annealing on the treated ceramics. The treated Ni-substituted samples were subjected to heat treatment in a muffle furnace at 350 ˚C for 1 hour under ambient air, as illustrated in Figure 4.14(a). Next, we measured the frequency-dependent dielectric constant (indicated by the red circle), the polarization-electric field (*P-E*) hysteresis (indicated by the green circle), and the temperature-dependent permittivity (indicated by the blue circle) of the annealed sample. The ultrahigh dielectric permittivity (i.e., the on-state) observed in the low-frequency region of the treated ceramics disappeared completely in the annealed ceramics [Figure 4.14(b)]. Additionally, the *P-E* curve became linear with little hysteresis [Figure 4.14(c)]. The temperature-dependent dielectric dispersions of the annealed ceramic sample also revealed that the dielectric anomalies observed in the treated ceramic sample were suppressed, with no distinct transition in the temperature range of 30-190 ˚C [Figure 4.14(d)]. This suggested that the on-state with the ultrahigh dielectric permittivity at low frequencies was recovered to the

original state in our Ni-substituted $BaTiO_3$ ceramics through a thermally-assisted reset process. Therefore, our results indicate that the two different dielectric states observed in the Ni-substituted $BaTiO_3$ ceramics can be manipulated by external thermal stimuli.

In order to determine the extent to which the off and on states in Ni-substituted $BaTiO_3$ ceramics can be adjusted, we re-treated the annealed ceramic samples to ambient air at room temperature for a period of six weeks, followed by retesting all of the dielectric properties of the re-treated ceramic samples [indicated by the red, green, and blue circles in Figure 4.14(a)]. It was observed that the suppressed dielectric responses in the low-frequency region, representing the off-state, were restored in the re-treated ceramics, resulting in a very high dielectric permittivity ($\varepsilon \sim 6.9\times10^4$ at 1 Hz) in the frequency-dependent dielectric constant data [Figure 4.14(e)]. Additionally, the *P*-*E* loop [Figure 4.14(f)] and temperature-dependent dielectric characteristics [Figure 4.14(g)] in the off-state returned to typical behaviors of the on-state. The frequency-dependent dielectric responses were systematically monitored as a function of the duration time for the as-sintered and annealed states, and the reversible changes in low-frequency dielectric permittivity were clearly demonstrated. Thus, it was possible to reversibly control the off- and on-states in the dielectric responses of Ni-substituted $BaTiO_3$ ceramics through specific treatments under chemical environments (such as exposure to ambient air) and external stimulation (such as the application of heat and electric fields).

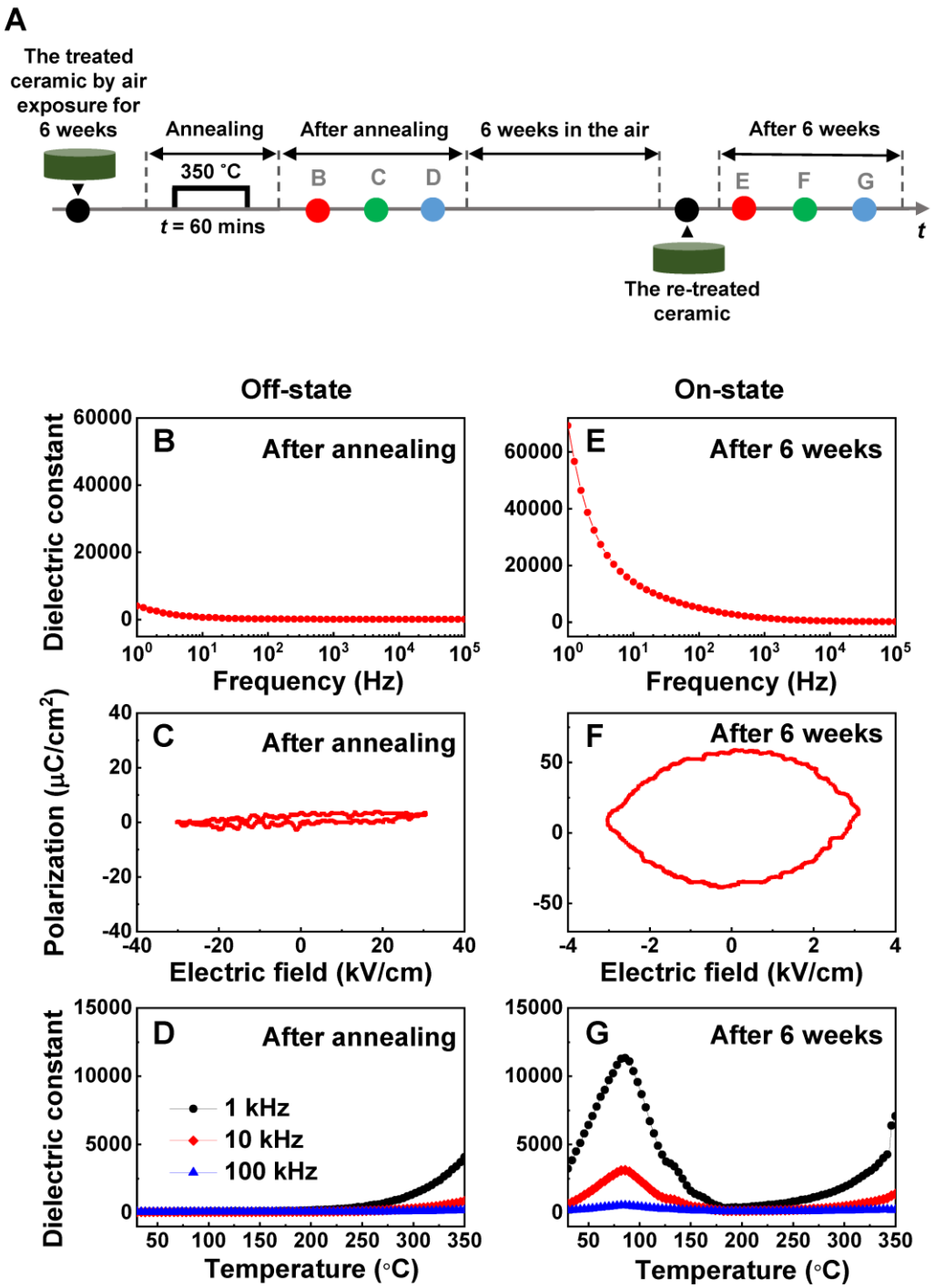

Figure 4.14 The reversible change of the dielectric responses in $BaTiO_3$ ceramics through thermal annealing and air exposure. (a) A schematic figure of the experimental sequence. The treated Ni-substituted $BaTiO_3$ ceramics by air exposure were annealed at 350 ºC for 1 hour. (b) The

frequency-dependent dielectric constant in treated ceramics after thermal annealing. (c) The hysteresis loop of annealed ceramic samples. (d) The temperature dependence of dielectric constant of the annealed Ni-substituted $BaTiO_3$ ceramics. The annealed ceramics were treated via air exposure for 6 weeks. (e) The frequency-dependent dielectric constant, (f) the *P*-*E* hysteresis loop, and (g) the temperature-dependent dielectric behavior in re-treated ceramics by ambient air environment.

In order to investigate how the dielectric responses of Ni-substituted $BaTiO_3$ ceramics change in response to ambient environments, we conducted a series of experiments (for more detailed information, refer to the method section in Chapter 2). We measured the dielectric constant as a function of frequency [Figure 4.15(a)] and loss [Figure 4.15(b)] before (indicated by black solid squares) and after (indicated by red solid circles) exposing the as-sintered ceramics to various atmosphere treatments (i.e., air, vacuum, N_2, CO_2, and high humidity) for a specific duration of time. To ensure experimental accuracy, we evacuated a desiccator to a base pressure of ~380 Torr before all ambient treatments (refer to the method section in Chapter 2). With the exception of high humidity, the treatment of as-sintered Ni-substituted $BaTiO_3$ ceramics in air, vacuum, N_2, and CO_2 environments for one week did not significantly alter the frequency-dependent dielectric constant. The dielectric permittivity remained consistently low at approximately 10^3 across the entire frequency range, while a slight change in the frequency-dependent dielectric loss was observed after the ambient treatments. This suggested that the initial off-state in the as-sintered Ni-substituted $BaTiO_3$ ceramics was not significantly impacted by exposure to air, vacuum, N_2, and CO_2. It was also possible that the ceramic samples exposed to these ambient conditions remained in the off-state, with no change in dielectric permittivity.

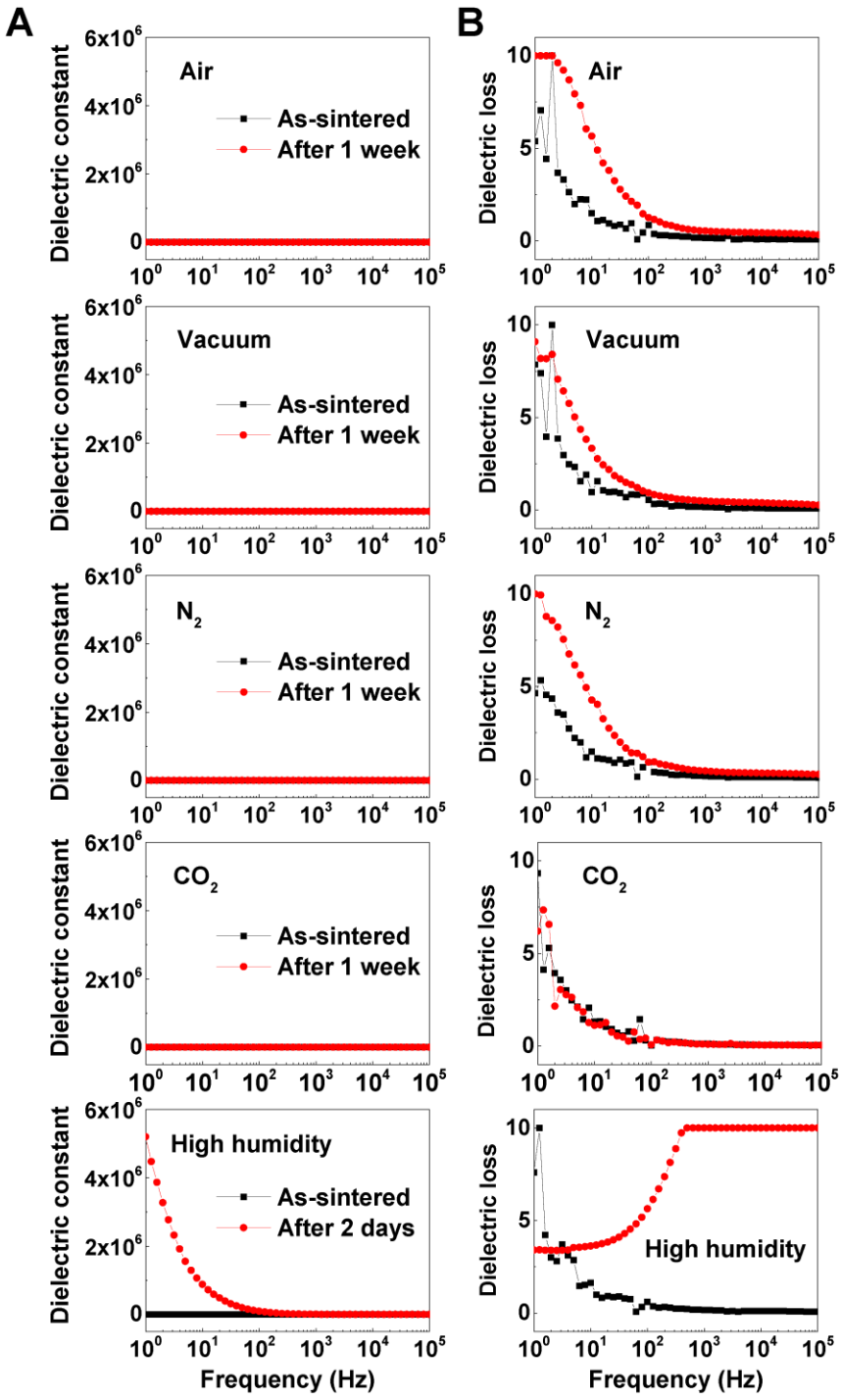

Figure 4.15 The evolution of dielectric responses in Ni-substituted $BaTiO_3$ ceramics under various ambient environments. (a) Change of frequency-dependent dielectric constant in Ni-substituted

$BaTiO_3$ ceramics under air, vacuum, nitrogen (N_2), carbon dioxide (CO_2), and high humidity environments. (b) Corresponding dielectric loss in ceramics before and after chemical treatments.

The effect of air exposure on the dielectric permittivity of Ni-substituted $BaTiO_3$ ceramics was found to be related to the presence of water molecules in the air. When the as-sintered Ni-substituted $BaTiO_3$ ceramic samples were exposed to a highly humid environment for two days, a significant change in their dielectric response was observed (as shown in the bottom panels of Figure 4.15). The Ni-substituted $BaTiO_3$ ceramics, which were treated under an environment containing a high level of moisture, exhibited a dielectric constant of around 5.2×10^6 (the on-state) at 1 Hz. It should be noted that the obtained high permittivity in treat ceramics was three orders of magnitude higher than the as-sintered ceramics (the off-state), as seen in Figure 4.15(a). This colossal dielectric permittivity value was comparable to values reported elsewhere (see Table 4.1). Moreover, the corresponding dielectric loss increased significantly up to the measurement limit ($\tan\delta \sim 10$) after the high-humidity treatment, as depicted in Figure 4.10(c). It was noteworthy that the duration of the humid ambient treatment (2 days) was even shorter than that of other treatments (1 week)

Table 4.1 The dielectric constant in the treated Ni-substituted $BaTiO_3$ ceramics under a humid condition and the colossal dielectric permittivity previously reported in various oxides ceramics.

Composition	Dielectric constant (ε)			Temperature	References
	At 1 Hz	At 10 Hz	At 100 Hz		
$Ba(Ti_{0.825}Ni_{0.175})O_{3-\delta}$	5.2×10^6	8.8×10^5	9.4×10^4	Room temperature	Current work
Previous works					
$CaCu_3Ti_4O_{12}$	1.0×10^6	5.0×10^5	3.0×10^5	308 K	[49]

$(In_{0.5}Nb_{0.5})_{0.01}Ti_{0.99}O_2$	1.0×10^7	1.0×10^6	2.0×10^5	Room temperature	[50]
$(Al_{0.5}Nb_{0.5})_{0.3}Ti_{0.7}O_2$	1.4×10^5	1.2×10^5	1.0×10^5	Room temperature	[51]

4.7. Possible mechanism: Protonation-driven ultrahigh dielectric constant in oxide ceramics

We now discuss *dc* and *ac* resistivity of Ni-substituted $BaTiO_3$ ceramics for the as-sintered and treated states. The *dc* resistivity was calculated as follows:

$$\rho_{dc} = R\frac{A}{d} \tag{1}$$

where *R*, *A*, and *d* represented the electrical resistance, surface area, and thickness of ceramic pellets, respectively. The *dc* resistivity was estimated to ~8.6×10^9 ohms·m at a zero relative humidity condition (RH = 0%), whereas it was ~4.1×10^7 ohms·m at a high relative humidity condition (RH = 80%). On the other hand, we also extracted the *ac* resistivity (ρ_{ac}) from the measured dielectric constant (ε) and dielectric loss ($\tan\delta$) using the following relation:

$$\rho_{ac} = \frac{1}{2\pi f \varepsilon_0 \varepsilon \tan\delta} \tag{2}$$

where ε_0 was the permittivity of free space and *f* is the frequency of the applied voltage bias. At a frequency of 1 Hz, the *ac* resistivities were ~2.1×10^6 and 1.1×10^3 ohms·m for the as-sintered ceramic (i.e., off-state) and the treated ceramic by humidity (i.e., on-state), respectively (the bottom panels in Figure 4.15). Note that the *ac* resistivity ratio (~1.9×10^3) between off- and on states was approximately an order of magnitude higher than the *dc* resistivity ratio (i.e., the proportion of the *dc* resistivity in a zero RH condition to that in a high RH condition ~2.1×10^2). It

was highly likely that such a difference between the *ac* and *dc* resistivity ratio would be attributed to an interfacial effect between the Ag electrode and the ceramic sample (*20*). A further study would be highly desirable to elucidate the relationship between the *ac* and *dc* resistivities of the Ni-substituted $BaTiO_3$ ceramics.

To gain a better understanding of the emergence of two different dielectric states (off- and on-states) in Ni-substituted $BaTiO_3$ ceramics with 6H-hexagonal symmetry, we conducted impedance measurements on both the as-sintered (off-state) and treated (on-state attained after a treatment under the ambient air for 6 weeks) Ni-substituted $BaTiO_3$ ceramics. we noted that polycrystalline Ni-substituted $BaTiO_3$ ceramics with 6H-hexagonal symmetry consisted of numerous grains and grain boundaries, as shown in Figure 4.16(a). To distinguish between the capacitive and resistive contributions of the incorporated grains and grain boundaries, we employed a simple brick-layer model in which a polycrystalline ceramic was conceptually made up of identical cubic bricks (i.e., grains) separated by flat layers (i.e., grain boundaries), as depicted by the hatched squares and red solid lines in Figure 4.16(b) [52, 53]. When we applied an external electric field [black solid arrow in Figure 4.16(b)] to the ceramics, two conducting channels were possible in the brick-layer model: (1) electrical currents [blue dashed arrow in Figure 4.16(b)] passing through only the horizontal grain boundaries and (2) electrical currents [blue dash-dotted arrow in Figure 4.16(b)] flowing alternatively through the grains and vertical grain boundaries. The equivalent electrical circuits for these two current paths were also displayed in Figure 4.16(c).

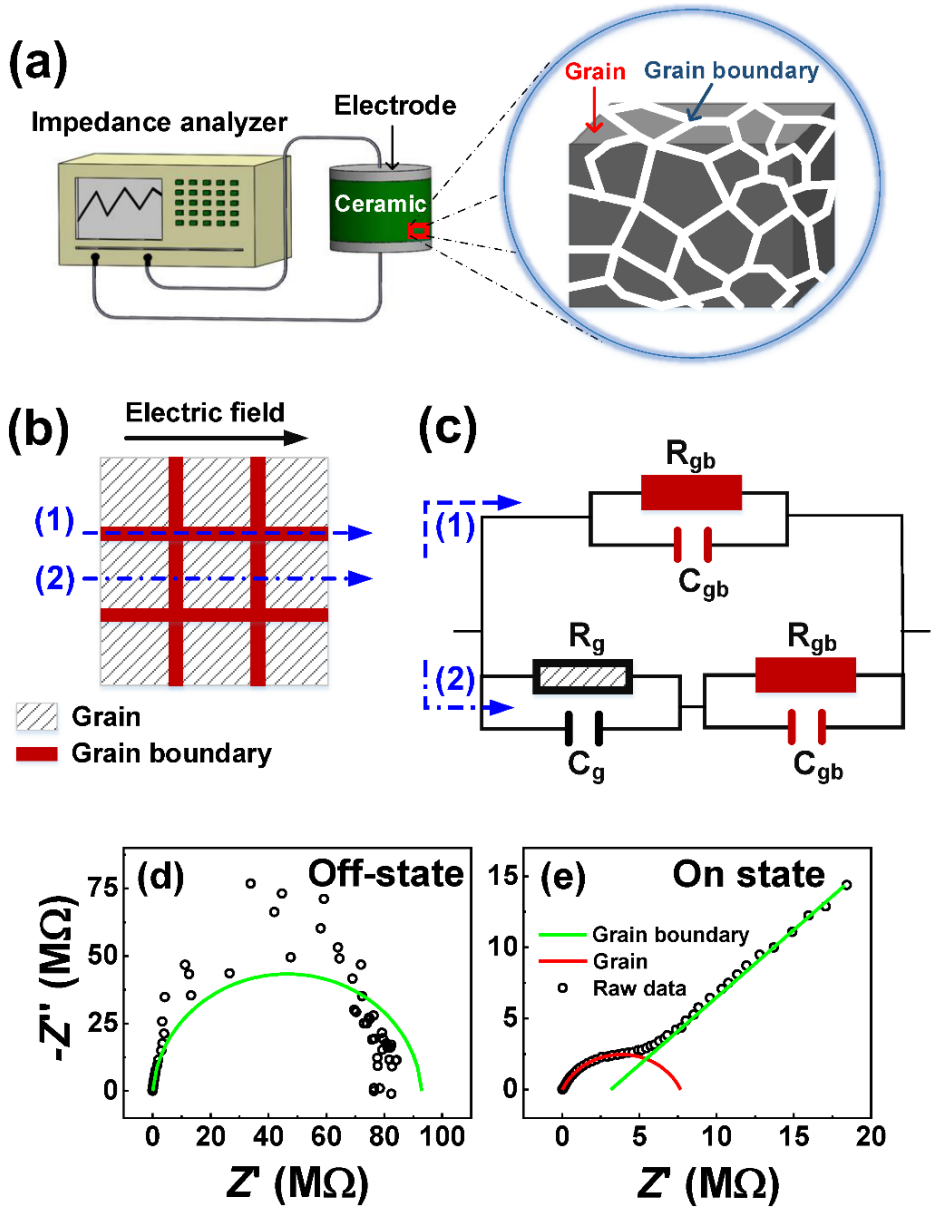

Figure 4.16 Impedance analyses of Ni-substituted $BaTiO_3$ ceramics at two dielectric states (i.e., off- and on-states). (a) Experimental set-up of impedance analysis. b) Schematic diagram of a brick-layer model for a polycrystalline ceramic. (c) The equivalent electric circuit. (d-e) The impedance complex plane plots in the Ni-substituted $BaTiO_3$ ceramic with off- (d) and on-state (e) at room temperature.

According to the impedance data, our observations revealed two distinct impedance responses to external electric fields in the off-state (i.e., as-sintered state) and on-state (i.e., treated state) in Ni-substituted $BaTiO_3$ ceramics with 6H-hexagonal symmetry. Figure 4.16(d) and (e) demonstrated the impedance data for the as-sintered (off-state) and treated (on-state) ceramics, respectively. The as-sintered ceramics showed a single semicircular arc (the green solid curve), while the treated ceramics exhibited a deconvoluted curve with two semicircles (the red and green solid curves) of different sizes. These impedance characteristics were also evident in temperature-dependent Cole-Cole data. We note that a semicircle obtained in the impedance spectra is attributed to a connection of a capacitor and a resistor in parallel [54, 55]. In the as-sintered state, most electrical currents passed through grain boundaries (the first case of the brick-layer model), resulting in a single semicircular arc in the Cole-Cole plots. In contrast, electrical currents passing through both grains and grain boundaries produced a double semicircular curve in the treated ceramics (the second case of the brick-layer model), indicating a modification of the electrical pathway. This change occurred when the as-sintered Ni-substituted $BaTiO_3$ ceramics were exposed to ambient air for 6 weeks.

We carried out the impedance measurements to ceramics with the on- and off-states for different temperatures (varying from 20 to 180 ˚C). We also deconvoluted our impedance data to the semicircular arcs. Note that each semicircular arc in impedance spectra represented a dielectric relaxation characteristic arising from a parallel electrical circuit between one capacitor and one resistor. As shown in Figure 4.17, the observed impedance spectra at various temperatures for the off-state were almost fitted for a single semicircular arc. It was plausible that the majority of electrical currents passed through the grain boundaries in the off-state where the accumulated oxygen vacancies at grain boundaries acted as a conducting channel. In contrast, the impedance

responses of the on-state showed that electrical currents went through both grains and grain boundaries resulting in the double-semicircular curve (Figure 4.18).

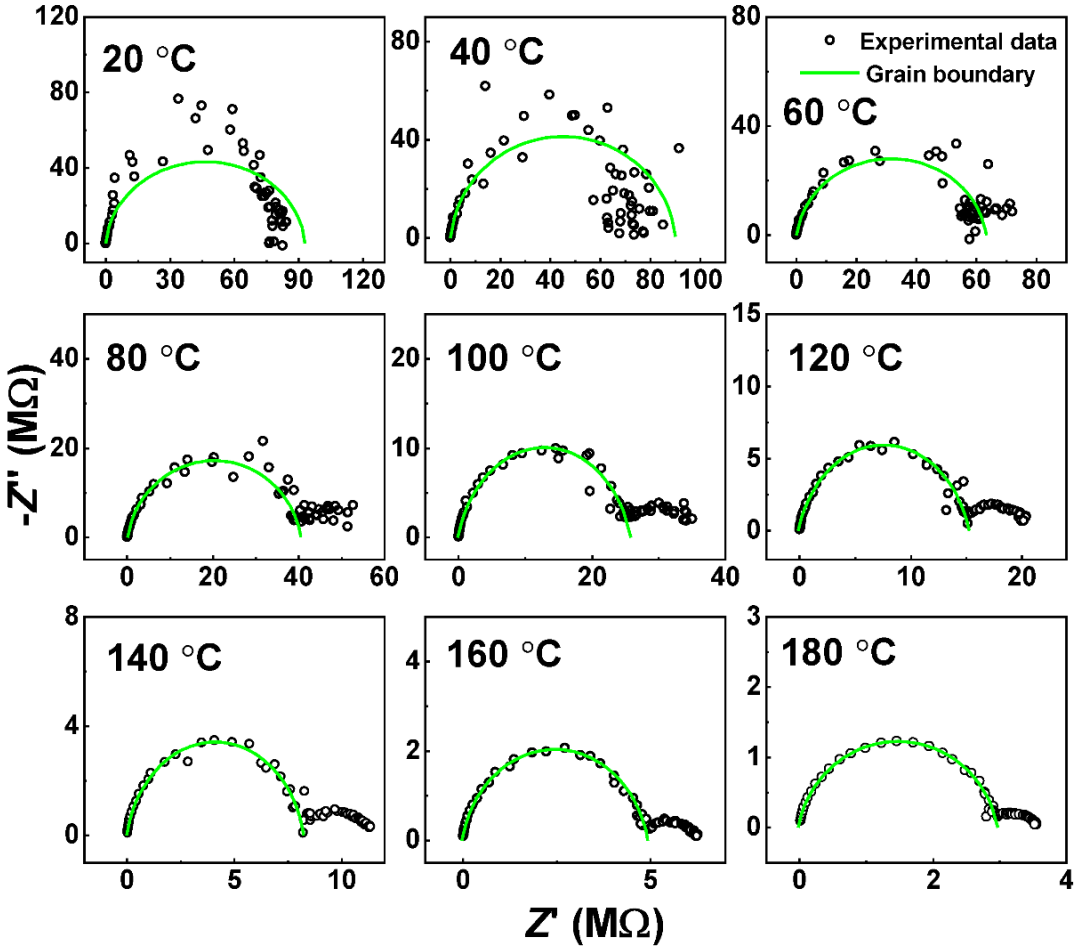

Figure 4.17 The impedance Cole-Cole plots in Ni-substituted $BaTiO_3$ ceramics at various temperatures for the off-state.

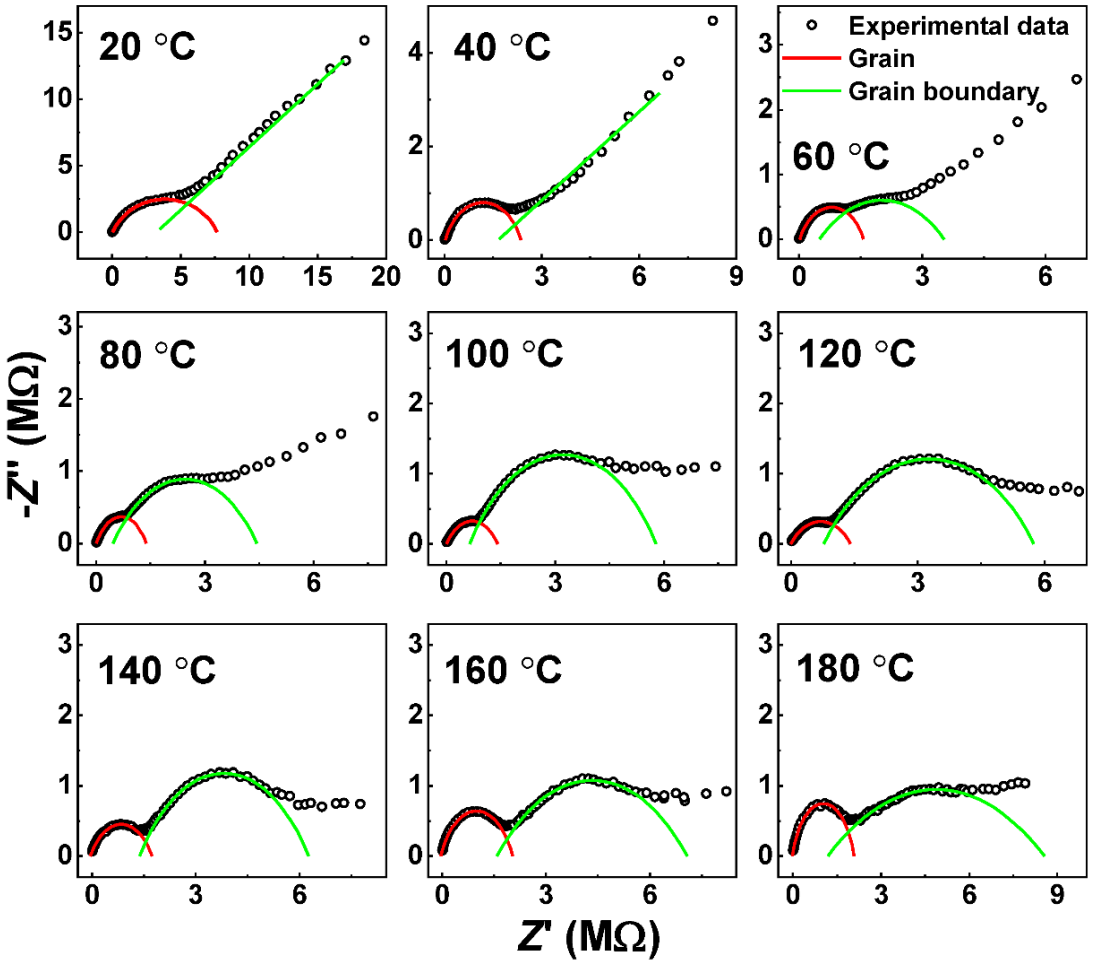

Figure 4.18 The impedance Cole-Cole plots in Ni-substituted $BaTiO_3$ ceramics at various temperatures for the on-state.

In order to clarify the microscopic origin of a difference in the dielectric responses between the off- and on-states of Ni-substituted $BaTiO_3$ ceramics, we conducted element-specific X-ray photoelectron spectroscopy (XPS) experiments on both the as-sintered and treated ceramics as shown in Figure 4.19(a) and (b), respectively. It was evident that the XPS spectra of Ba 3*d*, Ti 2*p*, and Ni 2*p* edges were similar. The difference was observed in XPS spectra in the O 1*s* orbital. We also deconvoluted the raw O 1*s* XPS data into three different spectra using Gaussian-Lorentzian fitting [42, 56], which were determined to be lattice oxygens (the red solid curve), oxygen

vacancies (the blue solid curve), and chemisorbed oxygen ions (the black solid curve), respectively [42, 57]. The XPS peak attributed to chemisorbed oxygen species, such as hydroxyls (OH-), was much stronger in the treated ceramics after exposure to ambient air for four weeks, compared to the as-sintered ceramics. while other XPS peaks of lattice oxygens and oxygen vacancies were almost identical after a treatment. We also noted that water molecules were involved in the difference in dielectric responses between the off and on states of the ceramics, suggesting that water vapor in the air was dissociated to form a proton (H^+) and a hydroxyl (OH^-) ion. And then the hydroxyl ions dissociated from water were adsorbed onto the ceramic surface.

To experimentally demonstrate the existence of hydrogen ions in our Ni-substituted $BaTiO_3$ ceramics, we performed the time-of-flight secondary ion mass spectrometry (TOF-SIMS) measurements in pure and substituted $BaTiO_3$ ceramics to visualize the spatial distribution of hydrogen (H^+) ions in samples. Before the TOF-SIMS analyses, the pure and Ni-substituted $BaTiO_3$ ceramics at the as-sintered state were treated under the ambient environment for 6 weeks. As shown in Figure 4.19(c), in pure $BaTiO_3$ ceramics, the intense signals of H^+ ions were observed at the top surface of the sample. This indicated that the water molecules were mostly adsorbed on ceramic surfaces after the treatment. In contrast to the pure samples, it was evident that the protons were identified not only on surfaces but also inside the Ni-substituted $BaTiO_3$ ceramics [Figure 4.19(d)]. In conjunction with XPS data, it was highly likely that hydroxyl (OH^-) ions dissociated water molecules in air were adsorbed at oxygen vacancy sites on the surface of our Ni-substituted $BaTiO_3$ with noticeable oxygen off-stoichiometry. Considering the fact that the protons with high mobility were easily incorporated in the complex oxides [36], the hydrogen ions dissociated from water molecules would be introduced inside the treated Ni-substituted $BaTiO_3$ ceramics, resulting in the modification of low-frequency dielectric permittivity.

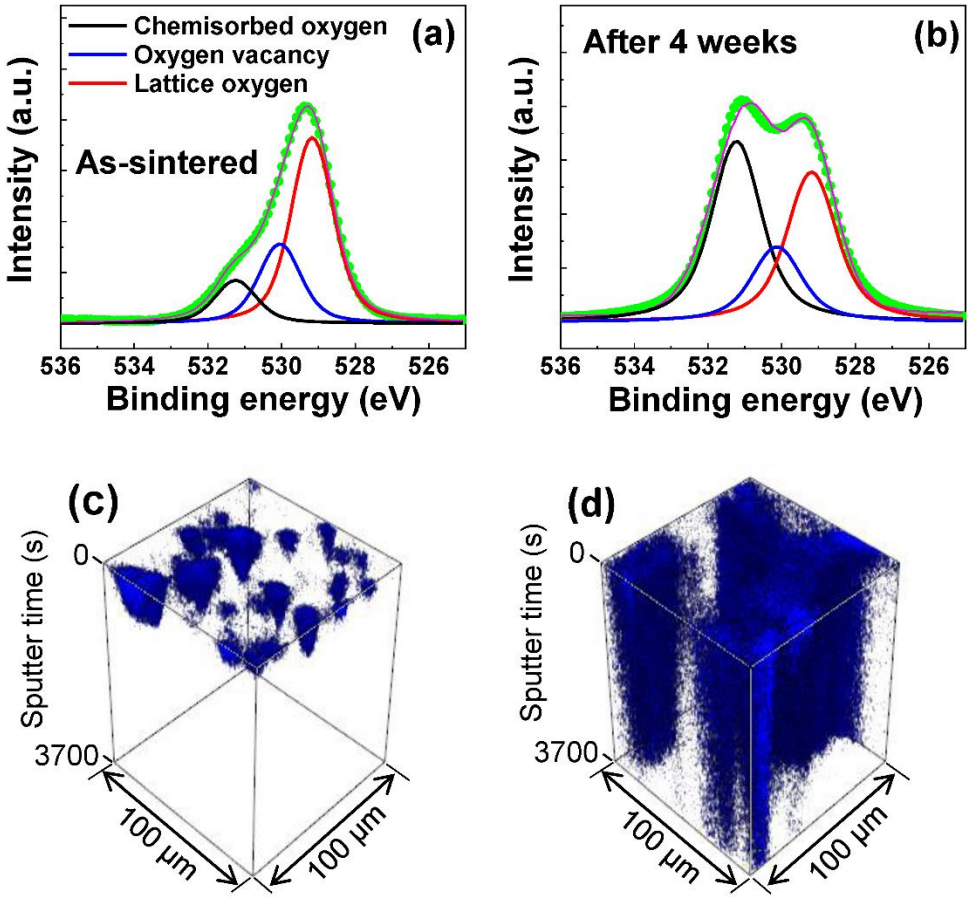

Figure 4.19 (a, b) XPS spectra at O 1*s* edge of the Ni-substituted $BaTiO_3$ ceramics at as-sintered state (a) and after 4 weeks in ambient air (b). The red, blue, and black solid lines in (a) and (b) represent the fitted curves of the oxygen in a lattice, the oxygen vacancy, and the chemisorbed oxygen in the surface of the ceramic. The volume fraction of the chemisorbed oxygen peak increases after air exposure. (c, d) TOF-SIMS 3D rendering maps of H^+ signals in the pure (c) and Ni-substituted $BaTiO_3$ (d) ceramics which were treated by air exposure for 6 weeks (scale: 100 μm × 100 μm, sputter time: 0 ~ 3700 seconds).

The observation of two dielectric behaviors in the low frequency region would originated from the introduction of hydrogen ions to Ni-substituted $BaTiO_3$ ceramics through the water

dissociation. Two dielectric states (i.e., on- and off-states) were reversibly controllable via a treatment under a specific ambient environment and a reset process by external stimulation. Based on EDS data, grain boundaries became more oxygen-deficient than grains for the as-sintered state (i.e., the off-state with a low dielectric permittivity at low frequencies) (Figure 4.11). The results indicated that the proportion of oxygen ions in grain boundaries was considerably lower (around 25%) compared to that in the grains (as depicted in Figure 4.12). It suggests that the majority of oxygen vacancies in the initially as-sintered Ni-substituted $BaTiO_3$ ceramics would accumulate at the grain boundaries [58]. In the off-state (i.e., as-sintered state), the grain boundaries with a large number of oxygen vacancies acted as the electrical conducting paths, while the grains with a low oxygen vacancy content would be were highly resistive. This difference in electrical conductivity between the grain boundaries and the grains facilitated the flow of electrical current mostly through the grain boundaries, which was consistent with the impedance results of the off-state (as illustrated in Figure 4.16). When the Ni-substituted $BaTiO_3$ ceramics were treated under the ambient air, it was plausible that polar hydroxyl (OH^-) ions that dissociated from water molecules were adsorbed at oxygen vacancy sites near the grain boundaries (as depicted in Figure 4.8). At the same time, it was highly likely that protons (H^+) that separated from water molecules could move within the grains (Figure 4.8). The presence of protons made the grains more electrically conductive in the treated Ni-substituted $BaTiO_3$ ceramics, enabling the electrical current to flow through both the grains and grain boundaries. Consequently, double-semicircular curves corresponding to grain and grain boundary distributions were obtained in the dielectric relaxation behaviors of the on-state (Figure 4.16). Moreover, the treated Ni-substituted $BaTiO_3$ ceramics became electrically leaky by the introduction of hydrogen ions into grains, resulting in an elliptical hysteresis curve [as depicted in Figure 4.13(f) and 4.14(f)] and an increase in dielectric loss [as

illustrated in Figure 4.15(b)] [59]. In order to maintain charge neutrality, the introduced hydrogen ions (H^+) could be removed from treated ceramics with the desorption of hydroxyl ions (OH^-) by applying the thermal stress (i.e., a reset process from the on-state to the initial off-state).

It is significant to discuss possible mechanisms of ultrahigh dielectric permittivity in the ambient-environment-treated substituted $BaTiO_3$ ceramics. Based on previous literature, it was reported that dielectric anomalies obtained in complex oxide ceramics would be attributed to a transition to a relaxor ferroelectric phase [60]. We identified the crystal structure of the as-sintered (off-state) and the treated (on-state attained by a treatment under a humid environment) Ni-substituted $BaTiO_3$ ceramics using X-ray diffraction (XRD) analyses. To examine the dielectric properties, we first deposited the Pt electrodes on the top and bottom sides of as-sintered ceramic pellets. Then, the XRD and frequency-dependent dielectric permittivity measurements were performed in as-sintered ceramics, respectively (Figure 4.20). Next, the as-sintered ceramics were treated under a humidity condition for 2 days. After the high-humidity treatment, we repeated the measurements of XRD and frequency-dependent dielectric constant in treated ceramics (Figure 4.20). The diffraction patterns of the off-state (i.e., the as-sintered ceramics) and on-state (i.e., the treated ceramics) were consistent with the reference XRD pattern of a hexagonal structure. The 6H-hexagonal polymorph was attained in both ceramics with off- and on-states, which indicated that the change of dielectric response in the Ni-substituted $BaTiO_3$ ceramics would not originate from a structural phase transition.

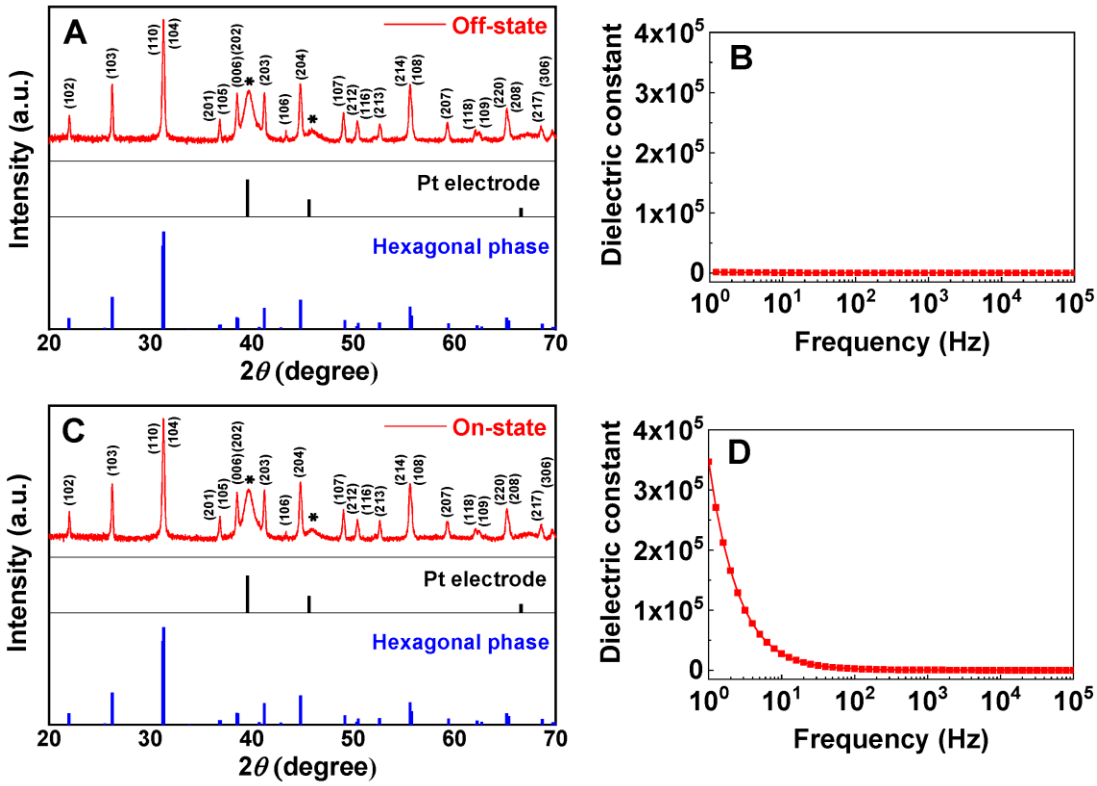

Figure 4.20 X-ray diffraction (XRD) measurements for two different dielectric states. The XRD patterns of Ni-substituted $BaTiO_3$ ceramics for (a) the off- and (c) on-states. The corresponding frequency-dependent dielectric constants of (b) the off- and (d) on-states.

4.7.1. Structural inhomogeneity induced by hydrogenation and the subsequent dielectric proximity effect

Hydrogenation induced an inhomogeneity in the structural and dielectric properties in Ni-substituted $BaTiO_3$ ceramics with 6H-hexagonal symmetry, which could be closely linked to the achieved colossal dielectric permittivity. In Ni-substituted $BaTiO_3$ ceramics with off-state (i.e., as-sintered state), the structural phases within the grains were expected to be homogeneous with minimal change in local dielectric permittivity, as most oxygen vacancies accumulated near the grain boundaries regions [as depicted in Figure 4.21(a)]. On the other hand, in the on-state, a large

number of hydrogen ions dissociated from water molecules could be introduced into the grains, resulting in heterogeneous distributions of the crystal structures and the electric polarizability on a microscopic level [as shown in Figure 4.21(b)]. Note that the proton is an ion with a positive charge. At a lattice site incorporating a proton (H^+), the local crystal structure at the atomic level would be more deformed accompanied by an enhancement in electric polarizability (an increase in dielectric constant) by an internal field generated by the introduced proton [28, 61]. It is worth noting that highly polarizable nano-domains with large dielectric constants could considerably enhance the electric polarizability of neighboring nano-domains with small dielectric constants through a proximity effect [62, 63]. Therefore, the inhomogeneity in the local dielectric responses caused by hydrogenation could lead to considerable improvement in the dielectric permittivity (i.e., electrical polarizability) in Ni-substituted $BaTiO_3$.

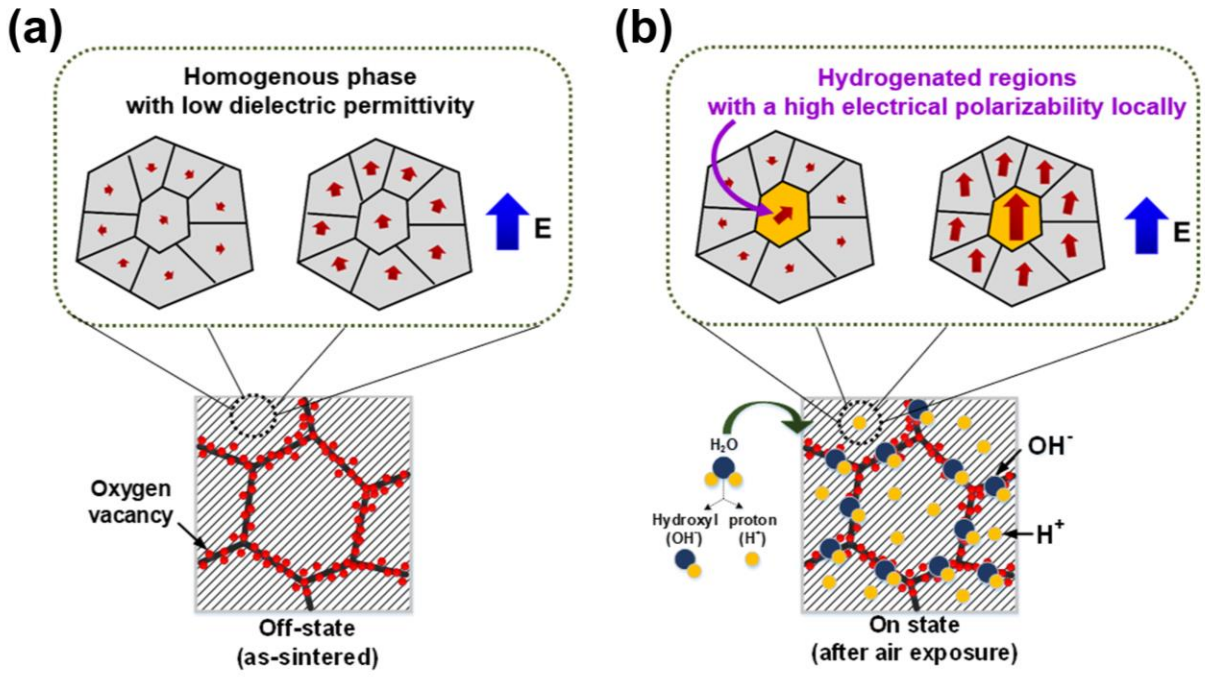

Figure 4.21 A possible mechanism of ultrahigh dielectric permittivity in Ni-substituted $BaTiO_3$ ceramics induced by hydrogenation.

4.7.2. Formation of interfacial dielectric layers between electrodes and ceramics

Herein, we discussed another possibility mechanism of colossal dielectric permittivity in Ni-substituted $BaTiO_3$ ceramics by hydrogenation. It should be noted that a capacitor configuration (i.e., Ag electrode/ Ni-substituted $BaTiO_3$ ceramic/ Ag electrode) was used to measure dielectric properties. At the interface between the silver electrode and a ceramic sample, a dielectric (depletion) layer would be formed [see Figure 4.22(a)]. The interfacial layer between a ceramic and an electrode is dielectric with a huge dielectric permittivity and a low conductivity, which acts as a high capacitance in parallel with a large resistor, connected in series to the bulk sample [as shown in Figure 4.22(b)] [64]. Therefore, the measured capacitance is attributed to the interfacial dielectric layer rather than the bulk response. As a result, the interfacial dielectric layers contributed to the overall measured capacitance resulting in the increase in the overall dielectric permittivity of Ni-substituted $BaTiO_3$ capacitors, especially at a low frequency region.

Then we can assume that the capacitance of the dielectric layer (C_i) is much higher than bulk capacitance (C_b) (the interface is much thinner than the bulk) and that the resistance of the dielectric layer (R_i) is also much higher than the resistance of bulk (R_b) [65]. When evaluating dielectric measurements, the dielectric constant usually is calculated from the measured capacitance data by:

$$\varepsilon = \frac{C}{C_0} = \frac{Ct}{\varepsilon_0 A} \quad (1)$$

Where C is the measured value of capacitance. C_0 is the geometrical capacitance, for a parallel-plate capacitor given by $C_0 = \varepsilon_0 A/t$ with A the area and t the plate distance of the capacitor. At low frequencies, in the interface dominated regime, the geometry of a capacitor is only the interfacial dielectric layer rather than the whole bulk geometry. Therefore, the calculation of C_0 determined from the bulk geometry is the wrong quantity and can be many decades smaller than the geometrical capacitance of the thin insulating layer(s). The real value of dielectric permittivity of the system at a low frequency, which is close to the dielectric constant of the dielectric layer, should be estimated in terms of the geometry of insulating layer rather than bulk capacitor.

$$\varepsilon_i = \frac{C}{C_{\mathrm{i}}} = \frac{C t_i}{\varepsilon_0 A} \tag{2}$$

Where t_i is the thickness of an insulating layer. We note that the thickness of a capacitor (i.e., t) is much higher than that of a dielectric layer (i.e., t_{i}). Thus, although the true dielectric constant of the interface region (ε_i) has a normal magnitude, very large apparent values of dielectric permittivity (ε) can be estimated if we use the bulk geometry for calculation. Therefore, the calculated dielectric permittivity with an ultrahigh value, which is estimated from geometrical capacitance of bulk ceramics, seems to be incorrect. As discussed above, the obtained high dielectric permittivity would originate from the interfacial dielectric layers, not bulk ceramics. Further studies are highly desirable to clarify the relationship between the formation of a dielectric layer at the electrode/ceramic interface and the obtained ultrahigh dielectric permittivity in hydrogenated $BaTiO_3$ ceramics.

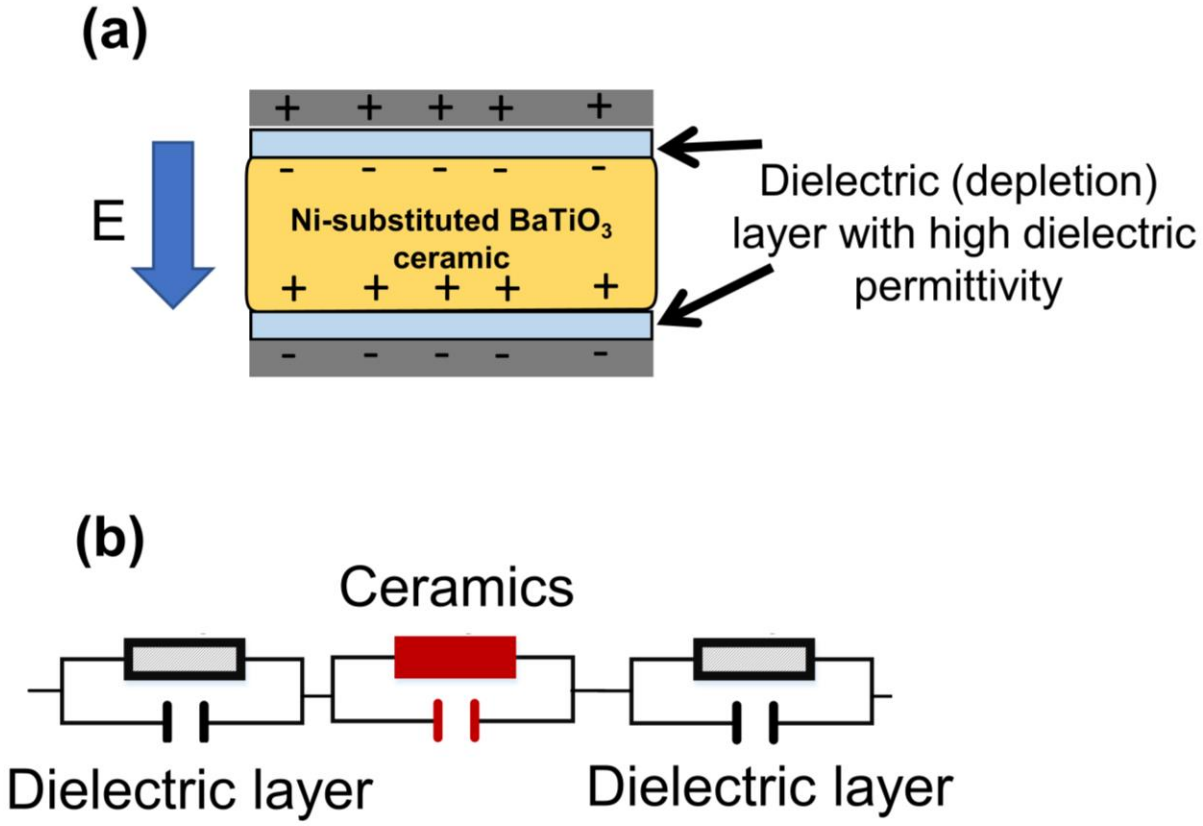

Figure 4.22 (a) The formation of interracial dielectric layers between the ceramic and electrodes. (b) The corresponding electrical equivalent of Ni-substituted $BaTiO_3$ ceramic capacitor with the contribution of interfacial dielectric layers.

4.7.3. Maxwell-Wagner effect

The Maxwell–Wagner effect accounts for charge accumulation at the interface of two materials on the basis of the difference of dielectric permittivity and electrical conductivity in these two materials [66]. Macroscopic electrical properties of materials are characterized by using two physical parameters. These are dielectric constant ε and conductivity σ. The ratio $\tau = \varepsilon/\sigma$ gives a relaxation time and stands for the spreading time of excess free carriers in the materials. That is, a steady-state charge distribution is established after a relaxation time. In other words, this value of

relaxation time (τ) specifies the electrical properties of materials in terms of carrier transport. Charge accumulation is allowed at the interface between two materials with different relaxation times when a current lows across the interface [66].

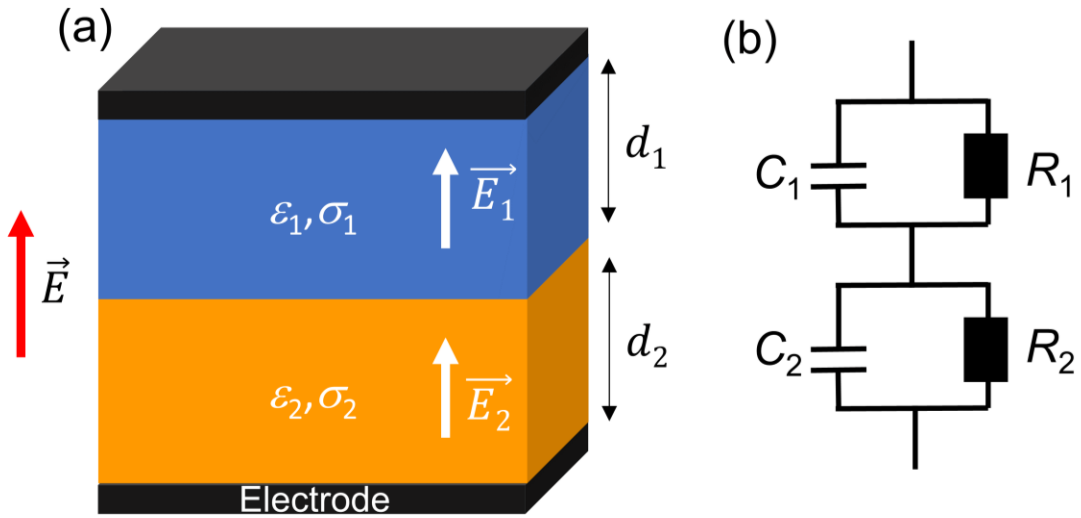

Figure 4.23 (a) The capacitor system with two dielectric layers. (b) The corresponding electrical equivalent for two layer dielectrics in series.

We consider the classic example of the Maxwell-Wagner effect by examining a system of two dielectric layers that have different electrical conductivity (σ) and dielectric permittivity (ε) (as shown in Figure 4.23). This process is equivalent to charging two series capacitors when a current flows across the interface of two materials. The conduction current through each material is given by [66, 67]

$$J_1 = \sigma_1 E_1 \quad (1)$$

$$J_2 = \sigma_2 E_2 \quad (2)$$

where E_1 and E_2 represent the electric fields, σ_1 and σ_2 are the electrical conductivities of the two component dielectrics, respectively. In a steady state, the current density is identical in the entire system.

$$J = J_1 = J_2 \tag{3}$$

$$\sigma_1 E_1 = \sigma_2 E_2 \tag{4}$$

According to the Gauss‘s law at the interfacial region of two dielectric materials, the surface change density at the interface of two dielectrics is given by.

$$\rho_s = \varepsilon_1 E_1 - \varepsilon_2 E_2 \tag{5}$$

From the equations of (4) and (5), the surface charge density at the interface of two dielectrics is also expressed [66]

$$\rho_s = J\left(\frac{\varepsilon_1}{\sigma_1} - \frac{\varepsilon_2}{\sigma_2}\right) \tag{6}$$

Equation (6) shows that the charge is accumulated at the interface between two dielectrics when the relaxation times (i.e., the ratio between the dielectric permittivity and electrical conductivity) of two dielectric materials are different. This is the Maxwell–Wagner effect, and accounts for charge accumulation phenomena observed in all kinds of two-material interfaces.

Now, we derive the real (ε) and imaginary (ε') parts of the dielectric permittivity of the two-layer dielectric system under the *ac* field. The equivalent electrical circuit is shown in Figure 4.23. The admittance of the equivalent circuit is given by [66, 68]

$$Y = \frac{Y_1 Y_2}{Y_1 + Y_2} \tag{7}$$

$$Y_1 = \frac{1}{R_1} + j\omega C_1 \tag{8}$$

$$Y_2 = \frac{1}{R_2} + j\omega C_2 \tag{9}$$

We further substitute equations (10), (11), and (12) into (7)

$$\tau_1 = R_1 C_1 = \frac{\varepsilon_1}{\sigma_1} \tag{10}$$

$$\tau_2 = R_2 C_2 = \frac{\varepsilon_2}{\sigma_2} \tag{11}$$

$$\tau_2 = \frac{(C_1 + C_2) R_1 R_2}{R_1 + R_2} \tag{12}$$

Hence the admittance may be rewritten.

$$Y = \frac{1}{R_1 + R_2} \frac{(1 + j\omega\tau_1)(1 + j\omega\tau_2)}{1 + j\omega\tau} \tag{13}$$

The relationship between admittance and complex permittivity of the capacitance as

$$Y = j\omega\varepsilon^* C_0 = j\omega C_0(\varepsilon + j\varepsilon') \tag{14}$$

Where

$$C_0 = \frac{A\varepsilon_0}{d}, \qquad d = d_1 + d_2 \tag{15}$$

We obtain the real and imaginary parts of dielectric permittivity as following.

$$\varepsilon = \frac{1}{(R_1 + R_2) C_0} \frac{[(\tau_1 + \tau_2) - \tau(1 - \omega^2 \tau_1 \tau_2)}{1 + \omega^2 \tau^2} \tag{16}$$

$$\varepsilon' = \frac{1}{\omega(R_1 + R_2) C_0} \frac{[1 - \omega^2 \tau_1 \tau_2 + \omega^2 \tau(\tau_1 + \tau_2)]}{1 + \omega^2 \tau^2} \tag{17}$$

When $\omega = 0$ the equation (16) reduces to

$$\varepsilon = \varepsilon_s = \frac{(\tau_1 + \tau_2) - \tau}{(R_1 + R_2) C_0} \tag{18}$$

When $\omega = \infty$ the equation (16) reduces to

$$\varepsilon = \varepsilon_\infty = \frac{\tau_1 \tau_2}{\tau} \frac{1}{(R_1 + R_2) C_0} \tag{19}$$

Substituting equation (18) and (19) in (16) and (17), we obtain

$$\varepsilon = \varepsilon_\infty + \frac{(\varepsilon_s - \varepsilon_\infty)}{1 + \omega^2 \tau^2} \tag{20}$$

$$\varepsilon' = \frac{1}{\omega (R_1 + R_2) C_0} + \frac{\omega \tau (\varepsilon_s - \varepsilon_\infty)}{1 + \omega^2 \tau^2} \tag{21}$$

Figure 4.24 shows the real and imaginary parts of complex dielectric permittivity as a function of frequency. As shown in Figure 4.24, the dielectric permittivity (ε) is enhanced at low-frequency region, and then decreases with the increase of frequency. The enhancement of overall dielectric permittivity is attributed to the production of interfacial polarization (i.e., space charge polarization), which originates from the accommodation of mobile charges at the interface between two materials. In the imaginary part (ε') of complex dielectric permittivity, there are two terms. The second term is Debye relaxation, while the first term is due to electrical conductivity.

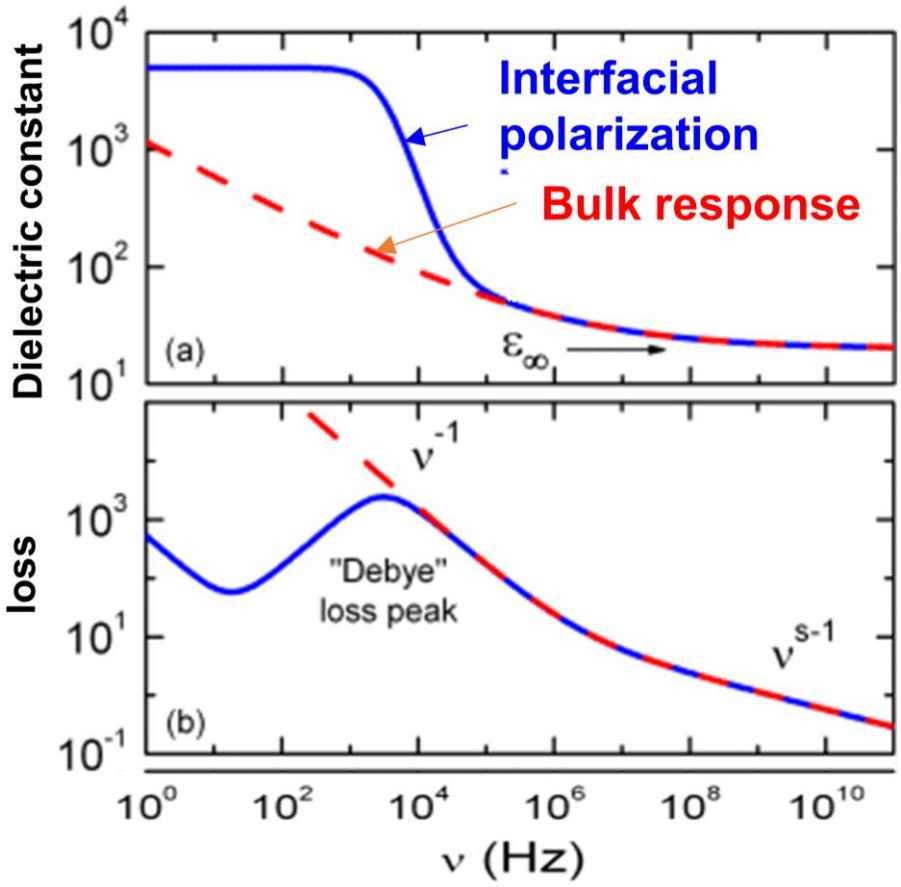

Figure 4.24 The frequency-dependent dielectric response for the capacitor system with two dielectric layers. Solid lines indicate the overall dielectric response including the contribution of interfacial polarization. Dashed lines show intrinsic bulk response [64].

Here, we note that the Maxwell-Wagner effect would be a possible original mechanism of the obtained ultrahigh dielectric permittivity in Ni-substituted $BaTiO_3$. After the hydrogenation through the water dissociation, the Ni-substituted $BaTiO_3$ ceramic is an inhomogeneous structure including the oxygen-deficient grain boundaries and the hydrogenated grains (Figure 4.25). If the electrical and dielectric properties (i.e., ε and σ) are different between grains and grain boundaries, interfacial polarization can occur due to the accommodation of mobile charges at the interface.

The produced interfacial polarization contributes to the overall polarization leading to the increase in dielectric responses of Ni-substituted $BaTiO_3$ ceramics.

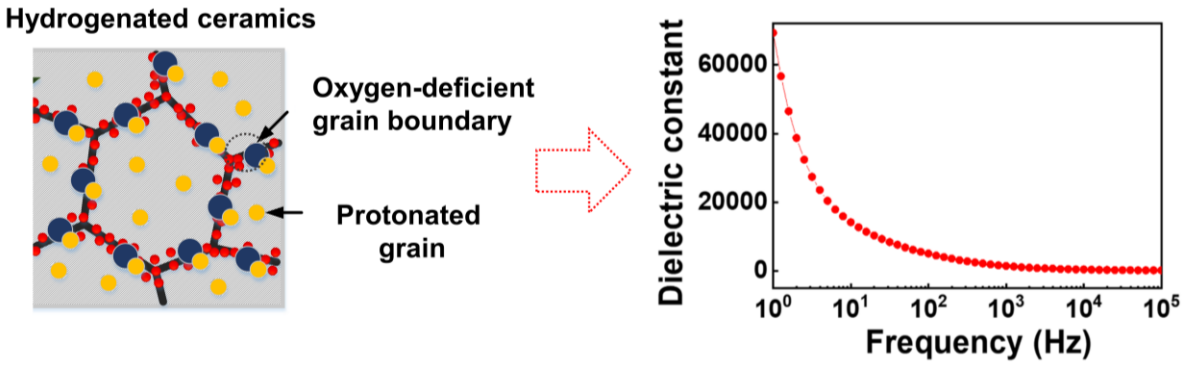

Figure 4.25 The possible mechanism of the ultrahigh dielectric permittivity in Ni-substituted $BaTiO_3$ ceramics by hydrogenation according to the Maxwell-Wagner effect. The interfacial polarization would appear due to the difference in permittivity and conductivity between oxygen-deficient grain boundaries and protonated grains resulting in the enhancement of dielectric responses.

4.7.4. Electrical polarization induced by surface hydroxyl ions

When an electric dipole is under a uniform electric field, the electrostatic force on the charges tends to rotate the dipole along the field direction (*E*) (Figure 4.26). The positive charge will be subjected to an electric force of in the leftward direction, while the negative charge will be subjected to an electric force in the rightward direction The magnitude of force on each charge equals the charge multiplied by a value of electric field.

$$\vec{F} = \vec{E} \times q \qquad (1)$$

The torque (τ) produced on an electric dipole by an electric field can be expressed as a vector product of the electric field and the electric dipole moment.

$$\vec{\tau} = \vec{E} \times \vec{p} \tag{2}$$

An electric field produces a torque on a dipole leading to the rotation of an electric dipole for a low energy configuration. The alignment of electric dipoles under electric field induces an electrical polarization with same field direction.

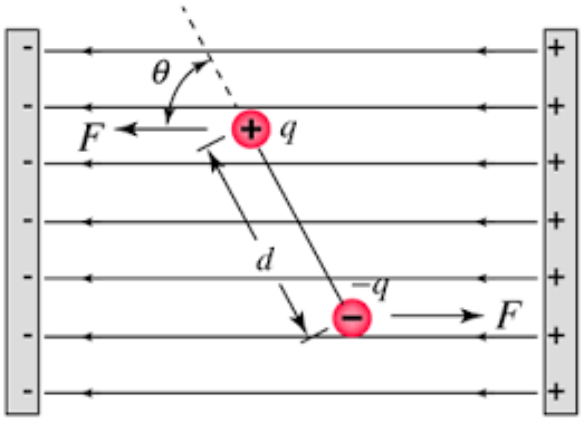

Figure 4.26 The electrical dipole under a uniform electric field. The electrostatic force on the charges tends to rotate the dipole along the direction of electric field (*E*).

The response of polar hydroxyl ions on the surface of ceramics to the electric field would induce electrical polarization contributing to the overall dielectric permittivity of Ni-substituted $BaTiO_3$ ceramics. In the complex oxides, the polar adsorbed specimens are very susceptible to the applied electric field [69]. The alignment of the polar adsorbates can produce additional polarization leading to enhanced dielectric responses. We note that when the Ni-substituted $BaTiO_3$ ceramics are hydrogenated through water dissociation, the separated hydrogen ions (H^+) are introduced into the oxide ceramics. Simultaneously, hydroxyl ions (OH^-) formed by the

dissociation of water molecules tend to be adsorbed at the oxygen vacancies on the ceramic surfaces. It is important to acknowledge that hydroxyl ions possess polarity, characterized by an electrical dipole moment. Consequently, the adsorbed hydroxyl ions on the ceramic surfaces exhibit a responsive behavior towards the applied electric field. These polar hydroxyl ions align themselves parallel to the electric field, thereby generating electrical polarization, as illustrated in Figure 4.27. The resultant polarization induced by the presence of surface hydroxyl ions contributes to an enhancement in the dielectric response of Ni-substituted $BaTiO_3$ ceramics. By incorporating hydrogen and adsorbing hydroxyl ions, these ceramics demonstrate an intensified dielectric behavior, effectively influenced by the response of polar hydroxyl ions to the electric field. Further studies are highly needed to clarify this phenomenon of surface chemistry and ion interactions in conjunction with the dielectric properties of Ni-substituted $BaTiO_3$ ceramics.

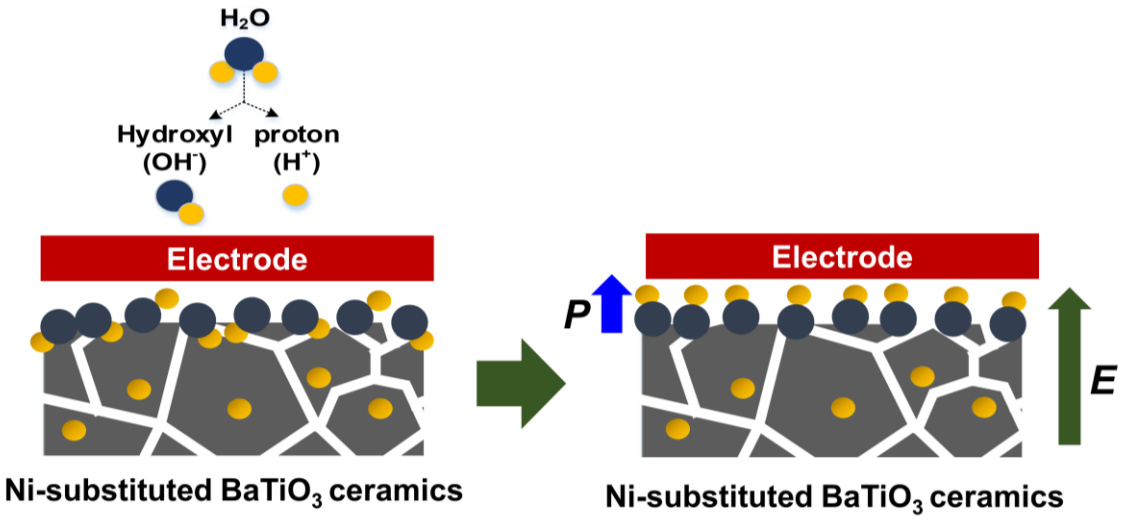

Figure 4.27 The alignment of polar hydroxyl ions under an applied electric field would induce electrical polarization resulting in high dielectric responses in Ni-substituted $BaTiO_3$.

4.7.5. Internal barrier layer capacitor at grain boundaries

The barrier layer capacitor (IBLC) model is widely used to explain the high dielectric response in polycrystalline ceramics [10]. Polycrystalline ceramics consist of a large number of grains and grain boundaries. To simplify, we use a brick-layer model, where a polycrystalline ceramic was conceptually assumed to consist of indistinguishable cubic bricks split by flat layers (Figure 4.28). In the barrier layer capacitor model, we consider polycrystalline ceramics with an electrically heterogeneous microstructure including conductive grains and dielectric grain boundaries. In this IBLC system, the total capacitance of ceramics is equivalent to the number (i.e., $n \sim \frac{d}{t_g}$) of dielectric grain boundary capacitors (i.e., the dielectric grain boundary layers indicated by the hatched squares in Figure 4.28), connected in series by the conductive grains [70]. Since each grain boundary layer has a capacitance of $\sim \frac{\varepsilon_{gb} A}{t_{gb}}$ (A is the surface area, t_{gb} the thickness of grain boundaries, and ε_{gb} the relative permittivity), the total capacitance of the ceramics is estimated by [70]:

$$C_{total} = \frac{\varepsilon_{gb} A}{n t_{gb}} = \frac{d \varepsilon_{gb} A}{t_g t_{gb}} \quad (1)$$

Therefore, the relative dielectric permittivity of ceramics is given by:

$$\varepsilon_r = \frac{\varepsilon_{gb} t_g}{t_{gb}} \quad (2)$$

According to equation (2), a material with an extremely high dielectric permittivity can be achieved due to a high t_g/t_{gb} ratio.

The obtained high dielectric constant in Ni-substituted $BaTiO_3$ ceramics would be discussed based on the barrier layer capacitor (IBLC) model. After protonation, the grains of Ni-substituted $BaTiO_3$ ceramics become conductive due to the introduction of hydrogen ions. The

hydroxyl ions dissociated from water molecules are adsorbed at oxygen vacancies sites along the gain boundaries. If grain boundaries of ceramics are dielectrics with high permittivity, the giant dielectric permittivity in Ni-substituted $BaTiO_3$ would be attributed to internal barrier layer capacitance (IBLC) at grain boundaries.

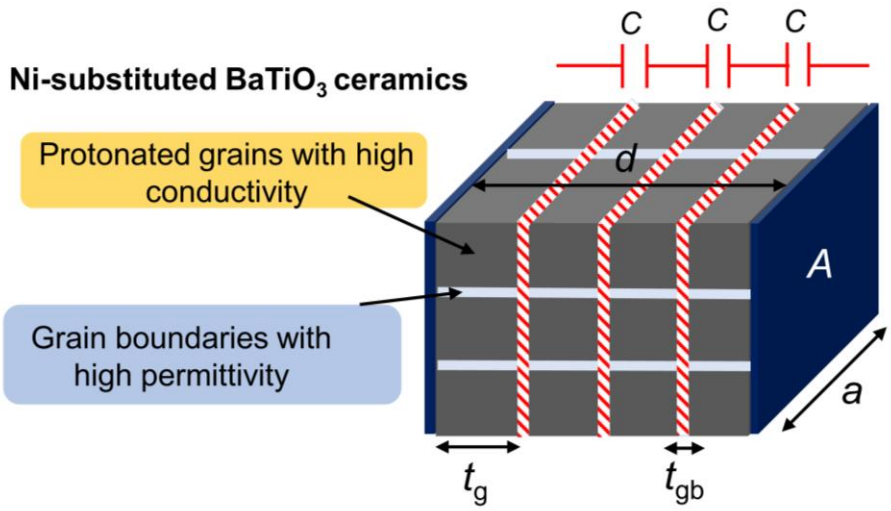

Figure 4.28 The barrier layer capacitor (IBLC) model in polycrystalline ceramics.

In this study, an ultrahigh dielectric permittivity is obtained in Ni-substituted $BaTiO_3$ ceramics by hydrogenation through water dissociation. Furthermore, the dielectric relaxation characteristics in Ni-substituted $BaTiO_3$ are reversibly controllable by external stimuli (i.e., the treatment under ambient environments and thermal annealing). In the discussion part, different possible mechanisms have been discussed to elucidate the observed phenomena of ultrahigh dielectric permittivity in Ni-substituted $BaTiO_3$ ceramics by hydrogenation. To understand the exact microscopic origin of colossal dielectric responses, further experimental analyses in conjunction with theoretical calculations are highly desirable.

References

1. K. C. Kao, *Dielectric phenomena in solids* (Elsevier, 2004).
2. J.-K. Huang, Y. Wan, J. Shi, J. Zhang, Z. Wang, W. Wang, N. Yang, Y. Liu, C.-H. Lin, X. Guan, L. Hu, Z.-L. Yang, B.-C. Huang, Y.-P. Chiu, J. Yang, V. Tung, D. Wang, K. Kalantar-Zadeh, T. Wu, X. Zu, L. Qiao, L.-J. Li, S. Li, *Nature* **605**, 262-267 (2022).
3. A. I. Kingon, J.-P. Maria, S. K. Streiffer, *Nature* **406**, 1032-1038 (2000).
4. S. Krohns, P. Lunkenheimer, S. Meissner, A. Reller, B. Gleich, A. Rathgeber, T. Gaugler, H. U. Buhl, D. C. Sinclair, A. Loidl, *Nat. Mater.* **10**, 899-901 (2011).
5. S. C. B. Mannsfeld, B. C. K. Tee, R. M. Stoltenberg, C. V. Chen, S. Barman, B. V. O. Muir, A. N. Sokolov, C. Reese, Z. Bao, *Nat. Mater.* **9**, 859-864 (2010).
6. W. H. Ko, Q. Wang, *Sens. Actuator A Phys.* **75**, 242-251 (1999).
7. C. C. Homes, T. Vogt, S. M. Shapiro, S. Wakimoto, A. P. Ramirez, *Science* **293**, 673-676 (2001).
8. M. A. Subramanian, D. Li, N. Duan, B. A. Reisner, A. W. Sleight, *J. Solid State Chem.* **151**, 323-325 (2000).
9. A. P. Ramirez, M. A. Subramanian, M. Gardel, G. Blumberg, D. Li, T. Vogt, S. M. Shapiro, *Solid State Commun.* **115**, 217-220 (2000).
10. D. C. Sinclair, T. B. Adams, F. D. Morrison, A. R. West, *Appl. Phys. Lett.* **80**, 2153-2155 (2002).
11. P. Lunkenheimer, R. Fichtl, S. G. Ebbinghaus, A. Loidl, *Phys. Rev. B* **70**, 172102 (2004).
12. M. Acosta, N. Novak, V. Rojas, S. Patel, R. Vaish, J. Koruza, G. Rossetti Jr, J. Rödel, *Appl. Phys. Rev.* **4**, 041305 (2017).

13. M. E. Lines, A. M. Glass, *Principles and applications of ferroelectrics and related materials* (Oxford university press, 2001).

14. B. Jaffe, W. Cook, H. Jaffe, *Piezoelectric Ceramics* (Academic Press, London, 1971).

15. M. Dawber, K. M. Rabe, J. F. Scott, *Rev. Mod. Phys.* **77**, 1083 (2005).

16. H. Han, C. Voisin, S. Guillemet-Fritsch, P. Dufour, C. Tenailleau, C. Turner, J. C. Nino, *J. Appl. Phys.* **113**, 024102 (2013).

17. S. Guillemet-Fritsch, Z. Valdez-Nava, C. Tenailleau, T. Lebey, B. Durand, J.-Y. Chane-Ching, *Adv. Mater.* **20**, 551-555 (2008).

18. Q. Liu, J. Liu, D. Lu, W. Zheng, *Ceram. Int.* **44**, 7251-7258 (2018).

19. W. Hu, Y. Liu, R. L. Withers, T. J. Frankcombe, L. Norén, A. Snashall, M. Kitchin, P. Smith, B. Gong, H. Chen, S. Jason, F. Brink, J. Wong-Leung, *Nat. Mater.* **12**, 821-826 (2013).

20. Y. Song, X. Wang, Y. Sui, Z. Liu, Y. Zhang, H. Zhan, B. Song, Z. Liu, Z. Lv, L. Tao, J. Tang, *Sci. Rep.* **6**, 1-8 (2016).

21. G. Wang, C. Wang, S. Huang, C. Lei, X. Sun, T. Li, L. Liu, *J. Am. Ceram. Soc.* **96**, 2203-2210 (2013).

22. W. Z. Yang, M. S. Fu, X. Q. Liu, H. Y. Zhu, X. M. Chen, *Ceram. Int.* **37**, 2747-2753 (2011).

23. H. Yoon, M. Choi, T.-W. Lim, H. Kwon, K. Ihm, J. K. Kim, S.-Y. Choi, J. Son, *Nat. Mater.* **15**, 1113-1119 (2016).

24. A. Janotti, C. G. Van de Walle, *Nat. Mater.* **6**, 44-47 (2007).

25. S. Shen, Z. Li, Z. Tian, W. Luo, S. Okamoto, P. Yu, *Phys. Rev. X* **11**, 021018 (2021).

26. N. Lu, P. Zhang, Q. Zhang, R. Qiao, Q. He, H.-B. Li, Y. Wang, J. Guo, D. Zhang, Z. J. N. Duan, **546**, 124-128 (2017).

27. J. Lee, Y. Ha, S. Lee, *Adv. Mater.* **33**, 2007606 (2021).

28. H. Lee, T. H. Kim, J. J. Patzner, H. Lu, J.-W. Lee, H. Zhou, W. Chang, M. K. Mahanthappa, E. Y. Tsymbal, A. Gruverman, C.-B. Eom, *Nano Lett.* **16**, 2400-2406 (2016).

29. R. Schaub, P. Thostrup, N. Lopez, E. Lægsgaard, I. Stensgaard, J. K. Nørskov, F. Besenbacher, *Phys. Rev. Lett.* **87**, 266104 (2001).

30. D. C. Sinclair, J. M. S. Skakle, F. D. Morrison, R. I. Smith, T. P. Beales, *J. Mater. Chem.* **9**, 1327-1331 (1999).

31. R. D. Burbank, H. T. Evans, *Acta Crystallogr.* **1**, 330-336 (1948).

32. H. T. Langhammer, T. Müller, K. H. Felgner, H. P. Abicht, *J. Am. Ceram. Soc.* **83**, 605-611 (2000).

33. N. X. Duong, J.-S. Bae, J. Jeon, S. Y. Lim, S. H. Oh, A. Ullah, M. Sheeraz, J. San Choi, J.-H. Ko, S. M. Yang, K.-H. Kim, I. W. Kim, C. W. Ahn, T. H. Kim, *Ceram. Int.* **45**, 16305-16310 (2019).

34. G. M. Keith, M. J. Rampling, K. Sarma, N. M. Alford, D. C. Sinclair, *J. Eur. Ceram. Soc.* **24**, 1721-1724 (2004).

35. R. E. Cohen, *Nature* **358**, 136-138 (1992).

36. K. D. Kreuer, *Solid State Ion.* **125**, 285-302 (1999).

37. A. Hanada, K. Kinoshita, S. Kishida, *Appl. Phys. Lett.* **101**, 043507 (2012).

38. H. Han, C. Davis III, J. C. Nino, *J. Phys. Chem. C* **118**, 9137-9142 (2014).

39. R. M. Glaister, H. F. Kay, *Proc. Phys. Soc.* **76**, 763 (1960).

40. S. M. Gaytan, M. A. Cadena, H. Karim, D. Delfin, Y. Lin, D. Espalin, E. MacDonald, R. B. Wicker, *Ceram. Int.* **41**, 6610-6619 (2015).

41. H. Kim, A. Renteria-Marquez, M. D. Islam, L. A. Chavez, C. A. Garcia Rosales, M. A. Ahsan, T. L. B. Tseng, N. D. Love, Y. Lin, *J. Am. Ceram. Soc.* **102**, 3685-3694 (2019).

42. G. Panchal, D. K. Shukla, R. J. Choudhary, V. R. Reddy, D. M. Phase, *J. Appl. Phys.* **122**, 085310 (2017).

43. S. Majumder, P. Basera, M. Tripathi, R. J. Choudhary, S. Bhattacharya, K. Bapna, D. M. Phase, *J. Phys. Condens. Matter* **31**, 205001 (2019).

44. M. Sheeraz, M. U. Rashid, A. Ali, F. Akram, H. J. Lee, J. San Choi, J.-S. Bae, Y. S. Kim, Y.-H. Shin, C. W. Ahn, T. H. Kim, *J. Eur. Ceram. Soc.* **41**, 5155-5162 (2021).

45. R. Yimnirun, J. Tangsritrakul, S. Rujirawat, S. Limpijumnong, *Ferroelectrics* **381**, 130-143 (2009).

46. J. F. Scott, *J. Phys. Condens. Matter* **20**, 021001 (2007).

47. K. Parida, S. Das, P. K. Mahapatra, R. N. P. Choudhary, *Mater. Res. Bull.* **111**, 7-16 (2019).

48. W. Q. Cao, L. F. Xu, M. M. Ismail, L. L. Huang, *Mater. Sci.-Poland* **34**, 322-329 (2016).

49. L. Ni, M. Fu, X. Ren, Y. Zhang, *J. Mater. Sci: Mater. Electron.* **28**, 10191-10198 (2017).

50. Y. Wu, X. Zhao, J. Zhang, W. Su, J. Liu, *Appl. Phys. Lett.* **107**, 242904 (2015).

51. Y. Song, P. Liu, W. Wu, Q. Zhou, *J. Eur. Ceram. Soc.* **41**, 4146-4152 (2021).

52. N. M. Beekmans, L. Heyne, *Electrochim. Acta* **21**, 303-310 (1976).

53. H. Näfe, *Solid State Ion.* **13**, 255-263 (1984).

54. J. R. Macdonald, E. Barsoukov, *Impedance spectroscopy: theory, experiment, and applications* (Wiley, 2005).

55. D. C. Sinclair, A. R. West, *J. Appl. Phys.* **66**, 3850-3856 (1989).

56. J. S. Choi, C. W. Ahn, J.-S. Bae, T. H. Kim, *Curr. Appl. Phys.* **20**, 102-105 (2020).

57. C. Miot, E. Husson, C. Proust, R. Erre, J. P. Coutures, *J. Mater. Res.* **12**, 2388-2392 (1997).

58. D. E. Newbury, N. Ritchie, *Microsc. Microanal.* **22**, 735-753 (2016).

59. A. C. Caballero, M. Villegas, J. F. Fernandez, M. Viviani, M. T. Buscaglia, M. Leoni, *J. Mater. Sci. Lett.* **18**, 1297-1299 (1999).

60. E. Sun, W. Cao, *Prog. Mater. Sci.* **65**, 124-210 (2014).

61. C. H. Park, D. J. Chadi, *Phys. Rev. Lett.* **84**, 4717 (2000).

62. F. Li, S. Zhang, D. Damjanovic, L. Q. Chen, T. R. Shrout, *Adv. Funct. Mater.* **28**, 1801504 (2018).

63. N. Qu, H. Du, X. Hao, *J. Mater. Chem. C* **7**, 7993-8002 (2019).

64. P. Lunkenheimer, V. Bobnar, A. V. Pronin, A. I. Ritus, A. A. Volkov, A. Loidl, *Phys. Rev. B* **66**, 052105 (2002).

65. P. Lunkenheimer, S. Krohns, S. Riegg, S. G. Ebbinghaus, A. Reller, A. Loidl, *Eur. Phys. J. Special Topics* **180**, 61 (2010).

66. B. Bhushan, *Encyclopedia of nanotechnology* (Springer, 2012).

67. C. Li, G. Chen, X. Qiu, Q. Lou, X. Gao, *AIP Adv.* **11**, 065227 (2021).

68. H. A. Von, R. Arthur, *Dielectrics and Waves* (Wiley, 1954).

69. D. D. Xu, R. R. Ma, A. P. Fu, Z. Guan, N. Zhong, H. Peng, P. H. Xiang, C. G. Duan, *Nat. Commun.* **12**, 655 (2021).

70. R. Mauczok, R. Wernicke, *Philips Tech. Rev.* **41**, 338 (1983).

Chapter 5

Reversible control of dielectric permittivity in oxide ceramics for sensing devices

5.1. Potential applications of the 6H-hexagonal $BaTiO_3$ ceramics for gas sensors

The 6H-hexagonal $BaTiO_3$ ceramics are of practical interest for realizing the sensing devices due to the sensitivity of dielectric and electrical properties to the ambient environment. As discussed in the previous chapter, the dielectric responses of Ni-substituted $BaTiO_3$ are reversibly manipulated by external stimuli. An ultrahigh dielectric constant (i.e., on-state) is obtained in Ni-substituted $BaTiO_3$ ceramics by hydrogenation through a specific treatment under ambient conditions. The thermal annealing restores the high dielectric permittivity (i.e., on-state) to the original value (i.e., off-state). Considering that the dielectric constant is closely coupled with electrical conductivity in lossy dielectrics [1, 2], the dielectric and associated electrical responses in Ni-substituted $BaTiO_3$ are controllable by a specific treatment under ambient environments and thermal annealing. The reversible control of dielectric permittivity and related electrical conductivity in Ni-substituted $BaTiO_3$ ceramics would allow us to implement a new concept of oxide-ceramic-based dielectric sensors.

5.2. Set-up of sensing performance experiments

We examined the evolution of dielectric responses in Ni-substituted $BaTiO_3$ ceramics under various ambient environments. The dielectric responses were measured in as-sintered $BaTiO_3$ ceramics. The Ni-substituted $BaTiO_3$ ceramics were treated in ambient air, vacuum, water vapor, N_2, and CO_2 for a particular time duration (for more details, see the method part in the

Chapter 2). After a specific treatment under ambient conditions, we remeasured the dielectric properties in the treated ceramics samples.

An experimental set-up was constructed for a specific treatment under an acetic acid environment. First, we inserted a few droplets of acetic acid (CH_3COOH, 99.7%, Sigma-Aldrich, USA) into the bottom of a glass jar. We put the pure and Ni-substituted $BaTiO_3$ ceramics in another beaker. Then, the beaker with the ceramic samples was placed inside the jar to separate the ceramics from the acid liquid. The glass jar was closed, and the ceramics remained under the acid acetic-rich environment. After 2 days, we took the ceramics out of the jar and re-measured the dielectric properties (for more details, see the method part in the Chapter 2). For a treatment under a liquid water environment, the as-sintered Ni-substituted $BaTiO_3$ ceramics were immersed in deionized water for 10 minutes at room temperature. After the water treatment, the ceramic samples were dried under a circumstance of N_2 gas flow at room temperature.

We experimentally demonstrated the reversible change between two dielectric states (i.e., on- and off-states) in Ni-substituted $BaTiO_3$ ceramics through high-humidity treatment and thermal annealing for 5 cycles. We first measured the frequency-dependent dielectric permittivity of the as-sintered Ni-substituted $BaTiO_3$ ceramics (i.e., off-state). Next, the as-sintered ceramics were treated under a high-humidity environment for the time duration of 1 hour. After the treatment, we re-measured the dielectric permittivity of the treated ceramics (i.e., on-state). To recover the dielectric on-state to the off-state, we thermally annealed the treated ceramics at 150°C for 1 hour in a box furnace and then, performed the dielectric constant measurement after the thermal annealing. The cycle of high-humidity treatment and thermal annealing was repeated 5 times in Ni-substituted $BaTiO_3$ ceramics to secure experimental reliability of the recyclability of the on- and off-states.

The humidity sensing properties of ceramic samples (e.g., Ni-substituted $BaTiO_3$) were measured in a quartz tube (diameter: 3 cm, length: 30 cm) at room temperature. The relative humidity levels (20-80 RH%) were calibrated by mixing the dry air with water vapor. Note that the humidity gas flow rate was 1000 sccm which was controlled by mass-flow controller (MFC). The electrical conductivity of ceramic samples was measured by using a *dc* bias voltage of 0.5 V with a Keithley 2401 source meter and all conductivity results were recorded by a home-made LabVIEW software.

5.3. Change of dielectric permittivity under different ambient conditions

5.3.1. Ambient air environment

To track the evolution of the dielectric responses to the ambient air in Ni-substituted $BaTiO_3$ ceramics, we measured the frequency-dependent dielectric permittivity in the ceramic samples for the different time duration of the air exposure. The frequency-dependent dielectric constant measurements were repeatedly performed in our ceramics with weekly time intervals [the experimental process in the schematic Figure 5.1(a)]. We observed that the dielectric permittivity in a low-frequency range (from 10^0 to 10^3 Hz) continuously increased with the increase of time duration [Figure 5.1(b)]. In particular, the dielectric constant ($\varepsilon \sim 2.5\times10^3$ at 1 Hz) in the as-sintered ceramics was enhanced up to the value of $\varepsilon \sim 4.6\times10^4$ after 6 weeks in the ambient air. As shown in Figure 5.1(c), the corresponding dielectric loss also increased after a treatment under the air environment. We plotted the dielectric constant values at 1 Hz as a function of the air-exposure time Figure 5.1(d). For the first two weeks, the dielectric constant varied around the finite value of $\varepsilon \sim 2.7\times10^3$. After two weeks, the dielectric permittivity started to increase dramatically and then, it reached a high value of $\varepsilon \sim 4.6\times10^4$ after a time duration of 6 weeks.

We reset the on-state in the treated ceramics by air exposure to the initial off-state by thermal annealing, as shown in Figure 5.1(a). The high dielectric constant in the low-frequency region returned to a low value [black solid squares in Figure 5.1(e)], while the dielectric loss also became reduced after thermal annealing [black solid squares in Figure 5.1(f)]. Then, we plotted the frequency-dependent dielectric constant and loss in the annealed ceramics as a function of the air-exposure time. Interestingly, the dielectric responses in the low-frequency region significantly increased after air exposure [Figure 5.1(e)]. The observed peak in the dielectric loss shifted to a higher frequency with the increase of the time duration [Figure 5.1(f)]. As shown in Figure 5.1(g), the dielectric permittivity kept increasing over the time and an extremely high dielectric constant ($\varepsilon \sim 6.9\times10^4$ at 1 Hz) was achieved after 6 weeks.

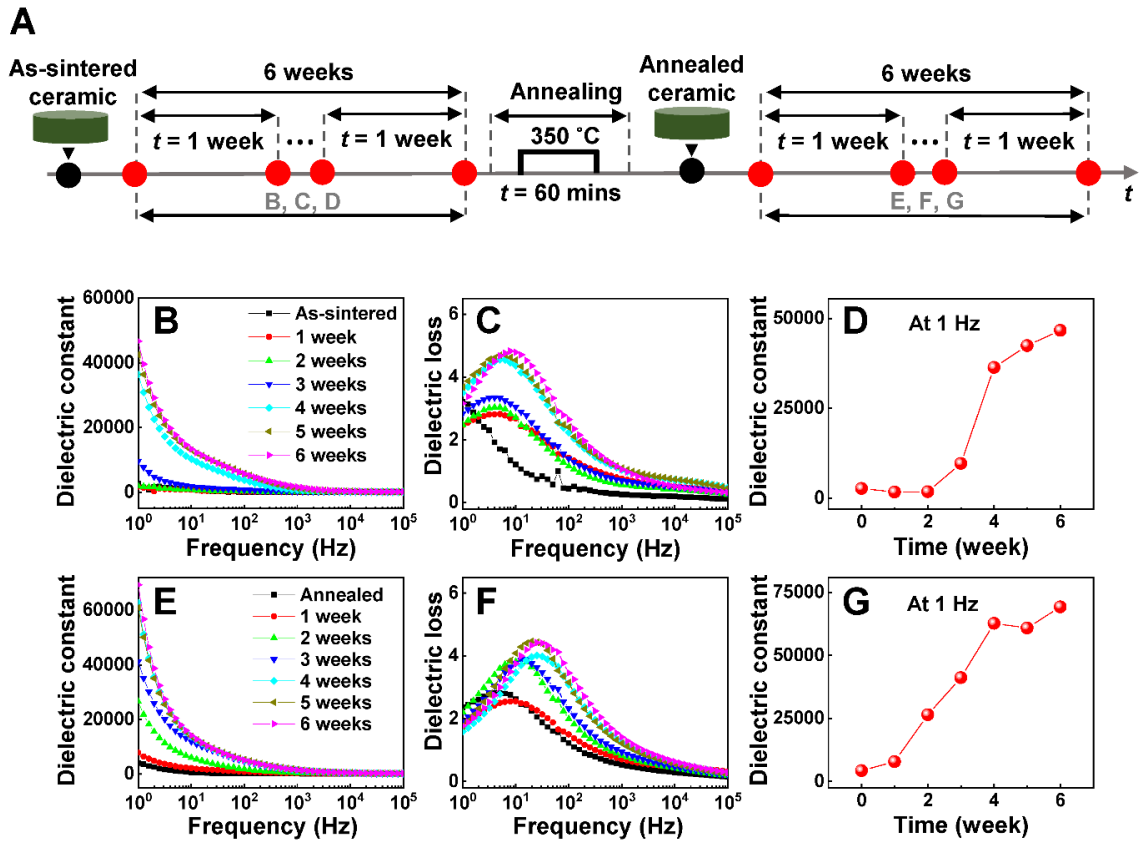

Figure 5.1 Evolution of dielectric responses in Ni-substituted $BaTiO_3$ ceramics under the ambient air environment. (a) A schematic of the experimental sequence. (b) The frequency-dependent dielectric permittivity in Ni-substituted $BaTiO_3$ ceramics for different time duration under the ambient air environment. (c) The corresponding dielectric loss as a function of frequency for different time duration of the air exposure. (d) The dielectric constant as a function of time duration at 1 Hz in (b). (e) The dielectric constant and (f) dielectric loss as a function of frequency in the annealed ceramics for different time duration of the air exposure. (g) The air-exposure time dependence of dielectric permittivity at 1 Hz in (e).

5.3.2. Humidity condition

Figure 5.2 showed the change of the dielectric permittivity and the corresponding dielectric loss in Ni-substituted $BaTiO_3$ ceramics under a high-humidity environment. At the as-sintered state, the dielectric constant was low ($\varepsilon \sim 10^3$, the on-state) in the whole measured frequency range. The low-frequency dielectric responses were enhanced after a treatment under a water vapor condition. An ultrahigh dielectric permittivity ($\varepsilon \sim 10^6$, the off-state) was achieved in the treated Ni-substituted $BaTiO_3$ [Figure 5.2(a)]. The enhanced dielectric constant was accompanied by the increase of corresponding dielectric loss [Figure 5.2(b)]. This indicated that the dielectric properties of our Ni-substituted $BaTiO_3$ were susceptible to moisture in ambient environments.

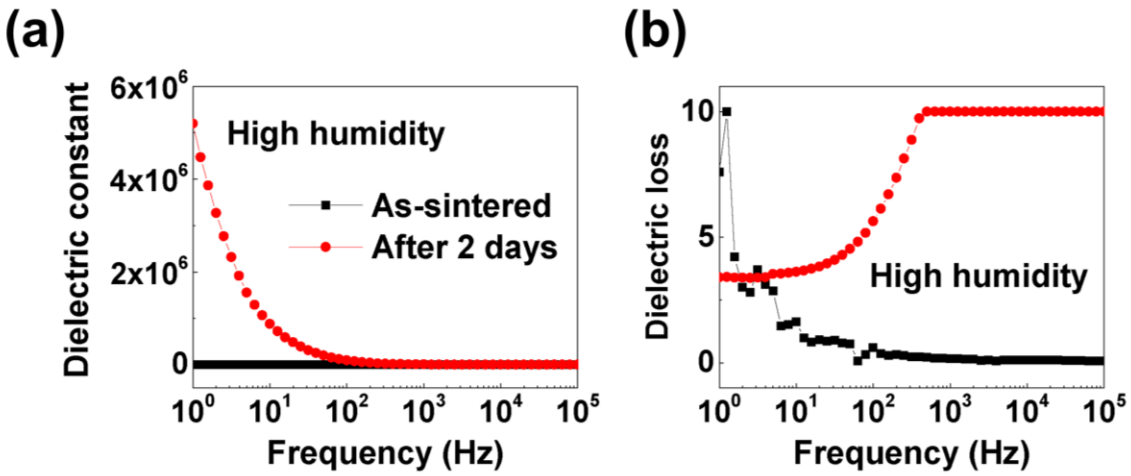

Figure 5.2 Change of (a) dielectric permittivity and (b) corresponding dielectric loss in Ni-substituted $BaTiO_3$ ceramics under the ambient air environment.

5.3.3. Acetic acid environment

Another route to modify the dielectric responses in Ni-substituted $BaTiO_3$ ceramics was an acetic acid (CH_3COOH) treatment. The experimental procedures of our acetic acid treatments were depicted in Chapter 2. Before the acetic acid treatments, the dielectric behaviors corresponded to the off-state [Figure 5.3(a)]. As shown in Figure 5.3(b), the low-frequency dielectric constant was dramatically enhanced by the acetic acid treatments. For the treated ceramic samples, we observed the extremely high dielectric permittivity ($\varepsilon \sim 10^6$ at 1Hz) which was three orders of magnitude larger that the initial value. We also identified that the dielectric constant rapidly decreased, when the sample was exposed to the ambient air after the acetic acid treatment [Figure 5.3(b)]. By plotting the dielectric constant as a function of the air-exposure time, we found that the dielectric permittivity continuously decreased over the time [Figure 5.3(c)]. Unlike the Ni-substituted

$BaTiO_3$ ceramics, the dielectric responses in pure $BaTiO_3$ ceramics were almost unchanged before and after the acetic acid treatment [Figure 5.3(d-f)].

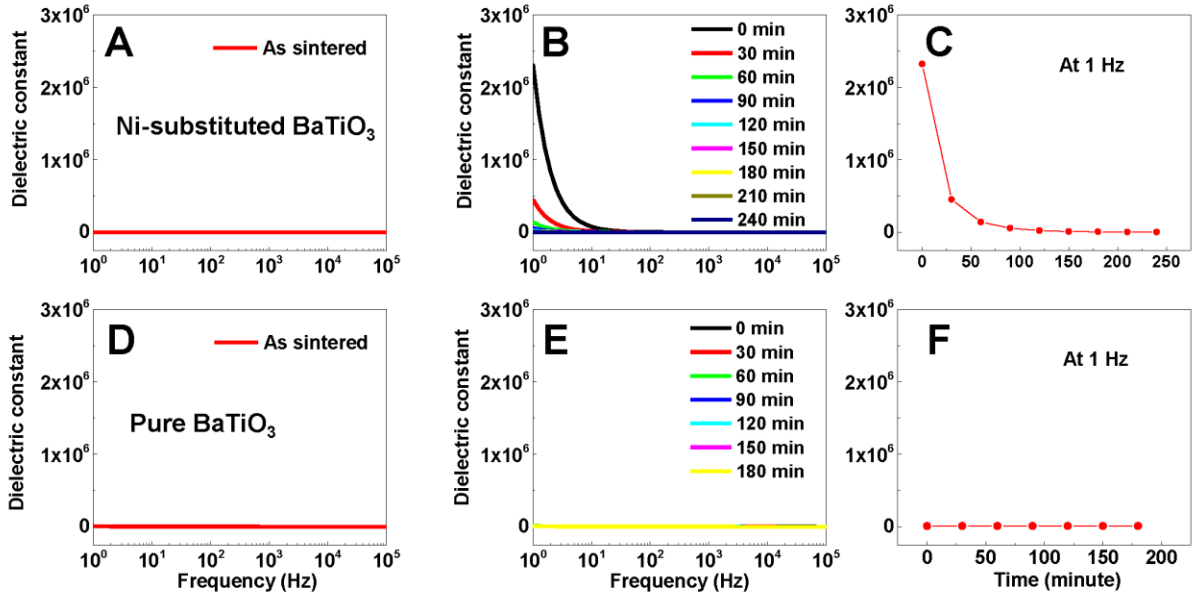

Figure 5.3 Change of dielectric responses in Ni-substituted $BaTiO_3$ ceramics under an acetic acid environment. (a and d) The dielectric constants as a function of frequency in (a) Ni-substituted and (d) pure $BaTiO_3$ ceramics for the as-sintered states. After a two-day treatment in the acetic acid environment, we re-measured the dielectric constants of the treated ceramics in the air. (b and e) The frequency dependences of dielectric constants in (b) Ni-substituted and (e) pure ceramics for various time duration of the exposure to ambient air. (c and f) The air-exposure time dependence of dielectric permittivity at 1 Hz in (b) and (e).

5.3.4. Water treatment

To further verify the effect of water molecules on the dielectric properties of Ni-substituted $BaTiO_3$ ceramics, a water-treatment experiment was conducted [Figure 5.4(a)]. As shown in Figure 5.4(b) and (c), we measured the dielectric permittivity and dielectric loss in Ni-substituted

$BaTiO_3$ ceramics before (black squares) and after (red circles) the water treatment. We found that the off-state immediately changed to the on-state after a short time duration (t ~ 10 minutes) of the water treatment. For a comparison, we also carried out the water-treatment experiment of pure $BaTiO_3$ ceramics. The dielectric responses of pure ceramics were almost unchanged before (black squares) and after (red circles) the water treatment [Figure 5.4(d) and (e)]. It was clear that a change in dielectric responses induced by the water treatment only emerged in for the Ni-substituted $BaTiO_3$ ceramics, not pure $BaTiO_3$.

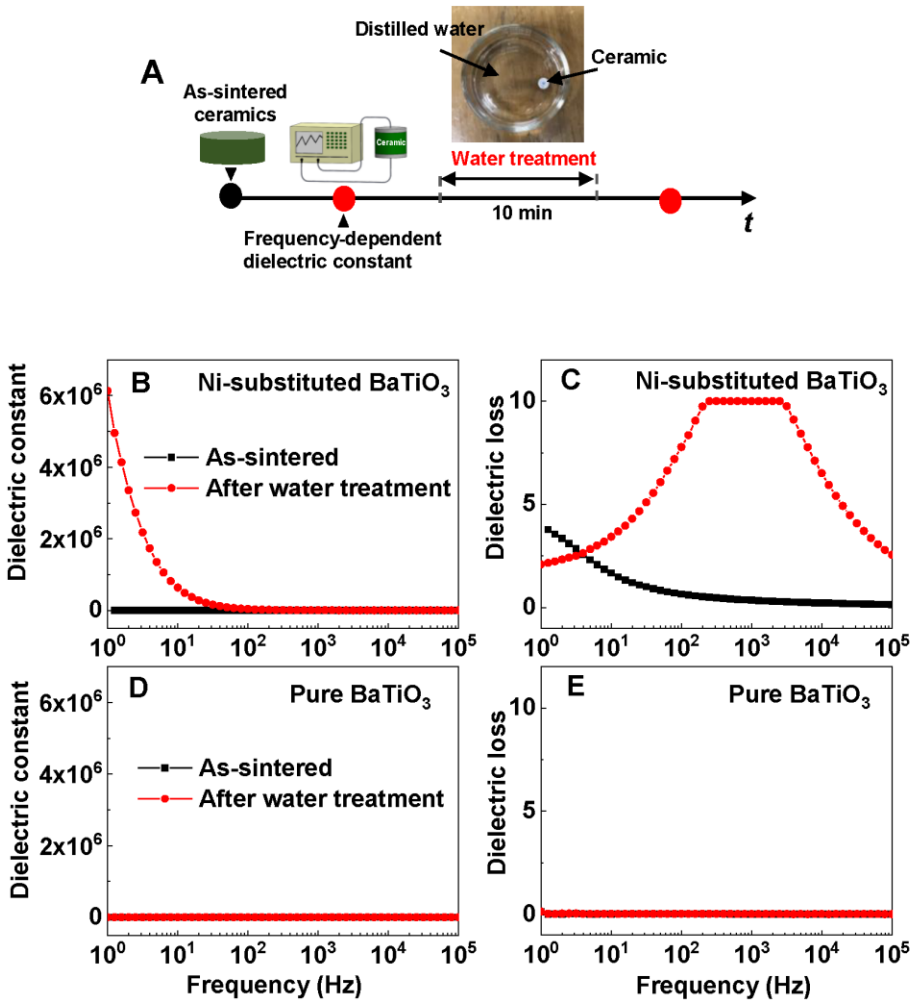

Figure 5.4 Change of dielectric responses in Ni-substituted $BaTiO_3$ ceramics induced by water treatment. (a) The sequence of the water-treatment experiment. We measured the dielectric properties of ceramic samples before and after the water treatment. (b) The dielectric constant and (c) the dielectric loss in Ni-substituted $BaTiO_3$ ceramics at the as-sintered state and after the water treatment. (d) The dielectric constant and (e) the dielectric loss of the pure $BaTiO_3$ ceramics at the as-sintered state and after the water treatment.

5.4. Reversible control of dielectric responses in Ni-substituted $BaTiO_3$ ceramics

We experimentally demonstrated the manipulation of dielectric permittivity in Ni-substituted $BaTiO_3$ ceramics by external stimuli. To examine the reproducibility of two different dielectric states in Ni-substituted $BaTiO_3$ ceramics, we repetitively performed the reversible change between on- and off- dielectric states through specific treatment under a humid environment and subsequent thermal annealing for 5 times [for more details, see Figure 5.5(a)]. As shown in Figure 5.5(b), the on- and off-states in dielectric responses of Ni-substituted $BaTiO_3$ ceramics were alternatively reproducible over 5 cycles of high-humidity treatment and thermal annealing. It should be noted that the ratio of the dielectric constant between on-state (i.e., the treated ceramics under a humid condition) and off-state (i.e., the ceramics after thermal treatment) was approximately 10^3 with a slight variation during the cycling process [Figure 5(c)].

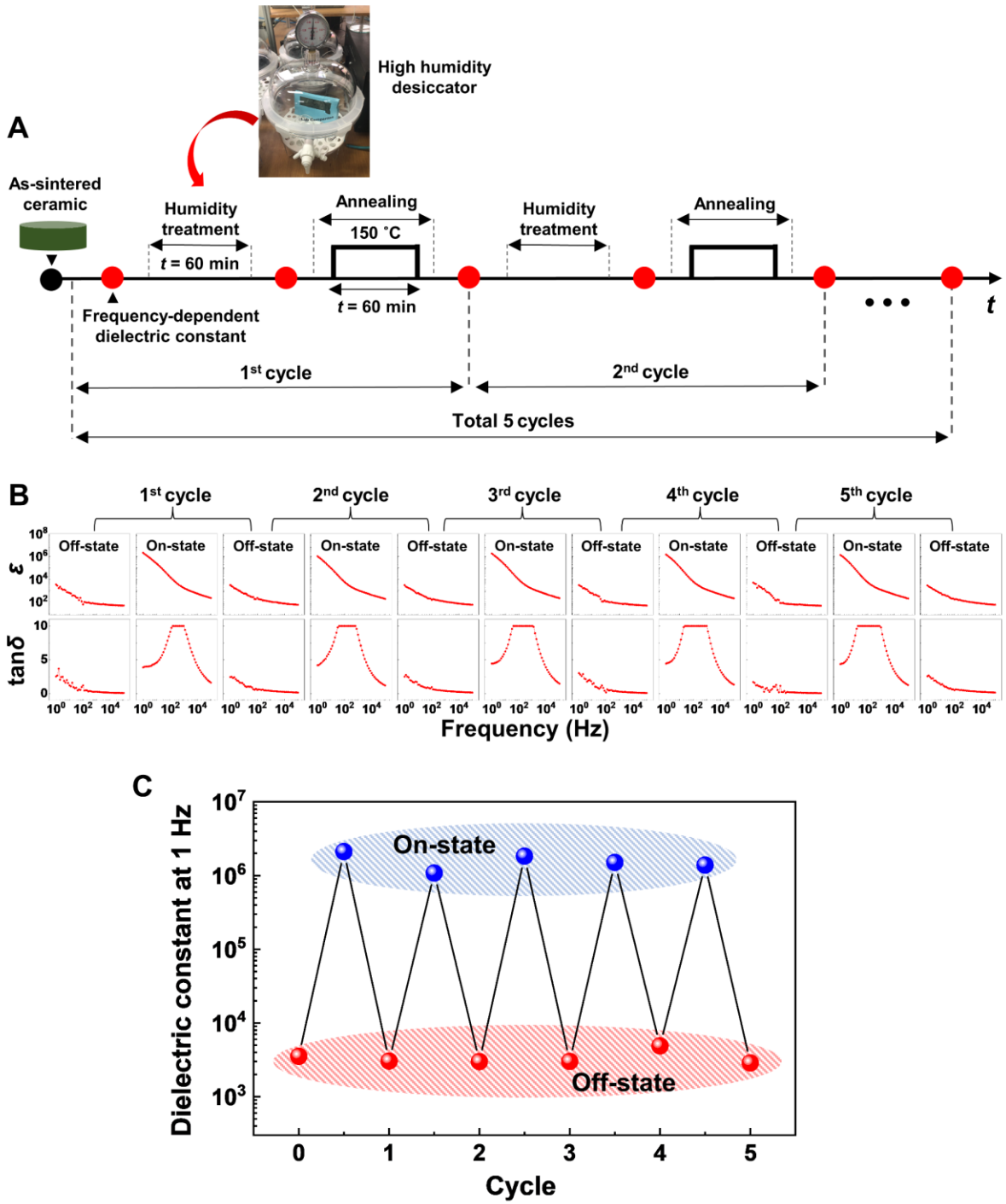

Figure 5.5 The control of dielectric permittivity in Ni-substituted $BaTiO_3$ experimentally. (a) The schematic of the experimental sequence. (b) The dielectric constant and corresponding dielectric loss of Ni-substituted $BaTiO_3$ ceramics during 5 cycles of high-humidity treatment and thermal annealing. (c) The change of dielectric constant at a frequency of 1Hz through the treatment under

a humid condition and thermal annealing over 5 cycles. The red and blue circles represent the dielectric permittivity of ceramics after thermal annealing (i.e., off-state) and after the treatment under a humid environment (i.e., on-state), respectively.

5.5. Realization of oxide ceramic-based humidity sensors

To demonstrate the implementation of humidity sensing characteristics in our Ni-substituted $BaTiO_3$ ceramics, the electrical resistance of our ceramics was measured at different relative humidity (RH). A device in a capacitor form (i.e., Ag electrode/ceramic/Ag electrode) was used to test the sensing performance. The humidity of the chamber varied from 0 to 80% in a stepwise manner (a step of 20%) with a time interval of about 1,000 seconds [Fig. 5.6(a)]. Unlike pure $BaTiO_3$ ceramics, Ni-substituted $BaTiO_3$ ceramics should contain a large number of oxygen vacancies, which can result in electrical leakage and dielectric loss [3, 4]. Due to the relation between electrical conductivity and dielectric properties in a lossy dielectric, changes in dielectric permittivity could be evaluated by examining the variation of electrical resistance with RH [1, 2]. Fig. 5.6(b) showed the dynamic change in the resistance as a function of relative humidity. It was observed that the electrical resistance of Ni-substituted $BaTiO_3$ ceramic decreased with a stepwise increase of relative humidity. Moreover, the electrical resistance promptly increased and returned to the initial value when the relative humidity was restored to the reference condition (RH = 0%). We also noted that the resistive response in pure $BaTiO_3$ was almost constant with the change of relative humidity. Our experimental results are of practical interest for the realization of Ni-substituted $BaTiO_3$ ceramics as a potential material for humidity-sensing applications with high sensitivity.

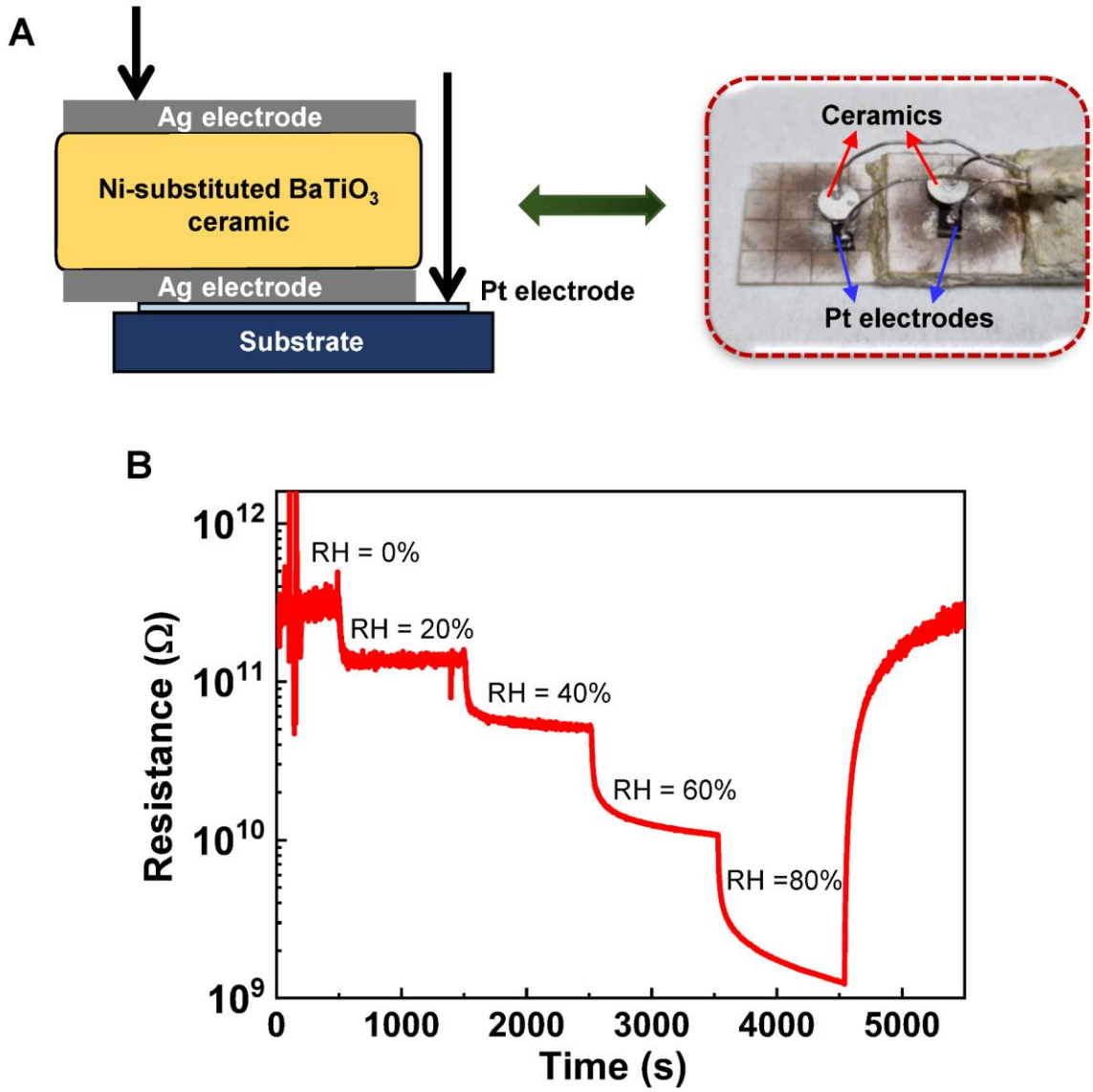

Figure 5.6 Sensing-performance experiments. (a) Schematic diagram of a humidity sensing experiment. (b) Resistive responses of Ni-substituted $BaTiO_3$ ceramics to the change in relative humidity. A stepwise decrease in the electrical resistance of the sensors was observed with the increasing humidity levels. The electrical resistance of ceramics gradually recovered to the initial value when the relative humidity changed from 80 to 0% again.

The manipulation of dielectric responses in dielectric materials is of great interest for technological applications [5, 6]. The tuning of dielectric properties by external stimuli enables the realization of sensing devices with multifunctionality [7-9]. Herein, we experimentally demonstrate the potential applications of oxygen-deficient 6H-hexagonal $BaTiO_3$ ceramics for the realization of dielectric-based humidity sensors with high sensitivity. The susceptibility of dielectric properties in Ni-substituted $BaTiO_3$ ceramics to various ambient environments is systematically examined. The ultrahigh dielectric permittivity of Ni-substituted $BaTiO_3$ ceramics is reversibly controllable by hydrogenation through a specific treatment under ambient environments and thermal annealing, which allows us to implement oxide-ceramic-based dielectric sensors (e.g., hygrometers). Furthermore, the degree of variation (i.e., the on-off ratio) in dielectric constant is very large ($\sim 10^3$), leading to the enhanced sensitivity of sensors. Finally, we have also tested the humidity-sensing performance of our Ni-substituted $BaTiO_3$ ceramics in an actual device.

References

1. D. M. Pozar, *Microwave engineering* (John Wiley & Sons, 2011).
2. K. C. Kao, *Dielectric phenomena in solids* (Elsevier, 2004).
3. D. C. Sinclair, J. M. S. Skakle, F. D. Morrison, R. I. Smith, T. P. Beales, *J. Mater. Chem.* **9**, 1327-1331 (1999).
4. G. M. Keith, M. J. Rampling, K. Sarma, N. M. Alford, D. C. Sinclair, *J. Eur. Ceram. Soc.* **24**, 1721-1724 (2004).
5. G. Catalan, J. Scott, *Nature* **448**, E4-E5 (2007).
6. T. Nagai, H. Takahashi, R. Okazaki, K. Tanabe, I. Terasaki, H. Taniguchi, *Appl. Phys. Lett*. **110**, 172901 (2017).
7. T. Ishihara, S. Matsubara, *J. Electroceramics* **2**, 215-228 (1998).
8. W. H. Ko, Q. Wang, *Sens. Actuator A Phys*. **75**, 242-251 (1999).
9. P. Bindra, A. Hazra, *J. Mater. Sci: Mater. Electron.* **29**, 6129-6148 (2018).

Chapter 6

Further application of dielectric oxides to multi-functional devices

6.1. Hydrogen storage with high capacity

Hydrogen has been identified as a clean energy source for the future due to its high energy efficiency, environmental friendliness, and non-toxicity [1, 2]. For instance, hydrogen can be used in stationary power generation, where it is used in fuel cells to generate electricity and heat. In transportation, fuel cell engines, which convert the chemical energy of a fuel (i.e., hydrogen) into electrical energy, have been popular in vehicles [2]. However, one of the main challenges is the storage of hydrogen in an efficient and safe manner [1, 3]. The storage of hydrogen in a traditional method like compressed gas or cryogenic liquid hydrogen has limited the actual applications.

Complex oxides have emerged as a promising material for hydrogen storage due to their unique electronic, structural, and catalytic properties. It has been reported the hydrogen storage capacity in various oxide materials such as ZrO, TiO_2, and SnO_2 [4, 5]. Metal oxides, such as titanium oxide, can reversibly react with hydrogen to form metal hydrides, which can store hydrogen at a high density. Additionally, these metal oxides have high thermal stability and are abundant in nature, making them economically viable for large-scale production [5].

In our work, hydrogen ions are introduced to the oxygen-deficient $BaTiO_3$ ceramics by hydrogenation process via an ambient environment treatment. We stress that the presence of the hydrogen ions in the 6H-hexagonal $BaTiO_3$ ceramics by hydrogenation was experimentally corroborated indicating the introduction and storage of hydrogen ions into dielectric oxide

ceramics (Figure 6.1). Conceptually, our finding opens up the potential application of oxygen-deficient $BaTiO_3$ ceramics in hydrogen storage with a high capacity [6].

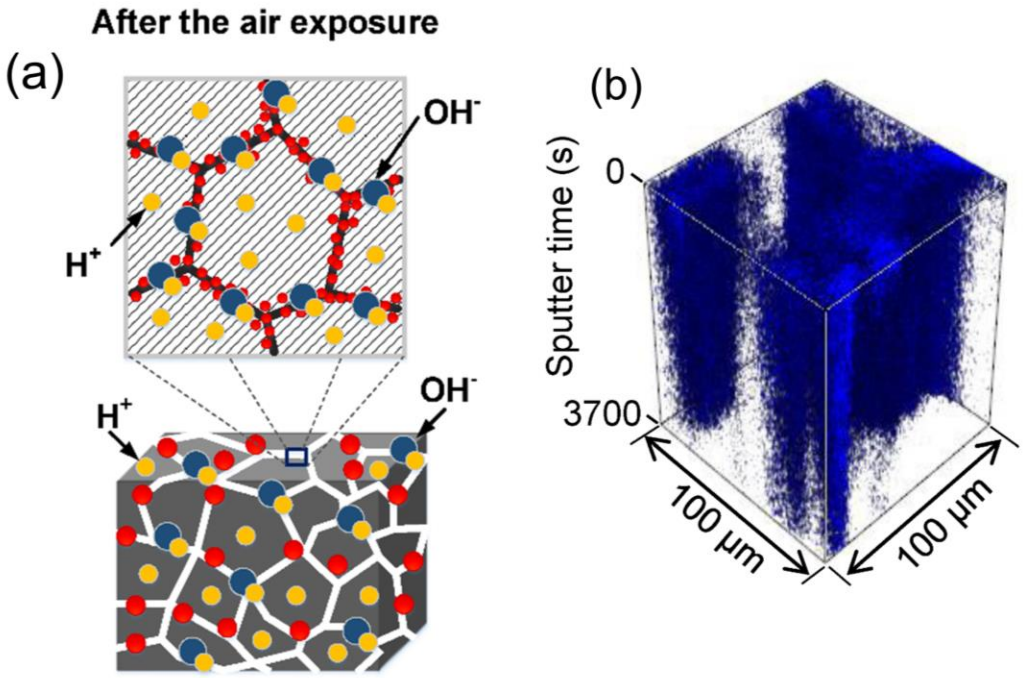

Figure 6.1 (a) A possible mechanism of the introduction and storage of hydrogen ions into oxygen-deficient oxide ceramics via hydrogenation. (b) Experimental evidence of the presence of hydrogen ions in Ni-substituted $BaTiO_3$ ceramics after a protonation process using TOF-SIMS analyses.

6.2. High-efficiency oxide catalysts for water splitting

Water splitting is a chemical process that involves the separation of water molecules (H_2O) into their constituent elements including hydrogen (H_2) and oxygen (O_2) [7]. Nowadays, metal oxides (e.g., TiO_2, WO_3, Fe_2O_3) have been extensively studied as catalysts for water splitting [7, 8]. According to our experimental results, the Ni-substituted $BaTiO_3$ would be a potential catalyst for the water splitting process. When the water molecules in the ambient environment contact with

the ceramics, the dissociation of water molecules into protons (H^+) and hydroxyls (OH^-) energetically appears on the surface of oxide ceramics in the presence of oxygen vacancy defects. Under the excitation of external energy (e.g., light, electrical, and thermal energies), the water spilling reaction would further happen, which produces hydrogen and oxygen gases (Figure 6.2). This highly implies that the Ni-substituted $BaTiO_3$ ceramics can be utilized as a new oxide catalyst for water splitting with high efficiency.

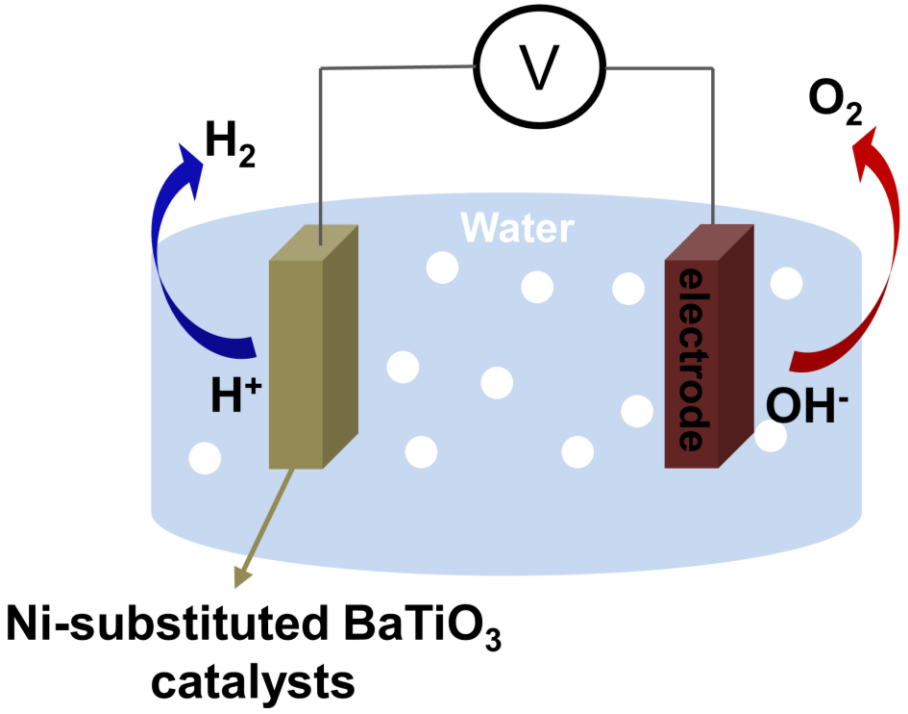

Figure 6.2 The potential application of Ni-substituted $BaTiO_3$ ceramics as an oxide catalyst for the water splitting.

References

1. J. Graetz, *Chen. Soc. Rev* **38**, 73-82 (2009).
2. T. V. Choudhary, D. Goodman, *Catal. Today* **77**, 65-78 (2002).
3. S.-Y. Lee, J.-H. Lee, Y.-H. Kim, J.-W. Kim, K.-J. Lee, S.-J. Park, *Processes* **10**, 304 (2022).
4. Q. Wan, C. Lin, X. Yu, T. Wang, *Appl. Phys. Lett.* **84**, 124-126 (2004).
5. B. Chen, Z. Liu, C. Li, Y. Zhu, L. Fu, Y. Wu, T. van Ree, in *Metal Oxides in Energy Technologies*. (Elsevier, 2018), pp. 251-274.
6. H. Yoon, M. Choi, T.-W. Lim, H. Kwon, K. Ihm, J. K. Kim, S.-Y. Choi, J. Son, *Nat. Mater.* **15**, 1113-1119 (2016).
7. R. M. Navarro Yerga, M. C. Álvarez Galván, F. Del Valle, J. A. Villoria de la Mano, J. L. Fierro, *Chem. Sus. Chem.* **2**, 471-485 (2009).
8. J. Wang, T. van Ree, Y. Wu, P. Zhang, L. Gao, in *Metal Oxides in Energy Technologies*. (Elsevier, 2018), pp. 205-249.

Chapter 7

Summary and perspective

7.1. Summary

For the last several decades, boosting dielectric permittivity, which represents the electrical polarizability of dielectric materials, has been considered a key step for exploring exotic physical phenomena in nature and for achieving novel fictional devices with excellent operational efficiency. In the aspect of device applications, such a huge dielectric permittivity, which is tunable via external stimuli, enables us to accomplish multifunctional devices such as switchable passives sensors. In this research, we experimentally realized the dielectric oxide ceramics with enhanced dielectric responses, which can be reversibly manipulated by external stress, for the actual realization of oxide-based gas sensors with high sensitivity.

First, we experimentally realize the 6H-hexagonal $BaTiO_3$ ceramics by cation substitution. The room-temperature polymorphic phase transition in $BaTiO_3$ ceramics induced by Ni-substitution is examined. A structural phase transition of the tetragonal-cubic-hexagonal polymorph is obtained in Ni-substituted $BaTiO_3$ ceramics as the doping concentration increases. When a Ti^{4+} cation is replaced by a Ni^{2+} ion, oxygen vacancy defects are generated to balance the overall charge neutrality. In the presence of oxygen vacancies, the Ti^{4+} oxidation state is reduced to 3+ at a defect site locally. The Ti-O hybridization in tetragonal $BaTiO_3$ becomes weakened by the local reduction of Ti charge valence state. As a consequence, a 6H-hexagonal phase in $BaTiO_3$, which is only stable above 1460 °C for the stoichiometric composition, is stabilized at room temperature by Ni substitution. The 6H-hexagonal $BaTiO_3$ would be an excellent platform for examining the dielectric responses to hydrogenation in dielectric oxides.

Second, the ultrahigh dielectric permittivity is achieved in 6H-hexagonal $BaTiO_3$ ceramics by hydrogenation through a specific treatment under ambient environments. Note that protonation by water dissociation is attainable in dielectric oxide ceramics with oxygen off-stoichiometry. The hydrogen ions dissociated from water molecules are introduced into Ni-substituted $BaTiO_3$ ceramics leading to the modification of dielectric responses. The introduction of hydrogen ions would produce the heterogeneous distributions of the crystal structures and the electric polarizability microscopically leading to the enhancement of overall dielectric permittivity in the Ni-substituted $BaTiO_3$ ceramics. Furthermore, the reversible control of dielectric permittivity in oxygen-deficient 6H-hexagonal $BaTiO_3$ ceramics by external stimuli can be utilized for device applications to dielectric-based gas sensors conceptually.

Finally, we provide a conceptual demonstration of sensing capability in our Ni-substituted $BaTiO_3$ ceramics for the realization of dielectric humidity sensors. The change of dielectric permittivity of Ni-substituted $BaTiO_3$ ceramics under various ambient environments is systematically investigated. The dielectric responses in 6H-hexagonal $BaTiO_3$ are reversibly controllable by hydrogenation through treatment under ambient conditions and subsequent thermal annealing. By monitoring the responses of the dielectric constant and the associated electrical conductivity to the water-vapor condition, we also evaluated the humidity sensing performance in Ni-substituted $BaTiO_3$ ceramics in an actual device.

7.2. Perspective

In this thesis, we provide a clear demonstration of the control dielectric properties in dielectric oxide ceramics by hydrogenation. In the aspect of device application, the protonation manipulation of the associated physical properties in dielectric oxides can enable the development

of multi-functional sensors with high efficiency and sensitivity. Furthermore, our approach of hydrogenation through water dissociation suggests potential applications for complex oxides in hydrogen storage, water splitting, and sensing devices.

Appendix: Detail user manual

A. Fabrication of Ni-substituted $BaTiO_3$ ceramics by solid-state reaction

Ni-substituted $BaTiO_3$ ($BaTi_{1-x}Ni_xO_{3-\delta}$) polycrystalline ceramics were prepared using the conventional solid-state reaction method. The raw materials of $BaCO_3$ (99.9%), TiO_2 (99.9%), and NiO (99.9%) were purchased from High Purity Chemicals (Figure A.1). Firstly, the $BaCO_3$, TiO_2, and NiO powders were weighed and mixed together.

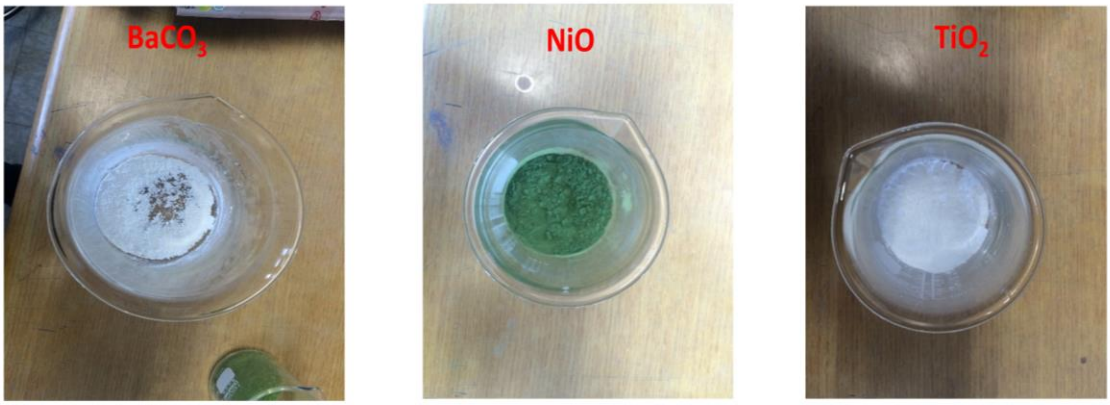

Figure A.1 The starting materials of $BaCO_3$ (99.9%), TiO_2 (99.9%), and NiO (99.9%) from High Purity Chemicals.

Then, the mixed powders were milled with yttria-stabilized zirconia balls and ethanol. The weight ratio of powder, zirconia balls, and ethanol is 1: 2: 3, respectively. The powders were ball-milled at 200 rpm for 24 hours.

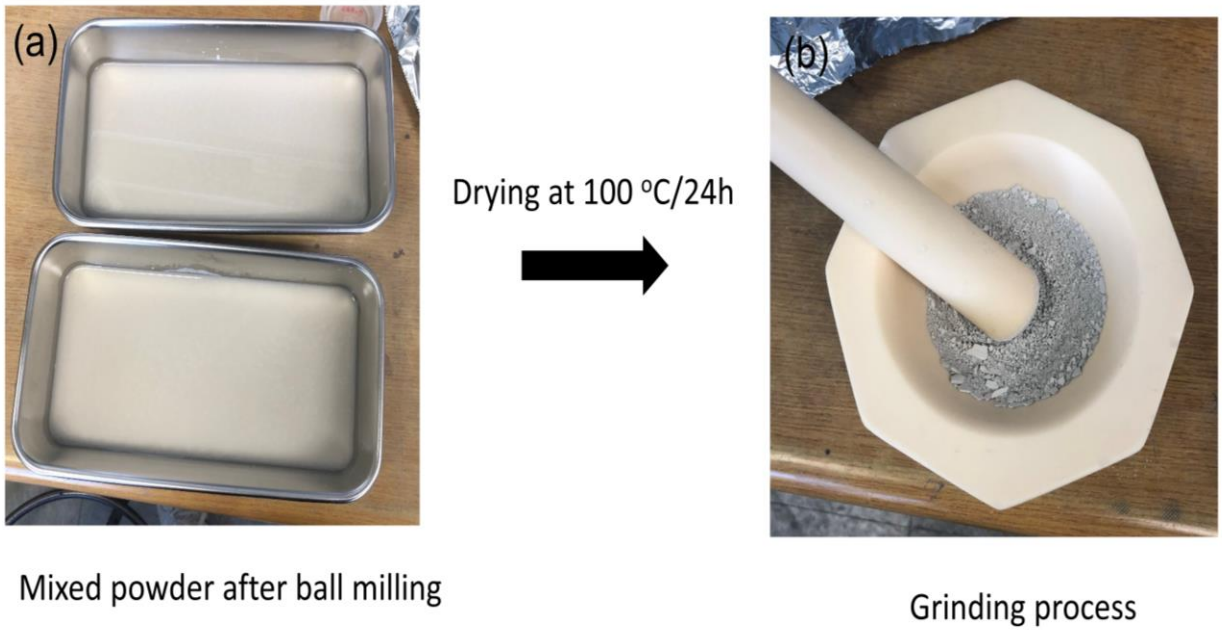

Figure A.2 (a) The mixed powders after ball-milling for 24 hours. (a) After drying at 100 °C for 24 hours, the powders were ground.

After the ball-milling process, the powders were dried at 100 °C for 24 hours to remove the ethanol [Figure A.2]. Next, the dried powders were ground for 15 min. We calcined the ball-milled powders in an alumina crucible in a box furnace at 1100 °C for 8 hours (the heating/cooling rate of 5 °C/min) in air, as shown in Figure A.3.

The as-calcined powders were re-grounded and then ball-milled again for 24 hours. After that, the ball-milled powders were dried and ground again to make fine powders with smaller grain sizes suitable for pelletizing.

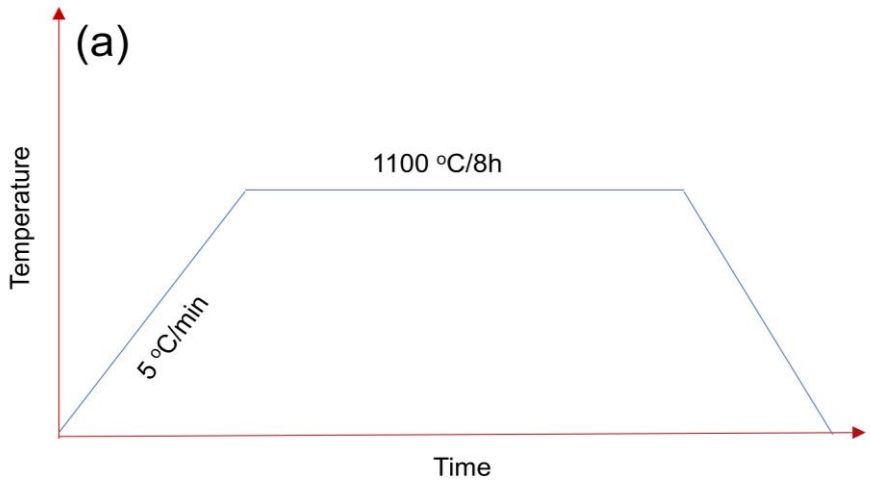

(b) Powder after calcinating at 1100 °C/8h

Figure A.3 (a) The calcination condition of Ni-substituted $BaTiO_3$ powders. We calcinated the powder at 1100 °C for 8 hours with a heating/cooling rate of 5 °C/min. (b) The Ni-substituted $BaTiO_3$ powders before and after the calcination process.

Next, we added polyvinyl-alcohol ($[CH_2CH(OH)]_n$) binder solution to the powders. Then, we molded a 1-inch-diameter pellet and pelletized it under a pressure of ~133 Pa. The Ni-substituted $BaTiO_3$ ceramic pellet was then sintered at 1330 °C for 6 hours in air to achieve crystallization [see Figure A.4].

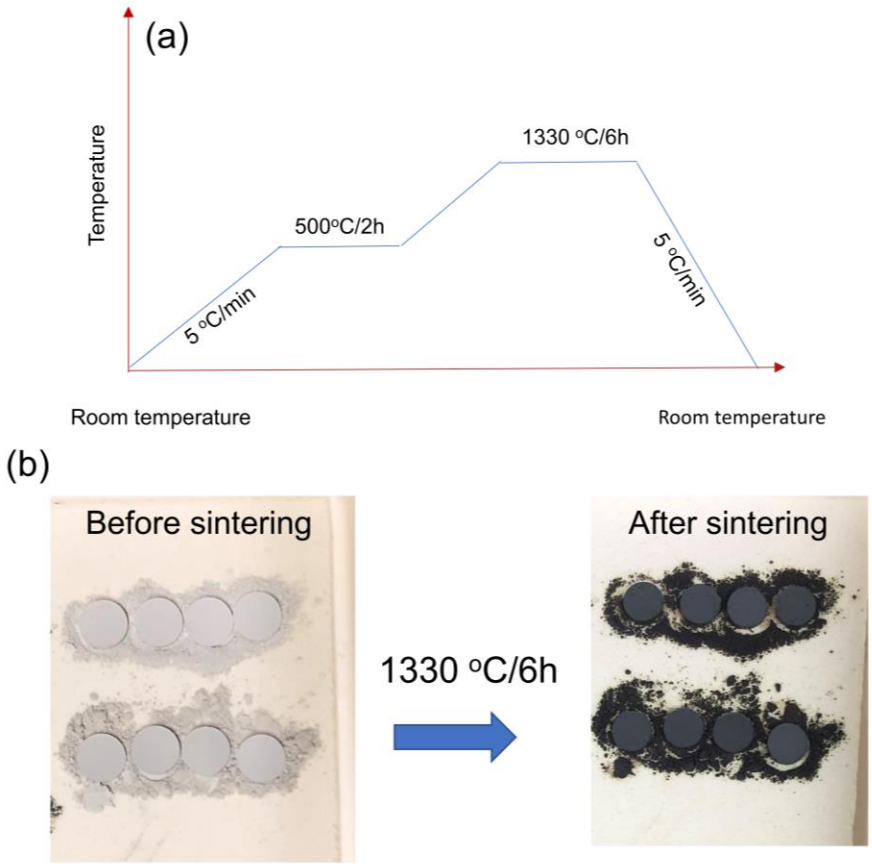

Figure A.4 (a) The sintering condition of Ni-substituted $BaTiO_3$ ceramic pellets. The ceramics were calcinated at 1330 °C for 6 hours. Before that, we annealed the ceramics pellets at 500 °C for 2 hours to remove the polyvinyl-alcohol binder. The heating and cooling rate is 5 °C/min. (b) The Ni-substituted $BaTiO_3$ ceramics before and after sintering.

B. X-ray diffraction measurements

The crystalline structure of Ni-substituted $BaTiO_3$ ceramic samples was identified by an x-ray diffractometer [wavelength $\lambda = 1.5406$ Å (Cu Kα), D8 Advance, Bruker, Germany] at room temperature.

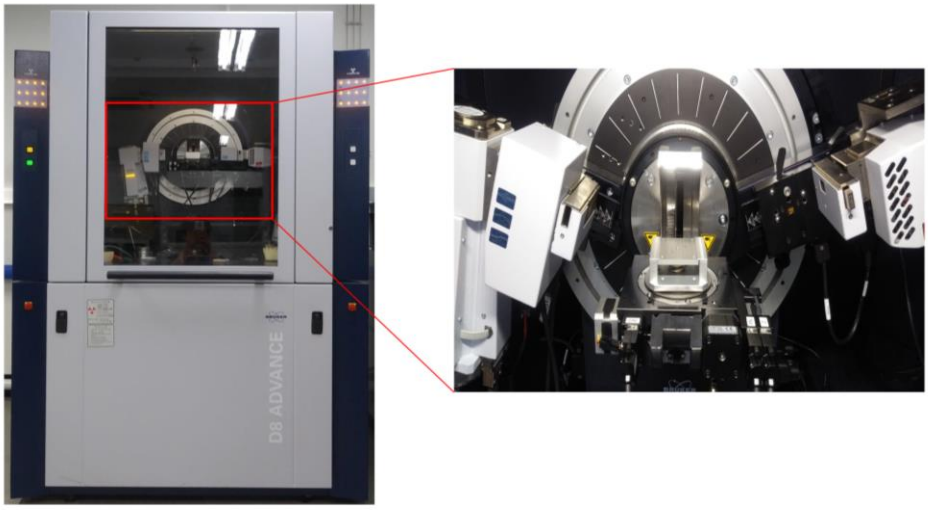

Figure B.1 Bruker D8 Advance equipment.

B.1 Setting of the Trio, Detector, and filter slot

Before the XRD measurement of polycrystalline ceramics, we set up the detector and filter for a suitable measurement mode. Here we used the motorized slit beam path in the Trio optic for the measurement of polycrystalline ceramics. In the Trio site, we inserted a soller slit and a Ni filter, as shown in Figure B.2. A soller slit and a Cu filter were installed in front of the detector (Figure B.3)

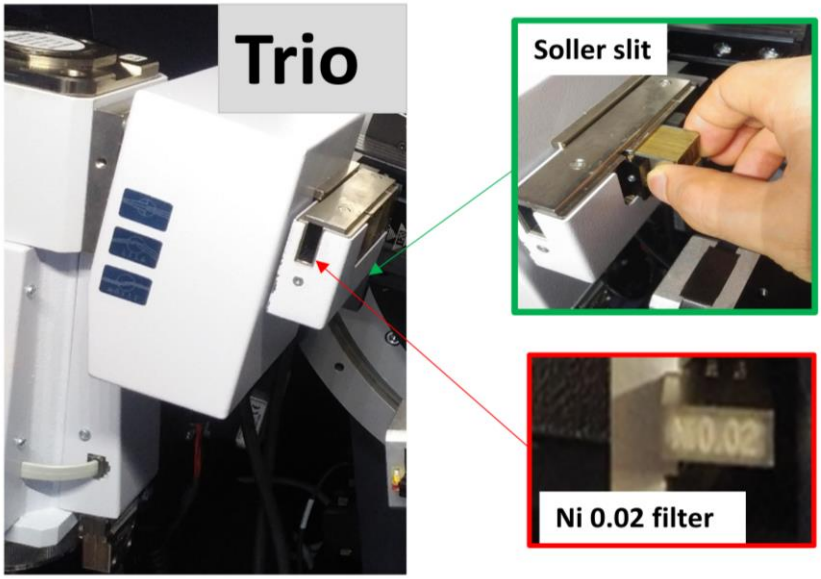

Figure B.2 The setting of the soller slit and Ni filter for the XRD measurements of polycrystalline ceramics.

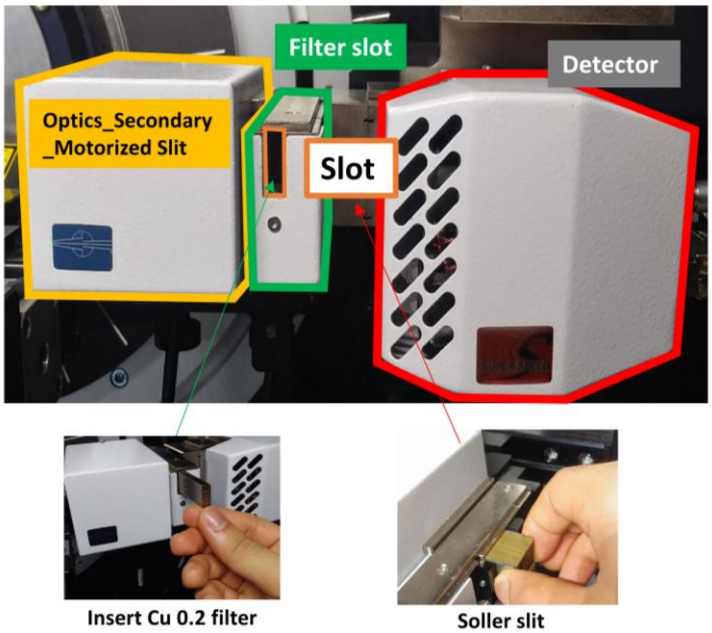

Figure B.3 A soller slit and Cu filter were installed in front of the detector.

B.2 Initialization

1. We open the file DIFFAC.MEASUREMENT CENTER on the desktop.

2. Go to File, select Application, and choose the Powder Diffraction mode (Figure B.4).

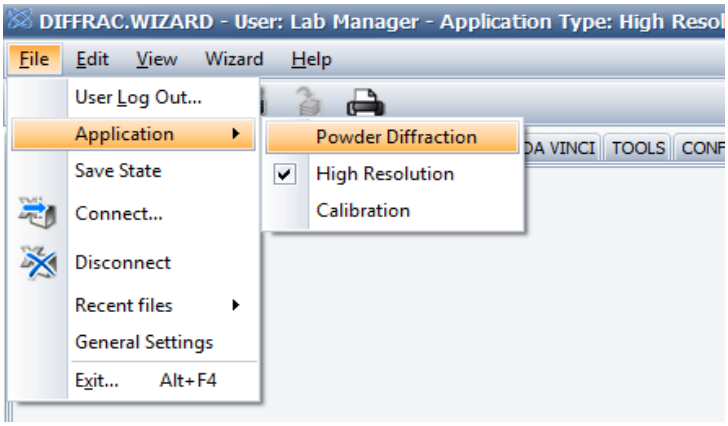

Figure B.4 Setting the measurement mode.

3. Set the initial positions: omega = 0, detector = 0, Chi cradle = 0, Beam H = 0, and Z Cradle = 0

Click to ‘position all checked drive” [(Figure B.5(a)].

4. Select the Trio option: Motorized Slit: Slitwidth [Figure B.5(b)].

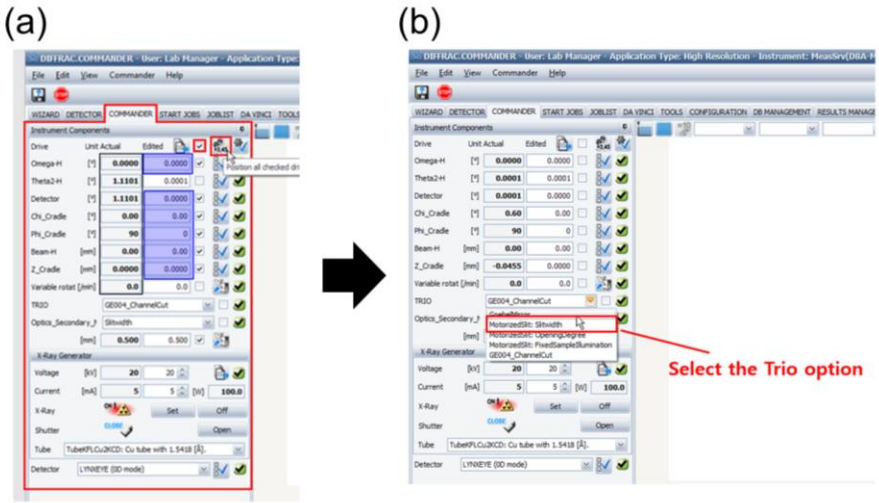

Figure B.5 Initialization process.

B.3 Full beam alignment

1. Set X-ray Generator to operating: Voltage = 40 kV, Current = 40 mA.

2. Select the Detector: LYNXEYE (0D mode) – Linear opening = 0.5 (Figure B.6).

3. Do the 2Theta scan: (Figure B.7)

Scan mode: Continuous, Time (sec): 0.2, Parameter(Start): -1^{o}, Parameter(Stop): 1^{o},

Parameter(Increment): 0.02^{o}.

4. Select Commander – Reference and Offset Determination.

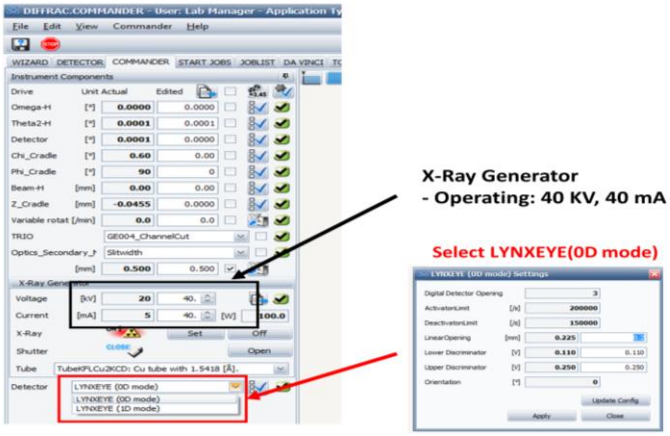

Figure B.6 X-ray generator and detector settings.

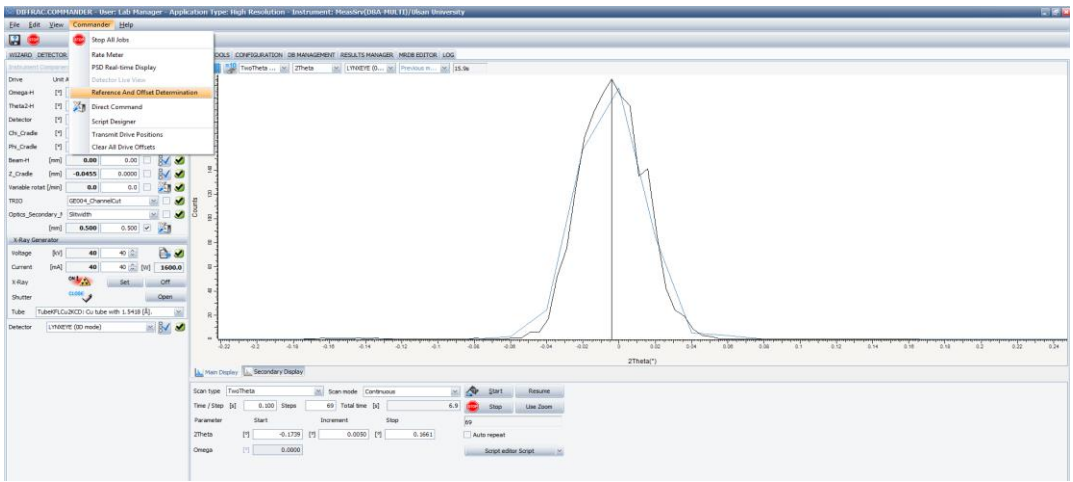

Figure B.7 Full beam alignment.

B.4 Starting the measurements

1. Mount ceramics on the sample holder (Figure B.8).

2. Select the Detector: LYNXEYE (1D mode).

3. Do the 2Theta-Omega scan: (Figure B.9).

Scan mode: Continuous, Time(sec): 1, Parameter(Start): 20^{o}, Parameter (Stop): 80^{o},

Parameter (Increment): 0.01^{o} , PSD opening: 2.94.

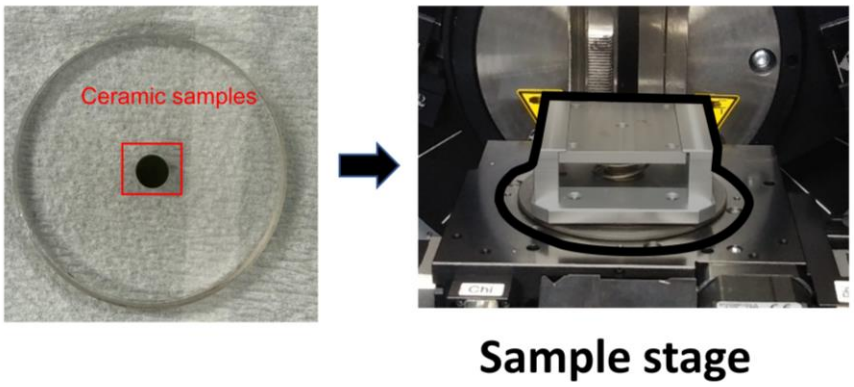

Figure B.8 Mounting the ceramics sample on the holder.

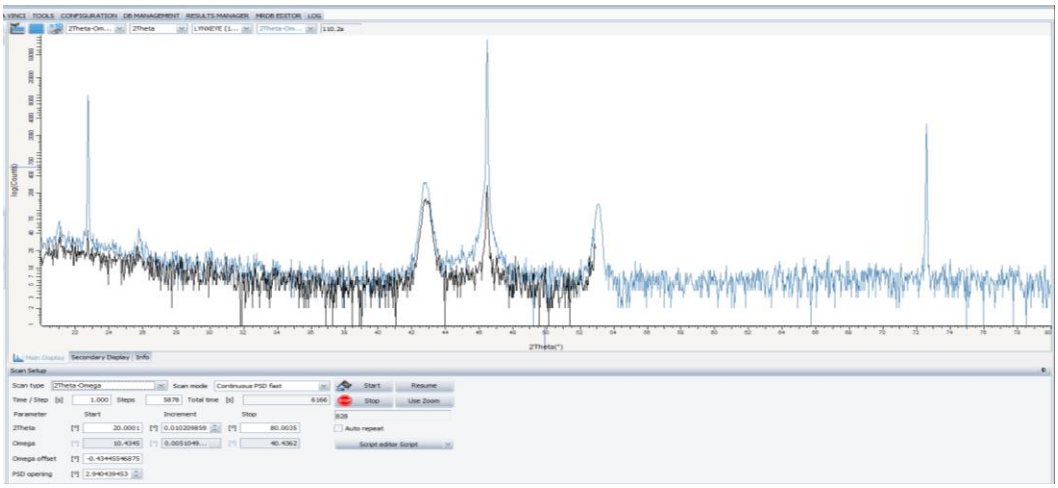

Figure B.9 The 2Theta-Omega scan after alignment.

C. Manual for impedance measurements

The electrical properties (i.e., impedance and dielectric properties) of Ni-substituted $BaTiO_3$ ($BaTi_{1-x}Ni_xO_{3-\delta}$) polycrystalline ceramics were measured using an impedance analyzer (HIOKI 3522-50) in a frequency range of $1\text{-}10^5$ Hz. Figure C.1 showed the experimental setup of the impedance measurements.

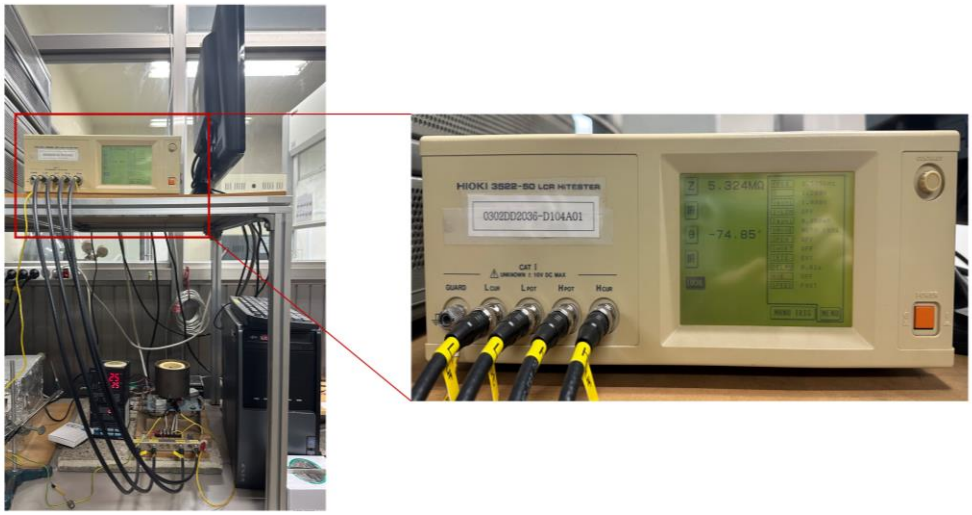

Figure C.1 Experimental set-up of the impedance measurement. The impedance analyses were carried out by a HIOKI 3522-50 analyzer.

C.1 Sample preparation

To measure the electrical properties (i.e., impedance and dielectric properties) of Ni-substituted $BaTiO_3$ ceramics, we made the electrodes on the surface of ceramics [Figure C.2(a)]. The as-sintered ceramic samples were coated with silver pastes on both the top and bottom sides.

After that, the ceramics with silver electrodes were annealed in box furnace cured them at 700 °C for 30 minutes for curing [see Figure C.2(b)].

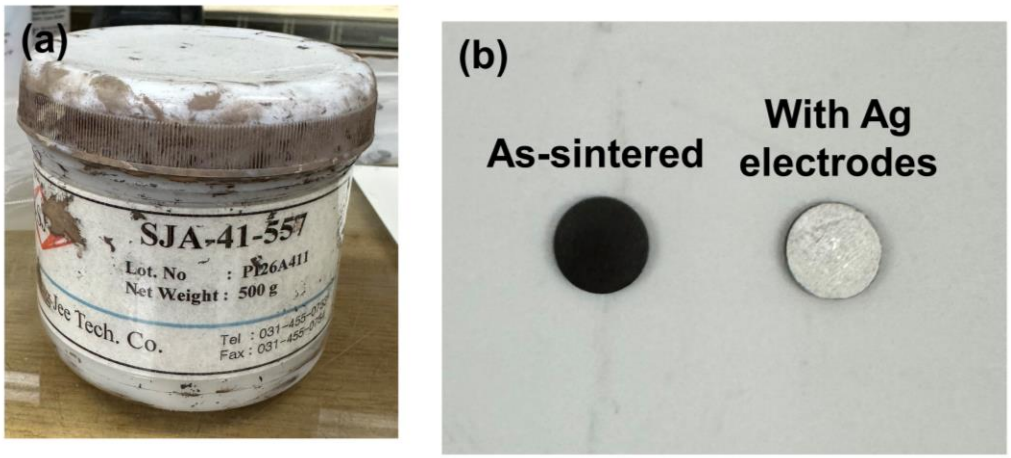

Figure C.2 The silver paste (SJ-41-557, Sung Lee Tech. Co.) was used to make the electrodes of ceramics samples. (b) the Ni-substituted $BaTiO_3$ ceramics without electrodes and with Ag electrodes

C.2 Setting of impedance measurement

1. We connected the ceramic samples with the impedance analyzer. The Ag wires were used to contact the ceramics (Figure C.3).

2. Open the HIOKI 3522-50 analyzer.

3. Open the program with a path: Computer/New Volume (F:)/HIOKI_2012/Hioki-Sk935_IS_D (see Figure C.4).

4. In the Hioki-Sk935_IS_D program (see Figure C.5):

- Set the frequency: startF = 1 (stat frequency), stopF = 100000 (end frequency).

- Material Name: put the name of samples.

- Path_File Name: select the folder to save the data.

5. Start the measurement: Click the run signal.

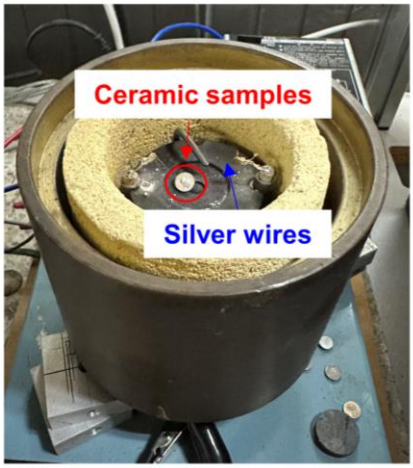

Figure C.3 The Ni-substituted $BaTiO_3$ ceramics with electrodes were contacted to the analyzer by silver wires.

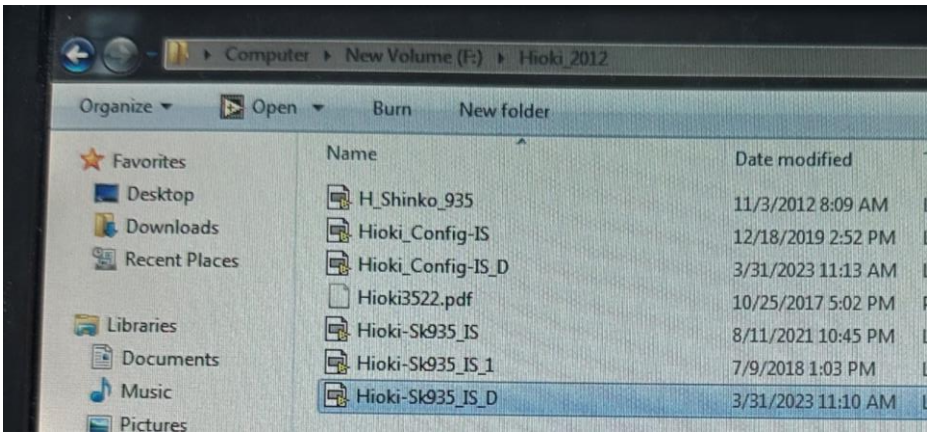

Figure C.4 Open the program with the path of: Computer/New Volume (F:)/HIOKI_2012/Hioki-Sk935_IS_D.

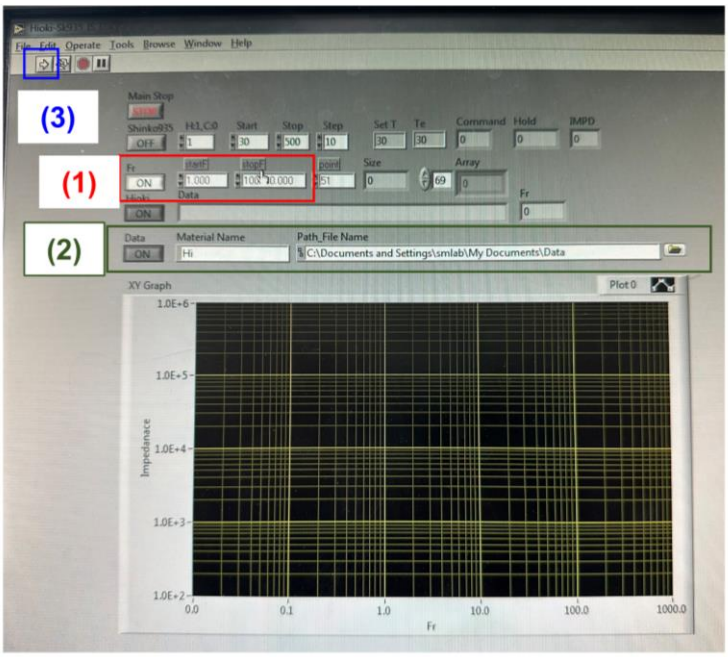

Figure C.5 The measurement setting. (1) Set the frequency range from 1 (startF) to 100000 Hz (stopF). (2) We put the sample name in Material Name and the folder to save data in Path_File Name Open. (3) Click the Run button to start the measurement.

C.3 Data analyses

In the raw data, each data column corresponds to an individual parameter:

A: temperature, B: frequency, C: impedance (Z), D: phase (θ), E: capacitance, F: dielectric loss.

1. The real and imaginary parts of impedance are calculated as follows:

Real part of impedance (Z') = Z* cos(θ)

Imaginary part of impedance (Z'') = Z* sin(θ)

2. Dielectric constant of ceramics is calculated from the equation:

$$C = \varepsilon\varepsilon_o \frac{A}{d}$$

where C is measured capacitance. ε is the dielectric constant (relative permittivity). ε_o is the permittivity of the vacuum. A is the surface area of ceramic samples. D is the thickness of the samples.

	A(X)	B(Y)	C(Y)	D(Y)	E(Y)	F(Y)
Long Name	temp	freq	Z	phase	capacitance	loss
Units						
Comments						
Sparklines						
1	20	100000	30130	-43.67	3.648E-11	1.04739
2	20	79432.82347	33340	-41.31	3.968E-11	1.13775
3	20	63095.73445	36620	-39.27	4.36E-11	1.22323
4	20	50118.72336	39930	-37.5	4.841E-11	1.30302
5	20	39810.71706	43290	-36	5.429E-11	1.37642
6	20	31622.7766	46720	-34.86	6.158E-11	1.43561
7	20	25118.86431	49800	-33.65	7.051E-11	1.50203
8	20	19952.62315	54140	-33.73	8.183E-11	1.49763
9	20	15848.93193	58170	-33.65	9.565E-11	1.50232
10	20	12589.25412	62420	-34	1.133E-10	1.48231
11	20	10000	67470	-34.74	1.344E-10	1.44225
12	20	7943.28235	73000	-35.67	1.6E-10	1.39327
13	20	6309.57345	79160	-36.96	1.916E-10	1.32902
14	20	5011.87234	86490	-38.37	2.279E-10	1.26292
15	20	3981.07171	94860	-40.01	2.71E-10	1.19131
16	20	3162.27766	104900	-41.81	3.199E-10	1.11813

Figure C.6 The raw data of impedance measurement. The columns of A, B, C, D, E, and F correspond to the temperature, frequency, impedance, phase, capacitance, and dielectric loss of ceramic samples.

D. Temperature-dependent dielectric constant analyses

The dielectric permittivity as a function of temperature in Ni-substituted $BaTiO_3$ ceramics were measured using an impedance analyzer (HP4192A). Figure D.1 showed the experimental setup of the temperature-dependent dielectric permittivity measurements. The dielectric constant and loss of the samples were performed across a temperature range of 30 to 350 °C at three different frequencies of 1 kHz, 10 kHz, and 100 kHz.

Figure D.1 Experimental set-up of the temperature-dependent dielectric constant. A HP4192A analyzer was used to measure dielectric permittivity as a function of temperature.

D.1 Setting of impedance measurement

1. We connected the ceramic samples with the impedance analyzer. The Ag wires were used to contact the ceramics (Figure D.2).

2. Put the ceramic sample inside the tube furnace (Figure D.2).

3. Open the HP4192A analyzer.

4. Open the program with a path:

Computer/New Volume (F:)/HP4192A/ HP4192A/4192A_71_2017 (see Figure D.3).

5. In the 4192A_71_2017 program (see Figure C.5):

- Set the temperature range: start = (stat temperature), stop = (end temperature) [(1) in Figure D.4].

- Set the frequency: startF = (stat frequency), stopF = (end frequency) [(2) in Figure D.4].

- Material Name: put the name of samples [(3) in Figure D.4].

- Path_File Name: select the folder to save the data [(4) in Figure D.4].

6. Start the measurement: Click the run signal [(5) in Figure D.4].

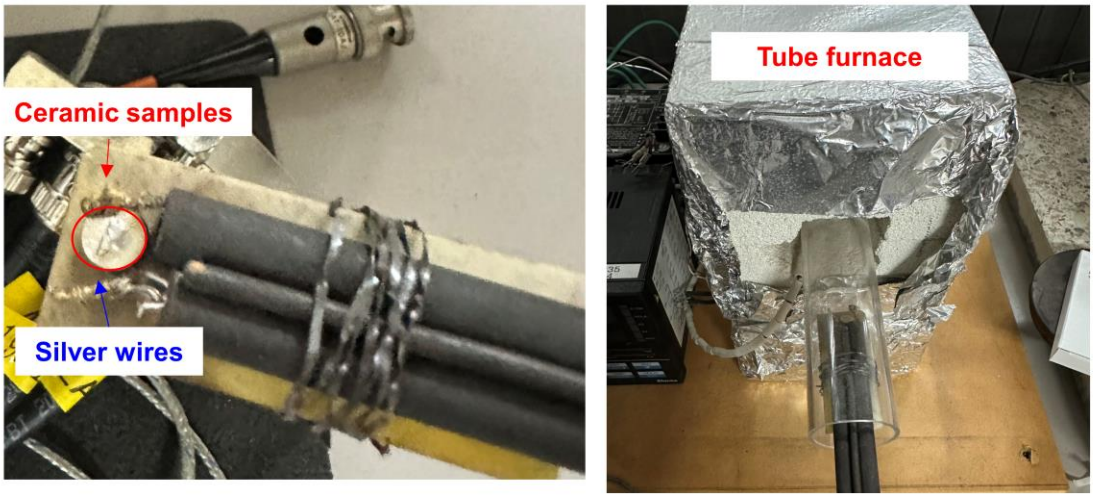

Figure D.2 The Ni-substituted $BaTiO_3$ ceramics with electrodes were contacted to the analyzer by silver wires. The samples were put into the tube furnace.

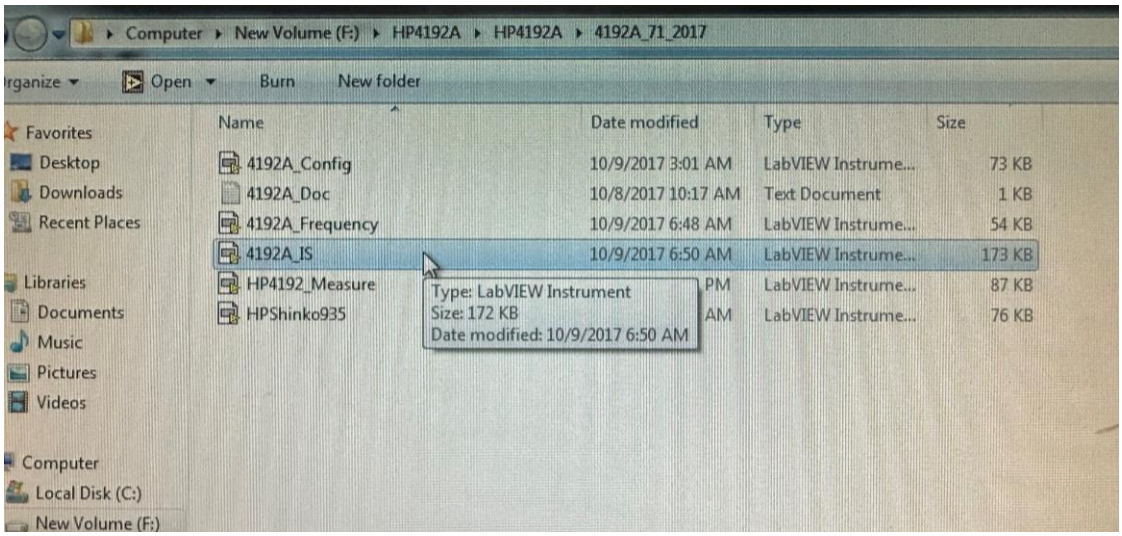

Figure D.3 Open the program with the path of: Computer/New Volume (F:)/HP4192A/ HP4192A/4192A_71_2017.

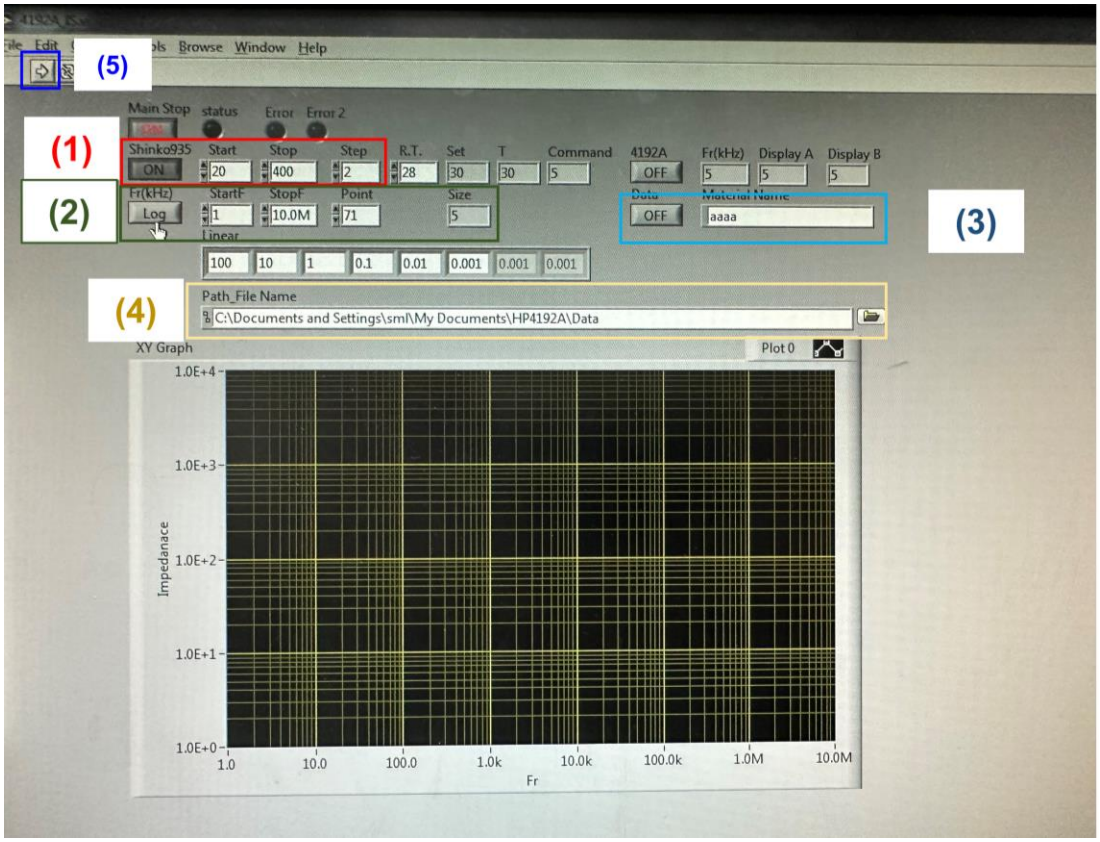

Figure D.4 The measurement setting. (1) Set the temperature range. (2) Set the frequency range. We put the sample name in (3) Material Name and the folder to save data in (4) Path_File Name Open. (5) Click the Run button to start the measurement.

Publication List

[1] “Ultrahigh dielectric permittivity in oxide ceramics by hydrogenation”

N. X. Duong, J.-S. Jang, M.-H. Jung, J.-S. Bae, C. W. Ahn, J. S. Jin, K. Ihm, G. Kim, S. Y. Lim, J. Lee, D. D. Dung, S. Lee, Y.-M. Kim, S. Lee, S. M. Yang, C. Sohn, I. W. Kim, H. Y. Jeong, S.-H. Baek, and T. H. Kim

Sci. Adv. **9**, eadd8328 (2023).

[2] “Polymorphic phase transition in $BaTiO_3$ by Ni doping”

N. X. Duong, J.-S. Bae, J. Jeon, S. Y. Lim, S. H. Oh, A. Ullah, M. Sheeraz, J. S. Choi, J.-H. Ko, S. M. Yang, K.-H. Kim, I. W. Kim, C. W. Ahn, and T. H. Kim

Ceram. Int. **45**, 16305 (2019).

[3] “Reversibly controlled ternary polar states and ferroelectric bias promoted by boosting square-tensile-strain”

J. H. Lee, **N. X. Duong**, M.-H. Jung, H.-J. Lee, A. Kim, Y. Yeo, J. Kim, G.-H. Kim, B.-G. Cho, J. Kim, F. U. H. Naqvi, J.-S. Bae, J. Kim, C. W. Ahn, Y.-M. Kim, T. K. Song, J.-H. Ko, T.-Y. Koo, C. Sohn, K. Park, C.-H. Yang, S. M. Yang, J. H. Lee, H. Y. Jeong, T. H. Kim, and Y. S. Oh

Adv. Mater. **34**, 2205825 (2022).

[4] “Large-scale assembly of peptide-based hierarchical nanostructures and their antiferroelectric properties”

Y. Lee, K. W. Kim, **N. X. Duong**, H. Park, J. Park, C. W. Ahn, I. W. Park, S. C. Jang, D. H. Kim, M. Lee, W.-J. Chung, T. H. Kim, H. Lee, and K. Heo

Small **16**, 2003986 (2020).

Acknowledgments

First of all, I am deeply grateful to Professor Tae Heon Kim for extending to me an opportunity to pursue my Ph.D. within his esteemed research group. I would like to express my heartfelt thanks to Prof. T. H. Kim for his invaluable guidance and mentorship, both academically and ethically. He always supports me to overcome not only academic issues but also problems in normal life. His profound expertise in condensed matter physics has been a constant source of inspiration for me, and his unwavering support and continuous guidance have been instrumental in my successful completion of my Ph.D. degree.

I would like to express my appreciation to Research Professors Kim Ill Won and Chang Won Ahn for their unwavering support and invaluable suggestions throughout the past six years. Prof. C. W. Ahn's exceptional expertise has been instrumental in guiding my experimental design and conducting systematic characterization, enabling me to carry out my research effectively. I am grateful for their continuous help and contributions to my academic journey.

I would like to express my heartfelt gratitude to all my colleagues at the Quantum Materials Laboratory in the Department of Physics for their valuable contributions, engaging discussions, and for creating a friendly research environment. My special thanks go to Dr. Bong Chan Park, Dr. Muhammad Sheeraz, Mr. Jin San Choi, Mr. Jae Hun Jo, Mr. Yong Jin Jo, Ms. Nguyen Bich Thuy, Mr. Hwan Min Kim, Mr. Gwang Bo Sim, and Ms. Ji Won Kim. I am also deeply appreciative of the support and assistance provided by all the Professors and staff members at the Department of Physics, both in my academic pursuits and official matters. Thank you for your support throughout my research journey.

I am immensely grateful to the University of Ulsan for awarding me the Brains Korea (BK-21) scholarship, which has provided crucial financial support for my research. I would also like to

acknowledge the National Research Foundation of Korea (NRF) for the generous grants that have funded my entire research study. The support from the government of the Republic of Korea through NRF has been instrumental in facilitating my academic pursuits.

I would like to sincerely express my appreciation to all my Vietnamese friends at the University of Ulsan, especially Dr. Do Tri Cuong, Dr. Le Chinh Tam, Dr. Nguyen Anh Duc, Dr. Dao Hoang Vu, Mr. Nguyen Manh Hung, Ms. Nguyen Thi Quynh Anh, Dr. Ho Huynh Thi, Ms. Pham Thi Hue, Mr. Nguyen Huu Lam, Mr. Nguyen Anh Phuong ... They have assisted and supported me since the first day I came to Ulsan.

Finally, but most importantly, I extend my heartfelt gratitude to my loving family in Vietnam for their love, support, guidance, and encouragement throughout my educational journey. My parents have been my biggest motivation during my six years in South Korea, always by my side, and supporting me unconditionally. I would like to thank my sister (Nga) and brother-in-law (Hieu) for taking care of my parents instead of me while I was in Korea. I would like to give a deep love to my wife “Nhung” and “San” for patiently waiting. I am immensely grateful for the love and care of my entire family, as I could not have achieved this without them.

Nguyen Xuan Duong